

学位論文

A Study of Cryogenic Techniques
for Gravitational Wave Detection

(重力波検出のための極低温技術の研究)

平成 26 年 12 月博士（理学）申請
東京大学大学院理学系研究科
物理学専攻

榊原 裕介

Abstract

Gravitational waves, ripples of space-time predicted by Einstein's general theory of relativity, have not been detected directly yet. The direct detection of gravitational waves is of great importance in physics to test general relativity and in astronomy to open a gravitational wave astronomy. Currently, one of the most promising methods to detect gravitational waves directly is to utilize an interferometer to measure extremely small displacement ($\sim 10^{-21}$ m) of its mirrors. The first generation of interferometric gravitational wave detectors, such as LIGO in USA, VIRGO in Italy, GEO in Germany, and TAMA in Japan, have already been in operation. Several second-generation detectors with roughly one order of magnitude better sensitivity are currently under construction, such as AdLIGO, AdVIRGO, and KAGRA (the Large-scale Cryogenic Gravitational wave Telescope (LCGT), a km-scale cryogenic detector project in Japan). KAGRA aims to detect gravitational waves from coalescence of binary neutron stars more than once per year. Third-generation gravitational wave detectors, such as ET (the Einstein Telescope) in Europe, are also being planned. KAGRA and ET will enjoy two key advantages over other detectors: they will be constructed in an underground site with small seismic motion, and they will be equipped with cooled mirrors (at around 20 K in the case of KAGRA) to reduce thermal noise of the mirrors and the suspensions.

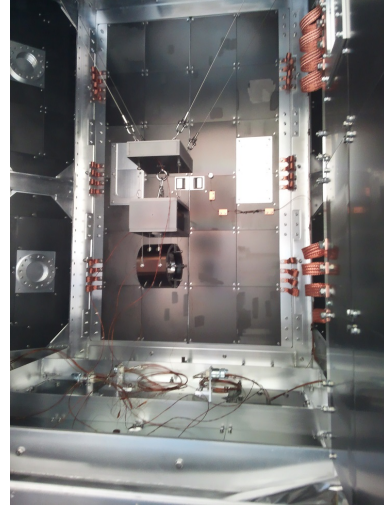
One of the most important problems in the cryogenic detectors, such as KAGRA and ET, is long cooling time of the mirrors (several months in KAGRA). During that time, the detectors cannot observe gravitational waves, and then gravitational wave events, such as the coalescence of binary neutron stars, will be missed. Because the detectors expect to have periodical maintenances including heating up and cooling down of the mirrors, long cooling time decreases observation time of the detectors. Therefore, it is necessary to reduce the cooling time.

In this thesis, I have worked on reduction of the cooling time, using a high-emissivity coating to increase cooling by thermal radiation and, simultaneously, to block out extra thermal radiation with radiation shield (duct shield). During this research, I have constructed a calculation model for the cooling system of KAGRA. I have tested an actual cooling system of the first cryogenic interferometric detector in the world, KAGRA, verified the calculation model, and demonstrated that the dead time can be reduced. I have achieved an increase of the observation duty factor from 71% to 77% based on the reduction in the cooling time. Although this thesis is mainly targeted to KAGRA, this study can be applied to other cryogenic interferometric

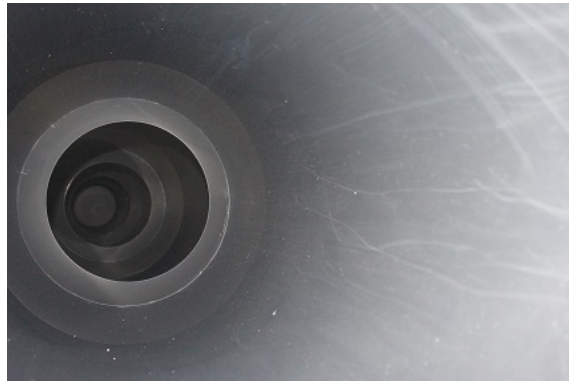
gravitational wave detectors, such as ET, in the future.



KAGRA cryostat



Half-sized payload



Inner surface of duct shield

Contents

1	Introduction	9
2	Graviational waves	13
2.1	Derivation of GWs	13
2.2	Quadrupole radiation	15
2.2.1	Oscillating masses	16
2.2.2	Masses in a circular orbit (model of a binary pulsar)	16
2.2.3	A Rotating rigid body (model of a neutron star)	17
2.3	An indirect proof of the existence of GWs	19
2.4	Principle of detecting GWs	19
2.4.1	Phase shift in a Michelson interferometer due to GWs	19
2.4.2	Response function and arm length	21
2.5	Fabry-Perot interferometer as a gravitational wave detector	21
2.5.1	Fabry-Perot interferometer	21
2.5.2	Response of the Fabry-Perot interferometer to GWs	25
2.6	Noise in an interferometer	27
2.6.1	Shot noise of photon	27
2.6.2	Radiation pressure noise	28
2.6.3	Quantum limit	29
2.6.4	Seismic noise	31
2.6.5	Thermal noise	31
2.7	Advantages of cryogenic mirrors	34
2.8	Interferometric gravitational wave detectors in the world	36
3	Cooling technique	37
3.1	Cooling mirrors of the interferometric gravitational wave detectors	37
3.1.1	Heat switch	37
3.1.2	Gas cooling	38
3.1.3	Optical cooling	38

3.1.4	Increasing radiation	38
3.2	CLIO, a prototype of KAGRA	39
3.3	KAGRA	39
3.4	A problem of the KAGRA cooling system	40
3.4.1	Formularization of water adsorption	40
3.4.2	Dead time due to heating up and cooling down	44
4	Cooling time reduction	45
4.1	Theory of thermal radiation	45
4.1.1	Thermal radiation	45
4.1.2	Black body radiation	46
4.1.3	Emissivity	47
4.1.4	Kirchhoff's law	48
4.1.5	Diffusive and specular surfaces	49
4.2	High-emissivity coating	51
4.2.1	Diamond Like Carbon (DLC) coating	51
4.2.2	Solblack	51
4.3	Calculation of cooling time of KAGRA	52
4.3.1	Method	53
4.3.2	Results	57
4.4	Small-scale experiment	58
4.4.1	Purpose	58
4.4.2	Method	58
4.4.3	Results	61
4.5	Experiments in the actual KAGRA cryostat	64
4.5.1	Purpose	64
4.5.2	Method	64
4.5.3	Results	66
4.6	Discussion	67
5	Duct shield	73
5.1	Design of the duct shields	73
5.2	Thermal radiation	75
5.2.1	Calculation	76
5.2.2	Measurement	78
5.3	Scattered light noise	82
5.3.1	Formularization of the scattered light noise	82
5.3.2	Calculation of amplitude scattering coefficient	83
5.3.3	Measurement of duct shield vibration	88

<i>CONTENTS</i>	7
5.4 Discussion	93
6 Discussion and conclusion	95
6.1 Discussion	95
6.2 Conclusion	97
A Thermal conductivity measurement of heat links	99
A.1 Purpose	99
A.2 Samples	99
A.3 Method	100
A.4 Result	101
B Sample code	105

Chapter

1

Introduction

Gravitational waves

Einstein's general theory of relativity has predicted gravitational waves, ripples of space-time curvature travelling with light speed. Evidence of the gravitational waves has been obtained in observations of binary pulsars or, possibly, recent cosmic-microwave-background (CMB) observation. However, the gravitational waves have not been detected directly yet. The direct detection of the gravitational waves is of great importance in physics to test the general relativity and in astronomy to open gravitational wave astronomy. Currently, one of the most promising methods to detect the gravitational waves directly is utilizing a laser interferometer to measure extremely small displacement ($\sim 10^{-21}$ m) of its mirrors. When the gravitational waves come to the interferometer, the differential length of its two arms changes. The first generation of interferometric gravitational wave detectors, such as LIGO in USA, VIRGO in Italy, GEO in Germany, and TAMA in Japan, have already been in operation, and several second-generation detectors are currently under construction, such as AdLIGO, AdVIRGO, and KAGRA (the Large-scale Cryogenic Gravitational wave Telescope (LCGT), a km-scale cryogenic detector project in Japan). KAGRA aims to detect the gravitational waves from coalescence of binary neutron stars more than once per year. Third-generation gravitational wave detectors, such as ET (the Einstein Telescope) in Europe, are also being planned. KAGRA and ET will enjoy two key advantages over other detectors: they will be constructed in an underground site with small seismic motion, and they will be equipped with cooled mirrors (at around 20 K in the case of KAGRA).

Cryogenic mirrors in gravitational-wave detectors

One of the largest advantages of the cryogenic mirrors is reduction of thermal noise. Thermoelastic noise in the mirror substrates, one of the thermal noise sources, is caused by thermoelastic damping. Thermoelastic damping is caused by heat flows between compressed (heated) and stretched (cooled) area when mirror has elastic vibration. While this thermoelastic noise is

approximately constant between 300 K and 50 K, it steeply decreases below around 50 K. The thermoelastic noise finally becomes lower than other thermal noise sources, becoming dominated by Brownian noise in the coating, at around 20 K. Therefore, design temperature of the KAGRA mirrors is 20 K, where the thermal noise of the mirrors is one order of magnitude smaller than that at 300 K.

In this thesis, I have developed the cryogenic techniques to be introduced in the gravitational wave detectors:

- Reduction of cooling time (main topic of this thesis)
- Technique of a pipe-shaped thermal radiation shield (duct shield)
 - Thermal radiation
 - Scattered light noise

Reduction of cooling time

The cooling time of the mirrors (several months in KAGRA) is one of the most important problems in the cryogenic gravitational wave detectors. KAGRA will have heating up and cooling down of the mirrors at least once per year. During that time, KAGRA cannot observe gravitational waves, and then KAGRA will miss gravitational wave events, such as the coalescence of binary neutron stars. Thus, the long cooling time decreases observation efficiency of the detectors, and it is necessary to reduce the cooling time. In the cryogenic interferometric gravitational wave detectors, such as KAGRA and ET, thermal conductors will be used to extract heat from the suspended mirror to keep the mirror cooled. To reduce vibration via the conductor, the mass to be cooled should be heavy, and the conductor should be long and thin wires. This is the main reason why it will take a long time to cool down the mirrors. On the other hand, continuous operation of the detectors causes reflectivity of the mirrors to decrease due to adsorption of water molecules on the mirrors. In KAGRA, water molecules will come from its beam duct with room temperature onto the mirrors. These molecules adsorbed by the mirrors will decrease the mirror reflectivity, the finesse of the cavity, and then the sensitivity to the gravitational waves. Frequency of the heating up and cooling down of the mirrors to remove the water molecules is estimated to be once per 300 days. Additionally, other maintenances could be necessary because of any other unexpected troubles.

In order to reduce cooling time, this thesis describes increasing thermal radiation. There are several methods for reducing the cooling time. One of them, increasing thermal radiation is a less effective method to extract heat from the mirrors than other methods. However, increasing radiation has a great advantage that it is simpler, namely, it avoids a use of a mechanical apparatus, which could cause troubles and sacrifice a high stability required for a large-scale detector.

Thermal radiation can be increased by using a high-emissivity material. There are many high-emissivity or black coatings in the world. However, in the interferometric gravitational wave detectors, ultra-high vacuum (2×10^{-7} Pa in KAGRA) is required since scattering of the laser light by gas molecules causes noise. Thus, the coating used to increase emissivity must be vacuum compatible. One of the most promising candidates in terms of the vacuum compatibility is a diamond-like carbon (DLC) coating, which is an intermediate material between diamond and graphite.

I constructed a calculation model of KAGRA cooling system, where heat is transferred by thermal radiation and thermal conduction. Then, how the cooling time can be reduced was calculated when the DLC coating was deposited on all the masses to be cooled down except the mirror. For this calculation, the following two experiments have been conducted. First of all, calculation of radiation heat transfer depends on whether the surfaces reflect rays of radiation diffusely or specularly. A small-scale experiment, where a sphere suspended inside a sphere-shaped vacuum chamber was cooled down by thermal radiation, has shown that the experimental results are consistent with calculation using the specular surfaces. The emissivity of the DLC coating was also obtained in this experiment. Experiments in the actual KAGRA cryostat, where a sphere or a half-sized payload was cooled down by thermal radiation, demonstrated the validity of the calculation model of thermal radiation and the effect of the DLC coating on the cooling time reduction. This experimental demonstration was for the first time in the world using an actual cryogenic interferometric detector since KAGRA is only one large-scale cryogenic interferometric detector so far in the world. As a result of these experiments, the calculated cooling time with the DLC coating is 39 days while it takes 58 days without any coating. As a result, a dramatic increase of the observation duty factor from 71% to 77% has been achieved based on the reduction in the cooling time. Then, the observation time of KAGRA for the gravitational wave events has increased.

Technique of a pipe-shaped thermal radiation shield

There is another problem to be solved to reduce the cooling time: the duct shields are necessary to reduce extra 300 K thermal radiation. The cryostats contain only the cryogenic mirrors, and not whole of the km-scale beam ducts, because it is difficult to cool the entire interferometer for its large scale. An opening in the shield is necessary to allow the laser beam to pass through. Large amount of 300 K thermal radiation would come through the opening. On the other hand, the amount of heat extractable from the mirror will be limited by the long and thin wires. Here, I conducted the calculation of thermal radiation passing through the duct shield. The result is that inserting several donut-shaped plates (baffles) can decrease thermal radiation below the requirement of KAGRA. On a basis of the calculation, three of all the eight KAGRA duct shields have been manufactured. Using the manufactured three duct shields, I measured thermal radiation input. The measured values were consistent with the calculation and the

manufactured three duct shields were found to be satisfied KAGRA requirement.

I also calculated scattered light noise caused by the duct shields. When the scattered laser beam by the mirror is reflected by something vibrating (e.g. the duct shields), the phase of the scattered light will be modulated by this vibration. If the scattered light comes back to the mirror and recombines to the main laser beam, it will affect the phase of the interferometer laser beam, and will cause noise. The calculation result satisfied requirement of KAGRA. I have demonstrated feasibility of the duct shields in terms of the thermal radiation and the scattered light noise using an actual cryogenic interferometric detector for the first time in the world.

Contents of this thesis

Chapter 2 reviews gravitational waves and an interferometer as a gravitational wave detector. Chapter 3 introduces readers to cryogenic techniques used for the interferometric gravitational wave detectors. The detail of KAGRA cooling system and its problem, a long cooling time, main topic of this thesis, is presented. Chapter 4 describes how to reduce the long cooling time. Effect of a high-emissivity coating is reported in calculation and experiments. Chapter 5 describes another problem to be solved to reduce the cooling time. Calculation and experiment of duct shields are reported. Chapter 6 concludes this research. Appendix A describes measurement of thermal conductivity of thin metal wires used in the cooling system of KAGRA, missed in the chapters above. Appendix B presents a sample code to calculate KAGRA cooling time for convenience of readers.

Chapter

2

Graviational waves

This chapter describes what gravitational waves (GWs) are, examples of calculations of GWs' waveforms and the principle of the most promising method to detect GWs directly, that is, a laser interferometer.[1, 2, 3, 4]

2.1 Derivation of GWs

In a 4-dimensional space-time, the interval ds is given as¹:

$$ds^2 = g_{\mu\nu} dx^\mu dx^\nu. \quad (2.1)$$

This chapter considers a metric:

$$g_{\mu\nu} = \eta_{\mu\nu} + h_{\mu\nu}, \quad |h_{\mu\nu}| \ll 1. \quad (2.2)$$

Here, $\eta_{\mu\nu}$ represents the flat space-time:

$$\eta_{\mu\nu} = \begin{pmatrix} -1 & 0 & 0 & 0 \\ 0 & 1 & 0 & 0 \\ 0 & 0 & 1 & 0 \\ 0 & 0 & 0 & 1 \end{pmatrix}. \quad (2.3)$$

Using the Christoffel symbol²:

$$\Gamma_{\mu\nu}^\rho = \frac{1}{2} g^{\rho\sigma} (\partial_\mu g_{\sigma\nu} + \partial_\nu g_{\sigma\mu} - \partial_\sigma g_{\mu\nu}), \quad (2.4)$$

¹Greek indices like μ, ν take values 0, 1, 2, 3. If they appear as superscript and subscript simultaneously in one term, they are summed: $x^\mu x_\mu$ means $\sum_{\mu=0}^3 x^\mu x_\mu$. $x^0 = ct$ is time multiplied by the light speed. $x^1 = x$, $x^2 = y$, $x^3 = z$ are spatial coordinate.

2

$$\partial_\mu \equiv \frac{\partial}{\partial x^\mu}$$

Riemann tensor:

$$R^\mu_{\nu\rho\sigma} = \partial_\rho \Gamma^\mu_{\nu\sigma} - \partial_\sigma \Gamma^\mu_{\nu\rho} + \Gamma^\mu_{\alpha\rho} \Gamma^\alpha_{\nu\sigma} - \Gamma^\mu_{\alpha\sigma} \Gamma^\alpha_{\nu\rho}, \quad (2.5)$$

Ricci tensor $R_{\mu\nu} = R^\alpha_{\mu\alpha\nu}$, and Ricci scalar $R = g^{\mu\nu} R_{\mu\nu}$, the Einstein equations are written as:

$$R_{\mu\nu} - \frac{1}{2} g_{\mu\nu} R = \frac{8\pi G}{c^4} T_{\mu\nu}, \quad (2.6)$$

where G is the Newtonian constant of gravitation and $T_{\mu\nu}$ is the energy-momentum tensor of matter. Equation (2.6) can be expanded to linear order in $h_{\mu\nu}$. First, the Riemann tensor is calculated to linear order in $h_{\mu\nu}$ as follows:

$$R_{\mu\nu\rho\sigma} = \frac{1}{2} (\partial_\nu \partial_\rho h_{\mu\sigma} + \partial_\mu \partial_\sigma h_{\nu\rho} - \partial_\mu \partial_\rho h_{\nu\sigma} - \partial_\nu \partial_\sigma h_{\mu\rho}). \quad (2.7)$$

The trace h of $h_{\mu\nu}$, and $\bar{h}_{\mu\nu}$ are defined as follows:

$$h = \eta^{\mu\nu} h_{\mu\nu} \quad (2.8)$$

and

$$\bar{h}_{\mu\nu} = h_{\mu\nu} - \frac{1}{2} \eta_{\mu\nu} h. \quad (2.9)$$

Using this $\bar{h}_{\mu\nu}$, eq.(2.6) is rewritten as:

$$\square \bar{h}_{\mu\nu} + \eta_{\mu\nu} \partial^\rho \partial^\sigma \bar{h}_{\rho\sigma} - \partial^\rho \partial_\nu \bar{h}_{\mu\rho} - \partial^\rho \partial_\mu \bar{h}_{\nu\rho} = -\frac{16\pi G}{c^4} T_{\mu\nu}. \quad (2.10)$$

Here, one can choose the Lorentz gauge:

$$\partial^\nu \bar{h}_{\mu\nu} = 0, \quad (2.11)$$

and obtain a differential equation:

$$\square \bar{h}_{\mu\nu} = -\frac{16\pi G}{c^4} T_{\mu\nu}. \quad (2.12)$$

Here, eq.(2.11) has reduced independent degrees of freedom in the symmetric tensor $h_{\mu\nu}$ from 10 to 6. Outside the wave source, $T_{\mu\nu} = 0$, one obtains:

$$\square \bar{h}_{\mu\nu} = 0. \quad (2.13)$$

In addition, one can choose the coordinate that satisfies the condition:

$$\bar{h} = 0, h^{0i} = 0. \quad (2.14)$$

This can decrease the independent degrees of freedom in $h_{\mu\nu}$ from 6 to 2. To the end, one obtains:

$$h^{0\mu} = 0, h^i_i = 0, \partial^j h_{ij} = 0. \quad (2.15)$$

(the transverse-traceless gauge or TT gauge). Equation (2.13) has plane-wave solutions $h_{ij}^{TT}(x) = e_{ij}(\mathbf{k})e^{ikx}$. Assuming that $\hat{\mathbf{n}} = \mathbf{k}/|\mathbf{k}|$ is toward the z direction, one can obtain:

$$h_{ab}^{TT}(t, z) = \begin{pmatrix} h_+ & h_\times \\ h_\times & -h_+ \end{pmatrix}_{ab} \cos \left[\omega \left(t - \frac{z}{c} \right) \right]. \quad (2.16)$$

In this case, an interval is given as:

$$\begin{aligned} ds^2 &= -c^2 dt^2 + (\delta_{ij} + h_{ij}^{TT}) dx^i dx^j \\ &= -c^2 dt^2 + dz^2 + \left\{ 1 + h_+ \cos \left[\omega \left(t - \frac{z}{c} \right) \right] \right\} dx^2 + \left\{ 1 - h_+ \cos \left[\omega \left(t - \frac{z}{c} \right) \right] \right\} dy^2 \\ &\quad + 2h_\times \cos \left[\omega \left(t - \frac{z}{c} \right) \right] dx dy. \end{aligned} \quad (2.17)$$

2.2 Quadrupole radiation

A solution of eq.(2.12) is given as:

$$\bar{h}_{\mu\nu}(t, \mathbf{x}) = \frac{4G}{c^4} \int d^3x' \frac{1}{|\mathbf{x} - \mathbf{x}'|} T_{\mu\nu} \left(t - \frac{|\mathbf{x} - \mathbf{x}'|}{c}, \mathbf{x}' \right). \quad (2.18)$$

Assuming that $r \gg d$ and $v \ll c$ (nonrelativistic), where d is the typical length scale of the wave source and r is the distance from the wave source \mathbf{x}' to the observation point \mathbf{x} , one can obtain the terms of the lowest order (the quadrupole radiation) as:

$$[h_{ij}^{TT}(t, \mathbf{x})]_{\text{quad}} = \frac{1}{r} \frac{2G}{c^4} \Lambda_{ij,kl}(\hat{\mathbf{n}}) \ddot{M}_{kl}(t - r/c) = \frac{1}{r} \frac{2G}{c^4} \Lambda_{ij,kl}(\hat{\mathbf{n}}) \ddot{Q}_{kl}(t - r/c). \quad (2.19)$$

Here, $\Lambda_{ij,kl}(\hat{\mathbf{n}})$, called lambda tensor, includes information about the direction of radiation of GWs; M^{ij} is the second mass moment and Q^{ij} is the quadrupole moment; their definitions are as follows:

$$\Lambda_{ij,kl}(\hat{\mathbf{n}}) = P_{ik}P_{jl} - \frac{1}{2}P_{ij}P_{kl} \quad (P_{ij}(\hat{\mathbf{n}}) = \delta_{ij} - n_i n_j) \quad (2.20)$$

$$M^{ij} = \int d^3x \rho(t, \mathbf{x}) x^i x^j, \quad (2.21)$$

$$Q^{ij} = M^{ij} - \frac{1}{3} \delta^{ij} M_{kk} = \int d^3x \rho(t, \mathbf{x}) \left(x^i x^j - \frac{1}{3} r^2 \delta^{ij} \right), \quad (2.22)$$

where $\rho(t, \mathbf{x})$ is the mass density. Using the energy-momentum tensor, one can obtain energy per unit time radiated by the quadrupole radiation:

$$P_{\text{quad}} = \frac{G}{2c^5} \langle \ddot{Q}_{ij} \ddot{Q}_{ij} \rangle = \frac{G}{2c^5} \langle \ddot{M}_{ij} \ddot{M}_{ij} - \frac{1}{3} (\ddot{M}_{kk})^2 \rangle, \quad (2.23)$$

where $\langle \cdots \rangle$ represents an average over several periods of the mass motion. Next, examples of the quadrupole radiation are given.

2.2.1 Oscillating masses

Two masses connected with a spring are considered and the relative coordinate is written as:

$$z_0(t) = a \cos \omega_s t. \quad (2.24)$$

The mass density, using the reduced mass μ , is represented as:

$$\rho(t, \mathbf{x}) = \mu \delta(x) \delta(y) \delta(z - z_0(t)), \quad (2.25)$$

and then

$$\begin{aligned} M^{ij} &= \int d^3x \rho(t, \mathbf{x}) x^i x^j \\ &= \mu z_0^2(t) \delta^{i3} \delta^{j3} \\ &= \mu a^2 \frac{1 + \cos 2\omega_s t}{2} \delta^{i3} \delta^{j3}. \end{aligned} \quad (2.26)$$

From eq.(2.19), one can obtain:

$$h_+(t) = \frac{2G\mu a^2 \omega_s^2}{rc^4} \sin^2 \iota \cos(2\omega_s t), \quad (2.27)$$

$$h_\times(t) = 0, \quad (2.28)$$

where ι is the angle between the z axis and the direction of the observer. h_+ vanishes when the observer is in the direction of the z axis. The angular frequency of GWs is just two-times larger than that of the oscillation of the masses. From eq.(2.23),

$$P_{\text{quad}} = \frac{16}{15} \frac{G\mu^2}{c^5} a^4 \omega_s^6. \quad (2.29)$$

2.2.2 Masses in a circular orbit (model of a binary pulsar)

Two masses m_1, m_2 moving along a circular orbit are considered, the relative coordinate is assumed as:

$$x_0(t) = R \cos \left(\omega_s t + \frac{\pi}{2} \right), \quad (2.30)$$

$$y_0(t) = R \sin \left(\omega_s t + \frac{\pi}{2} \right), \quad (2.31)$$

$$z_0(t) = 0. \quad (2.32)$$

Using

$$M^{ij} = \mu x_0^i(t) x_0^j(t), \quad (2.33)$$

where $\mu = m_1 m_2 / (m_1 + m_2)$ is the reduced mass, eq.(2.19) is written as:

$$h_+(t) = \frac{1}{r} \frac{4G\mu\omega_s^2 R^2}{c^4} \left(\frac{1 + \cos^2 \iota}{2} \right) \cos(2\omega_s t), \quad (2.34)$$

$$h_\times(t) = \frac{1}{r} \frac{4G\mu\omega_s^2 R^2}{c^4} \cos \iota \sin(2\omega_s t). \quad (2.35)$$

Here, ι is the angle between the normal of the orbit and the direction of the observer. When $\iota = \pi/2$, namely, the observer is on the orbital plane, h_\times vanishes. On the other hand, when the observer is in the direction of the normal of the orbital plane ($\iota = 0$), h_+ and h_\times have the same amplitude and change as $\cos(2\omega_s t)$ and $\sin(2\omega_s t)$, respectively. The typical value is calculated as:

$$h_0 = \frac{1}{r} \frac{4G\mu\omega_s^2 R^2}{c^4} = \frac{4}{r} \left(\frac{GM_c}{c^2} \right)^{5/3} \left(\frac{\pi f_{\text{gw}}}{c} \right)^{2/3} \quad (2.36)$$

$$\simeq 2.56 \times 10^{-23} \left(\frac{100 \text{ Mpc}}{r} \right) \left(\frac{M_c}{M_{\text{solar}}} \right)^{5/3} \left(\frac{f_{\text{gw}}}{100 \text{ Hz}} \right)^{2/3}. \quad (2.37)$$

Here, the chirp mass $M_c = (m_1 m_2)^{3/5} / (m_1 + m_2)^{1/5}$, the frequency of GWs f_{gw} satisfying $2\pi f_{\text{gw}} = 2\omega_s$, and Kepler's law:

$$\omega_s^2 = \frac{G(m_1 + m_2)}{R^3} \quad (2.38)$$

are used. f_{gw} reaches 100 Hz during the last several seconds to coalescence in the case that M_c is equal to the solar mass M_{solar} . Moreover, eq.(2.23) is calculated as:

$$P_{\text{quad}} = \frac{32}{5} \frac{G\mu^2}{c^5} R^4 \omega_s^6. \quad (2.39)$$

2.2.3 A Rotating rigid body (model of a neutron star)

Let us consider the coordinate where the inertia tensor of a rigid body is diagonalized. Now, a rigid body whose principal moments of inertia are I_1, I_2, I_3 around the x, y, z axes respectively is rotating around the z axis with an angular velocity ω_s and a frequency f_{rot} . Using a relation that

$$M_{ij} = -I_{ij} + c_{ij}, \quad (2.40)$$

where I_{ij} is the inertia tensor and c_{ij} is a constant tensor, eq.(2.19) is written as:

$$\begin{aligned} h_+(t) &= h_0 \frac{1 + \cos^2 \iota}{2} \cos(2\omega_s t), \\ h_\times(t) &= h_0 \cos \iota \sin(2\omega_s t), \end{aligned} \quad (2.41)$$

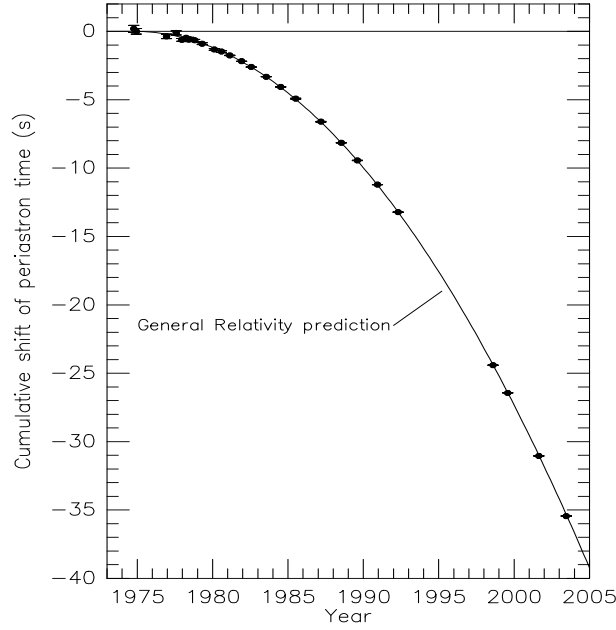


Figure 2.1: Change in the period of the Hulse Taylor binary pulsar PSR B1913+16. “Orbital decay of PSR B1913+16. The data points indicate the observed change in the epoch of periastron with date while the parabola illustrates the theoretically expected change in epoch for a system emitting gravitational radiation, according to general relativity.” [5]

where

$$h_0 = \frac{4\pi^2 G}{c^4} \frac{I_3 f_{\text{gw}}^2}{r} \epsilon. \quad (2.42)$$

Now, $f_{\text{gw}} = 2f_{\text{rot}}$ is the frequency of GWs, which is equal to twice the rotational frequency of the rigid body f_{rot} . Also,

$$\epsilon \equiv \frac{I_1 - I_2}{I_3} \quad (2.43)$$

is the ellipticity. The typical value is represented as:

$$h_0 \simeq 1.06 \times 10^{-27} \left(\frac{\epsilon}{10^{-6}} \right) \left(\frac{I_3}{10^{38} \text{ kg m}^2} \right) \left(\frac{10 \text{ kpc}}{r} \right) \left(\frac{f_{\text{gw}}}{100 \text{ Hz}} \right)^2. \quad (2.44)$$

Here, $I_3 \sim M_{\text{solar}} a_{\text{ns}}^2$, where $a_{\text{ns}} = 10 \text{ km}$ is a typical radius of neutron stars. In addition, eq.(2.23) is written as:

$$P = \frac{32G}{5c^5} \epsilon^2 I_3^2 \omega_s^6. \quad (2.45)$$

2.3 An indirect proof of the existence of GWs

Equation (2.23), derived from the theory of general relativity, is consistent with the observed result concerning the change in the period of the Hulse Taylor binary pulsar PSR B1913+16 caused by its radiation of GWs.[5] The orbital phase $\phi_b(T)$ at time T , using the orbital frequency ν_b , is given as:

$$\frac{1}{2\pi}\phi_b(T) = \nu_b T + \frac{1}{2}\dot{\nu}_b T^2 + \dots \quad (2.46)$$

When it passes the periastron for the n th time, $\phi_b(T_n) = 2\pi n$,

$$\nu_b T_n + \frac{1}{2}\dot{\nu}_b T_n^2 = n, \quad (2.47)$$

and thus

$$T_n - \frac{n}{\nu_b} = -\frac{\dot{\nu}_b}{2\nu_b^2} T_n^2. \quad (2.48)$$

Or, using the orbital period $P_b = 1/\nu_b$,

$$T_n - P_b n = \frac{\dot{P}_b}{2P_b} T_n^2. \quad (2.49)$$

The theoretical values and experimental values are plotted in Figure 2.1. The experimental value of \dot{P}_b is consistent with the theoretical value at the $(0.13 \pm 0.21) \%$ level.[5]

2.4 Principle of detecting GWs

There are observations which can be explained by existence of the GWs, such as one described in Subsection 2.3. Although many experiments to detect the GWs have been conducted, the GWs have not been detected directly yet. Hereafter, this chapter describes one of the most promising methods, namely an interferometer.

2.4.1 Phase shift in a Michelson interferometer due to GWs

In the Michelson interferometer shown in Figure 2.2, the current of the photo detector changes as:

$$I_P = \frac{I_{\max} + I_{\min}}{2} + \frac{(I_{\max} - I_{\min}) \cos(\phi_1 - \phi_2)}{2}. \quad (2.50)$$

Here, ϕ_1 , and ϕ_2 are phases of laser light travelling along x , and y axis, respectively. The current I_P can detect the phase difference $\phi_1 - \phi_2$, namely length difference of the two arms.

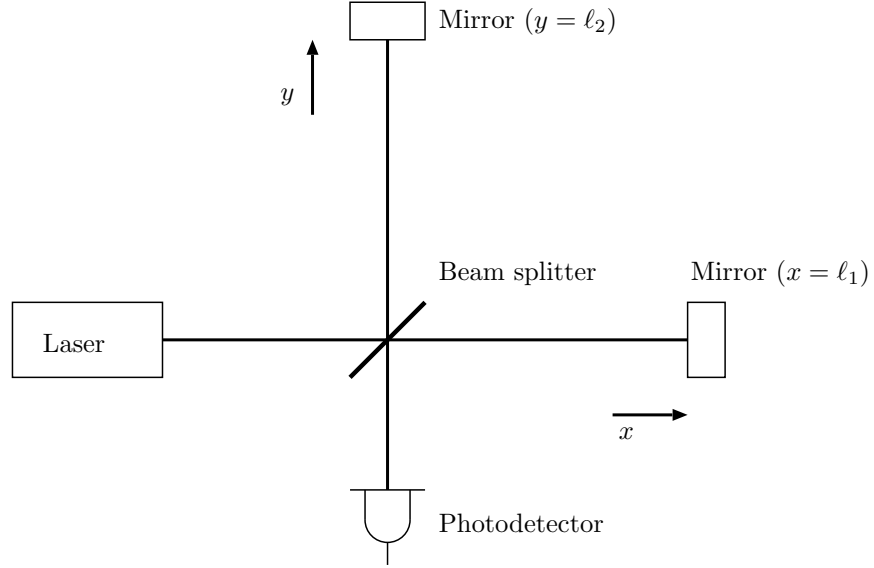


Figure 2.2: Michelson interferometer. The origin is on the beam splitter and x, y axes are set to the direction represented by the arrows. The light from the laser is split by a beam splitter. Then, the light travels to the mirrors, returns to the beam splitter, where the two beams interfere. The change of the interference is detected by a photodetector.

Next, let us think about the phase shift produced by GWs. Using the 4-dimensional infinitesimal length:

$$ds^2 = -c^2 dt^2 + (1 + h)dx^2 + (1 - h)dy^2 + dz^2, \quad (2.51)$$

the velocity of light that makes a round trip along the x axis is given as:

$$\frac{dx}{dt} = \pm \frac{c}{\sqrt{1 + h(t)}}. \quad (2.52)$$

Integrating eq.(2.52) from τ_1 to t produces the following relation:

$$\frac{2\ell_1}{c} = \int_{\tau_1}^t \frac{dt'}{\sqrt{1 + h(t')}} \approx \int_{\tau_1}^t \left[1 - \frac{1}{2}h(t') \right] dt' = t - \tau_1 - \frac{1}{2} \int_{\tau_1}^t h(t') dt', \quad (2.53)$$

where the light comes in the beam splitter at time τ_1 , makes a round trip on the distance ℓ_1 and comes back to the beam splitter at time t . The lower limit of the integral in the third term of the right-hand side is approximately $\tau_1 = t - 2\ell_1/c$, considering this equation to a linear order in h ; and then, the phase of the light is given as:

$$\phi_1(t) = \Omega\tau_1 = \Omega \left[t - \frac{2\ell_1}{c} - \frac{1}{2} \int_{t-2\ell_1/c}^t h(t') dt' \right]. \quad (2.54)$$

Because the effect of GWs has an opposite sign on the y axis, the phase shift is represented as:

$$\Delta\phi = \phi_1 - \phi_2 = -\frac{2\Omega(\ell_1 - \ell_2)}{c} - \Delta\phi_{\text{GR}}(t), \quad (2.55)$$

$$\Delta\phi_{\text{GR}}(t) = \Omega \int_{t-2\ell/c}^t h(t') dt' \quad (\ell_2 \approx \ell_1 = \ell). \quad (2.56)$$

2.4.2 Response function and arm length

When h changes slowly, eq.(2.56) is simplified as:

$$\Delta\phi_{\text{GR}}(t) \approx \frac{4\pi}{\lambda} h(t) \ell, \quad (2.57)$$

which shows that the sensitivity becomes higher for the longer arm length. However, this fact holds only when $\omega \ll c/\ell$. Generally, the response function of $h(t)$ to $\Delta\phi_{\text{GR}}(t)$ is written as:

$$H_{\text{M}}(\omega) = \frac{2\Omega}{\omega} \sin(\ell\omega/c) e^{-i\ell\omega/c}. \quad (2.58)$$

The modulus of eq.(2.58) is given in Figure 2.3, which shows that the longer arm length limits the band width.

2.5 Fabry-Perot interferometer as a gravitational wave detector

2.5.1 Fabry-Perot interferometer

As shown in eq.(2.57), the phase shift due to low-frequency GWs is proportional to the arm length. Here, a method to increase effective arm length with many round trips of light inside cavities is introduced.

In a Fabry-Perot cavity, where two mirrors are set facing each other, as shown in Figure 2.4, the light goes back and forth many times. Only light with a certain wavelength resonates and has a large transmission intensity. Parameters r and t are defined as the reflectivity and transmissivity of the mirrors, respectively. When an incident light wave $A_i(t) = e^{i\Omega t}$ comes to the cavity (Figure 2.4), the reflection is represented as:

$$A_r(t) = r_1 e^{i\Omega t} - \frac{t_1^2}{r_1} \sum_{n=1}^{\infty} (r_1 r_2)^n \exp(i\Omega \tau_n) \quad \left(\tau_n = t - \frac{2\ell}{c} n \right); \quad (2.59)$$

namely,

$$A_r(t) = e^{i\Omega t} [r_1 - a(\Omega)], \quad (2.60)$$

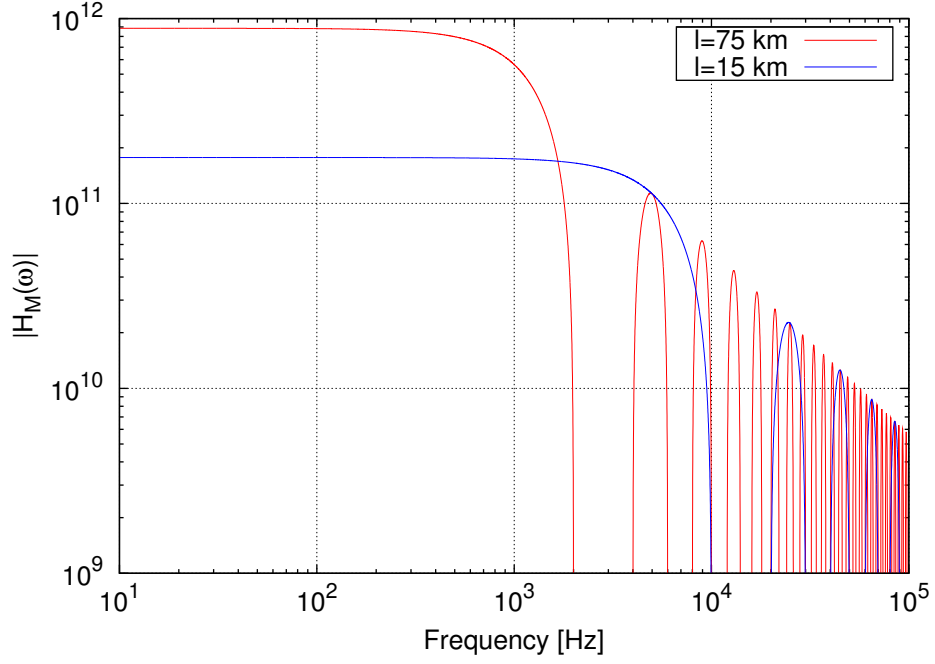


Figure 2.3: Response function of a Michelson interferometer. Here, the wavelength of the laser is $\lambda = 1064$ nm.

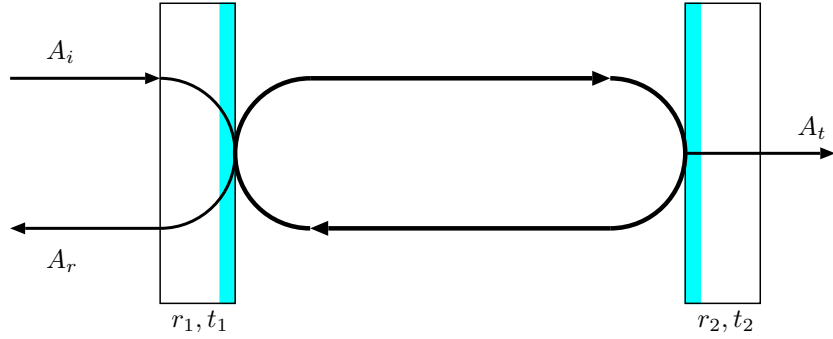


Figure 2.4: Fabry-Perot cavity

$$a(\Omega) = \frac{t_1^2 r_2 \exp(-2i\Omega\ell/c)}{1 - r_1 r_2 \exp(-2i\Omega\ell/c)}. \quad (2.61)$$

If loss in the first mirror is negligible: $r_1^2 + t_1^2 = 1$,

$$A_r(t) = e^{i\Omega t} \frac{r_1 - r_2 \exp(-2i\Omega\ell/c)}{1 - r_1 r_2 \exp(-2i\Omega\ell/c)}. \quad (2.62)$$

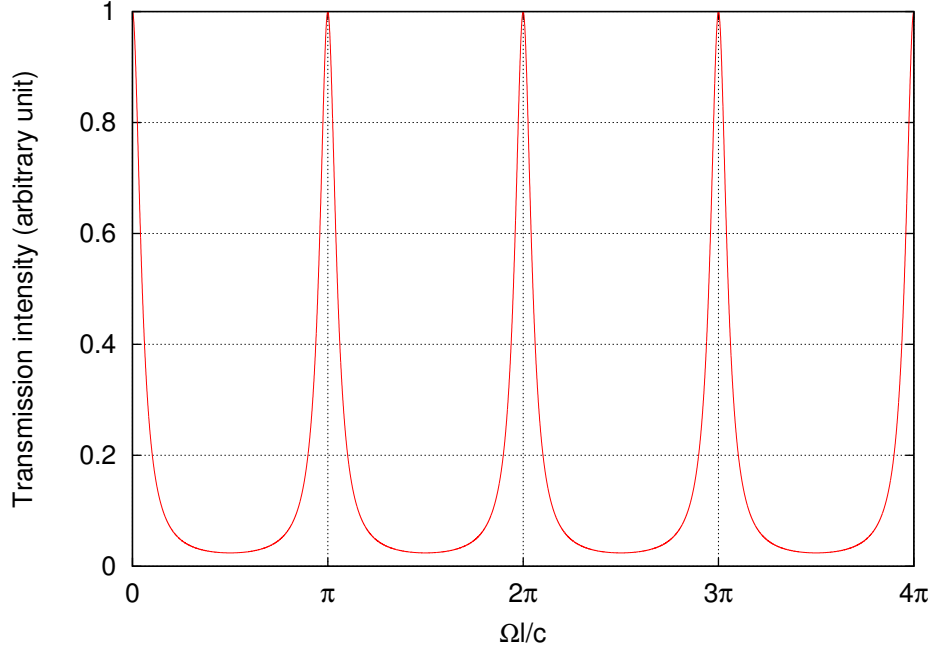


Figure 2.5: Transmission intensity of Fabry-Perot interferometer. Here, the finesse is 10.

Similarly, the field inside the cavity at the left mirror is:

$$A_{\text{cav}}(t) = e^{i\Omega t} \frac{t_1}{1 - r_1 r_2 e^{-2i\Omega\ell/c}}, \quad (2.63)$$

and the transmission is simply given by the product of A_{cav} and $\exp(-i\Omega\ell/c)t_2$:

$$A_t(t) = e^{i\Omega(t-\ell/c)} \frac{t_1 t_2}{1 - r_1 r_2 e^{-2i\Omega\ell/c}}. \quad (2.64)$$

The power inside the cavity is proportional to $|A_{\text{cav}}(t)|^2$:

$$|A_{\text{cav}}(t)|^2 = \left(\frac{t_1}{1 - r_1 r_2} \right)^2 \frac{1}{1 + F \sin^2(\Omega\ell/c)}, \quad (2.65)$$

where

$$F = \frac{4r_1 r_2}{(1 - r_1 r_2)^2}. \quad (2.66)$$

The transmission intensity has the same dependence on Ω :

$$|A_t(t)|^2 \propto \frac{1}{1 + F \sin^2(\Omega\ell/c)}. \quad (2.67)$$

When $\Omega\ell/c = n\pi$ (n is an integer), the intensity of the transmission takes the maximum value, as shown in Figure 2.5. The interval between the n th and the $(n+1)$ th frequency:

$$\nu_{n+1} - \nu_n = \frac{c}{2\ell} = \nu_{\text{FSR}} \quad (2.68)$$

is called free spectral range (FSR) of the Fabry-Perot cavity. The full width at half maximum (FWHM) of the resonance $\Delta\nu$ is:

$$\frac{1}{1 + F \sin^2 \left(\frac{2\pi\Delta\nu}{2} \frac{\ell}{c} \right)} = \frac{1}{2}. \quad (2.69)$$

When $\Delta\nu$ is sufficiently small,

$$\Delta\nu = \frac{c}{\pi\ell\sqrt{F}} = \frac{2}{\pi\sqrt{F}}\nu_{\text{FSR}}. \quad (2.70)$$

Then, defining finesse as:

$$\mathcal{F} = \frac{\pi\sqrt{F}}{2} = \frac{\pi\sqrt{r_1 r_2}}{1 - r_1 r_2}, \quad (2.71)$$

it is represented as:

$$\mathcal{F} = \frac{\nu_{\text{FSR}}}{\Delta\nu}. \quad (2.72)$$

Here, storage time in the cavity is described, which shows that finesse is roughly the effective number of the round trip in the cavity. If $r_2 = 1$, probability that the photon comes out after n round trips $p(n)$ is proportional to r_1^{2n} :

$$p(n) = \frac{r_1^{2n}}{\sum_{n=1}^{\infty} r_1^{2n}}. \quad (2.73)$$

The average number of n is given as:

$$\sum_{n=1}^{\infty} np(n) = \frac{1}{1 - r_1^2}. \quad (2.74)$$

Thus, storage time, namely the average time spent by the photons in the cavity, is

$$\tau_s = \frac{2\ell}{c} \frac{1}{1 - r_1^2} \simeq \frac{\ell}{c} \frac{\mathcal{F}}{\pi} \quad (2.75)$$

using eq.(2.71) and the fact that r_1 is close to one.

Now, phase ϕ of eq.(2.62) when $\Omega\ell/c$ is slightly shifted from the resonance $n\pi$ is described. Phases of numerator and denominator of eq.(2.62) ϕ_n and ϕ_d satisfy the following equations:

$$\tan \phi_n = -\frac{r_2 \sin(2\Omega\ell/c)}{r_1 - r_2 \cos(2\Omega\ell/c)}, \quad (2.76)$$

$$\tan \phi_d = -\frac{r_1 r_2 \sin(2\Omega\ell/c)}{1 - r_1 r_2 \cos(2\Omega\ell/c)}. \quad (2.77)$$

Phase ϕ of A_r is given as:

$$\phi = \phi_n - \phi_d. \quad (2.78)$$

Assuming $r_2 = 1$ and

$$\frac{2\Omega\ell}{c} = 2n\pi + \epsilon, \quad (2.79)$$

we obtain with eq.(2.71):

$$\frac{\partial\phi}{\partial\epsilon} = \frac{1+r_1}{1-r_1} \simeq \frac{2\mathcal{F}}{\pi} \quad (2.80)$$

when r_1 is close to one. If the length of arm changes by $\Delta\ell$, ϕ changes as:

$$\Delta\phi = \frac{4\mathcal{F}\Omega}{\pi c} \Delta\ell. \quad (2.81)$$

2.5.2 Response of the Fabry-Perot interferometer to GWs

The condition of τ_n :

$$\int_{\tau_n}^t \frac{dt'}{\sqrt{1+h(t')}} = \frac{2\ell}{c} n \quad (2.82)$$

yields the relation to the order of magnitude h :

$$e^{i\Omega\tau_n} = e^{i\Omega(t-2\ell n/c)} \left[1 - i\frac{\Omega}{2} \int h(\omega) e^{i\omega t} \frac{1 - e^{-2i\omega\ell n/c}}{i\omega} d\omega \right]. \quad (2.83)$$

Using this equation, the reflection is written as:

$$A_r(t) = e^{i\Omega t} \left[r_1 - a(\Omega) + \frac{i\Omega}{2} \int h(\omega) \frac{a(\Omega) - a(\Omega + \omega)}{i\omega} e^{i\omega t} d\omega \right]. \quad (2.84)$$

When the light is resonant in the cavity, namely $e^{-2i\Omega\ell/c} = 1$,

$$A_r(t) = e^{i\Omega t} (r_1 - \alpha_c + i\Delta_{\text{GR}}(t)/2), \quad (2.85)$$

$$\Delta_{\text{GR}}(t) = \int h(\omega) e^{i\omega t} H_{\text{FP}}(\omega) d\omega, \quad (2.86)$$

$$H_{\text{FP}}(\omega) = \frac{2\alpha_c\Omega}{\omega} \sin(\ell\omega/c) e^{-i\omega\ell/c} \frac{1}{1 - r_1 r_2 \exp(-2i\omega\ell/c)}, \quad (2.87)$$

$$\alpha_c = \frac{t_1^2 r_2}{1 - r_1 r_2} \simeq 1 + r_1 \sim 2. \quad (2.88)$$

Here, $i\Delta_{\text{GR}}$ represents the side band produced by GWs. α_c is approximated as $1 + r_1$ when $r_2 = 1$ and $r_1^2 + t_1^2 = 1$. The modulus of eq.(2.87) is given as:

$$|H_{\text{FP}}(\omega)| = \frac{2\alpha_c\Omega}{\omega(1 - r_1 r_2)} \frac{|\sin(\omega\ell/c)|}{\sqrt{1 + F \sin^2(\omega\ell/c)}}. \quad (2.89)$$

When $\omega \ll c/\ell$,

$$|H_{\text{FP}}(\omega)| = \frac{4\mathcal{F}\Omega\ell}{\pi} \frac{1}{c} \frac{1}{\sqrt{1 + (\omega\tau)^2}}, \quad (2.90)$$

where $\tau = 2\tau_s = 2\mathcal{F}\ell/(\pi c)$. This function is plotted in Figure 2.6.

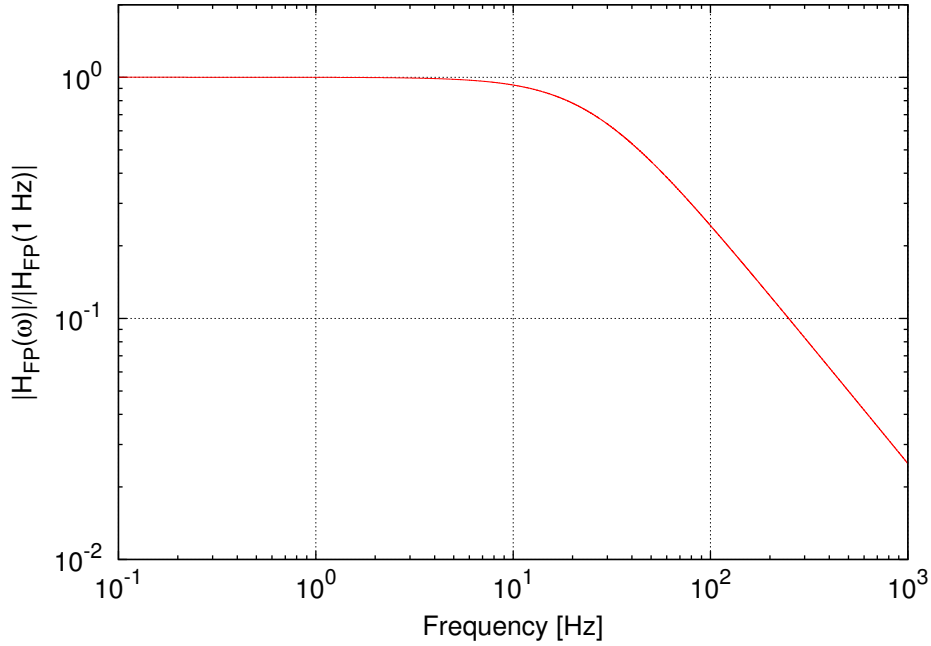


Figure 2.6: Response function of Fabry-Perot interferometer. Here, the finesse is 1000 and the arm length is 3 km.

2.6 Noise in an interferometer

There is several noise sources to limit the interferometer sensitivity to the GWs. This section describes main noise sources of the interferometric detectors.

2.6.1 Shot noise of photon

Shot noise comes from statistical fluctuations of the number of photons, or electrons generated by the photodetector. The power spectrum of the shot noise of the photocurrent I_P is given as:

$$\langle i_n^2 \rangle = 2eI_P. \quad (2.91)$$

In eq.(2.50), using $\Delta\phi = \phi_1 - \phi_2 = \Phi_0 + \delta\phi$ and $I_{\text{eff}} = I_{\text{max}} - I_{\text{min}}$, the differential photocurrent is

$$\delta I_P = -\frac{I_{\text{eff}}}{2} \sin \Phi_0 \cdot \delta\phi. \quad (2.92)$$

If this is equal to the shot noise of the photocurrent, the following relations are derived by using an observable bandwidth Δf ,

$$\frac{I_{\text{eff}}}{2} \sin \Phi_0 \cdot \delta\phi_{\text{min}} = \sqrt{2eI_{\text{dc}}\Delta f}, \quad (2.93)$$

$$I_{\text{dc}} = \frac{I_{\text{max}} + I_{\text{min}} + I_{\text{eff}} \cos \Phi_0}{2}. \quad (2.94)$$

In an ideal case of $I_{\text{min}} = 0$,

$$\delta\phi_{\text{min}} = \frac{\sqrt{eI_{\text{max}}(1 + \cos \Phi_0)\Delta f}}{\frac{I_{\text{max}}}{2} \sin \Phi_0} = \sqrt{\frac{2e}{I_{\text{max}}}\Delta f} \frac{1}{\sin \frac{\Phi_0}{2}}. \quad (2.95)$$

This has the minimum value at a dark fringe $\Phi_0 = \pi$. Using

$$I_{\text{max}} = e \frac{\eta P}{\hbar\Omega}, \quad (2.96)$$

where P is the power of the laser and η is the quantum efficiency of the photodetector,

$$\delta\phi_{\text{min}} = \sqrt{\frac{2\hbar\Omega}{\eta P}\Delta f}. \quad (2.97)$$

In case of the Fabry-Perot interferometer, the equivalent GWs' amplitude h_{shot} , which causes the same phase shift as $\delta\phi_{\text{min}}$, satisfies relation as:

$$\delta\phi_{\text{min}} = |H_{\text{FP}}| h_{\text{shot}} \Delta f, \quad (2.98)$$

using the transfer function H_{FP} from h to ϕ . Substituting eq.(2.90) yields equation:

$$h_{\text{shot}} = \frac{\pi c}{2\mathcal{F}\ell} \sqrt{\frac{\hbar}{2\Omega P}} \sqrt{1 + (\omega\tau)^2}, \quad (2.99)$$

assuming $\eta = 1$.

2.6.2 Radiation pressure noise

When the light is reflected by the mirror, the mirror receives the momentum change of the light. When the number of photons fluctuates, the force to the mirror, and then the position of the mirror consequently fluctuate, which is called radiation pressure noise.

Michelson interferometer

The force to the mirror is equal to the momentum change per unit time:

$$f_{\text{ba}} = 2 \frac{\hbar\Omega}{c} \frac{P}{\hbar\Omega} = \frac{2P}{c}, \quad (2.100)$$

where P is the power of the incident light. Using the mass of the mirror M , the equation of motion is represented as:

$$M \frac{d^2 x}{dt^2} = f_{\text{ba}}, \quad (2.101)$$

that is, in spectrum,

$$\langle x_{\text{ba}}^2(\omega) \rangle = \frac{4\langle \delta P^2(\omega) \rangle}{(M\omega^2 c)^2}. \quad (2.102)$$

When the incident light is in a coherent state,

$$\langle \delta P^2(\omega) \rangle = 2\hbar\Omega P, \quad (2.103)$$

and

$$\langle x_{\text{ba}}^2(\omega) \rangle = \frac{8\hbar\Omega P}{(M\omega^2 c)^2}. \quad (2.104)$$

The equivalent GWs' amplitude is given as:

$$h_{\text{rad}} = \frac{2}{\ell} \sqrt{\langle x(\omega)_{\text{ba}}^2 \rangle} = \frac{2}{\ell} \sqrt{\frac{8\hbar\Omega P}{M\omega^2 c}}. \quad (2.105)$$

Fabry-Perot interferometer

In case of the Fabry-Perot interferometer, the power inside the cavity should be taken into account. Equation (2.65) is written as:

$$|A_{\text{cav}}(t)|^2 = \frac{2\mathcal{F}}{\pi} \frac{1}{1 + \left(\frac{2\mathcal{F}}{\pi}\right)^2 \sin^2(\Omega\ell/c)}, \quad (2.106)$$

assuming that $r_1^2 + t_1^2 = 1$, $r_2 = 1$, and $r_1 \sim 1$. When the cavity is resonant $\Omega\ell/c = n\pi$ and the mirrors vibrate at angular frequency ω , the power inside the cavity P_{cav} and the power at the beam splitter P_{bs} have a relation as:

$$P_{\text{cav}} = \frac{2\mathcal{F}}{\pi} \frac{1}{1 + (\omega\tau)^2} P_{\text{bs}}. \quad (2.107)$$

Using this equation, eq.(2.100) is written as:

$$f_{\text{ba}} = \frac{2P_{\text{cav}}}{c} = \frac{2P_{\text{bs}}}{c} \frac{2\mathcal{F}}{\pi} \frac{1}{1 + (\omega\tau)^2}. \quad (2.108)$$

Then we obtain equation:

$$\langle x_{\text{ba}}^2(\omega) \rangle = \frac{8\hbar\Omega P}{(M\omega^2 c)^2} \left[\frac{2\mathcal{F}}{\pi} \frac{1}{1 + (\omega\tau)^2} \right]^2. \quad (2.109)$$

instead of eq.(2.104). Since gravitational waves h cause the phase shift $\Delta\phi = |H_{\text{FP}}| h \Delta f$, comparison of eq.(2.81) and eq.(2.90) yields relation as:

$$h_{\text{rad}} = \frac{2}{\ell} \sqrt{\langle x(\omega)_{\text{ba}}^2 \rangle} \sqrt{1 + (\omega\tau)^2} = \frac{2}{\ell} \frac{\sqrt{8\hbar\Omega P}}{M\omega^2 c} \frac{2\mathcal{F}}{\pi} \frac{1}{\sqrt{1 + (\omega\tau)^2}}. \quad (2.110)$$

2.6.3 Quantum limit

This subsection describes the quantum uncertainty principle. Operators of the position and the momentum of a free mass are represented as:

$$\hat{x}(t) = \hat{x}(0) + \frac{\hat{p}(0)t}{m}, \quad (2.111)$$

$$\hat{p}(t) = \hat{p}(0). \quad (2.112)$$

At a certain time τ_0 ,

$$\langle \Delta\hat{x}(\tau_0)^2 \rangle = \langle \Delta\hat{x}(0)^2 \rangle + \langle \Delta\hat{p}(0)^2 \rangle \frac{\tau_0^2}{m^2} + \langle \Delta\hat{x}(0)\Delta\hat{p}(0) + \Delta\hat{p}(0)\Delta\hat{x}(0) \rangle \frac{\tau_0}{m}. \quad (2.113)$$

If the third term of eq.(2.113) is negligible, the uncertainty principle

$$\sqrt{\langle \Delta \hat{x}(0)^2 \rangle \langle \Delta \hat{p}(0)^2 \rangle} \geq \frac{\hbar}{2} \quad (2.114)$$

yields equation:

$$\langle \Delta \hat{x}(\tau_0)^2 \rangle \geq \langle \Delta \hat{x}(0)^2 \rangle + \frac{1}{\langle \Delta \hat{x}(0)^2 \rangle} \left(\frac{\hbar \tau_0}{2m} \right)^2 \geq \frac{\hbar \tau_0}{m}. \quad (2.115)$$

The equal sign holds when

$$\sqrt{\langle \Delta \hat{x}(0)^2 \rangle} = \sqrt{\frac{\hbar \tau_0}{2m}} = \Delta X_{\text{SQL}}, \quad (2.116)$$

where ΔX_{SQL} is called standard quantum limit.

In the case of a Michelson interferometer, eq.(2.97) with $\eta = 1$ and (2.104) gives relation as:

$$\langle x(\omega)^2 \rangle = \left(\frac{\lambda}{4\pi} \right)^2 \frac{2\hbar\Omega}{P} + \left(\frac{1}{m\omega^2} \right)^2 \frac{8\hbar\Omega P}{c^2} \geq \frac{4\hbar}{m\omega^2} \quad (2.117)$$

The equal sign holds when

$$P_{\text{opt}} = \frac{m\omega^2 \lambda c}{8\pi}. \quad (2.118)$$

The shot noise is inversely proportional to the laser power P as eq.(2.99) while the radiation pressure noise is proportional to P in eq.(2.110). This fact means that there is the optimal laser power P_{opt} . Equation (2.117) is consistent with eq.(2.115) except for a factor, assuming that the bandwidth is $1/\tau_0$ and $\omega\tau_0 \sim 1$. The equivalent GWs' amplitude is given as:

$$h_{\text{SQL}} = \frac{2}{\ell} \sqrt{\langle x(\omega)^2 \rangle} = \frac{4}{\ell\omega} \sqrt{\frac{\hbar}{m}}. \quad (2.119)$$

In the case of the Fabry-Perot interferometer,

$$\sqrt{h_{\text{shot}}^2 + h_{\text{rad}}^2} \geq \sqrt{2h_{\text{shot}}h_{\text{rad}}} = h_{\text{SQL}}. \quad (2.120)$$

Equations (2.99) and (2.110) give the following relation:

$$h_{\text{SQL}} = \frac{1}{\ell\omega} \sqrt{\frac{8\hbar}{m}} \quad (2.121)$$

instead of eq.(2.119).

2.6.4 Seismic noise

A typical spectrum of seismic noise is empirically given as:

$$x_{\text{seismic}} = 10^{-7} \left(\frac{1 \text{ Hz}}{f} \right)^2 \text{ m}/\sqrt{\text{Hz}}. \quad (2.122)$$

There are some places where seismic noise level is lower. For instance, seismic noise in Kamioka mine is smaller by two orders of magnitude than eq.(2.122). The equivalent sensitivity is given as:

$$h_{\text{seismic}} = \Gamma_v \left(\frac{2x_{\text{seismic}}}{\ell} \right), \quad (2.123)$$

assuming that the vibration isolation system can decrease seismic noise by Γ_v . If $\Gamma_v = 10^{-3}/f^{10}$ in Kamioka[4],

$$h_{\text{seismic}} = 6.67 \times 10^{-16} \left(\frac{3 \text{ km}}{\ell} \right) \left(\frac{1 \text{ Hz}}{f} \right)^{12} / \sqrt{\text{Hz}}. \quad (2.124)$$

2.6.5 Thermal noise

In the interferometric detectors, vibration of the mirrors and the fibers to suspend the mirrors is thermally excited by the coupling (this coupling corresponds to dissipation of the system) to heat bath.

A general theory of thermal noise

The Brownian motion of a harmonic oscillator in a heat bath with temperature T is represented as:

$$m \frac{d^2 x}{dt^2} + \gamma \frac{dx}{dt} + kx = f_N(t). \quad (2.125)$$

If f_N is white noise, the correlation function is given as:

$$\langle f_N(t) f_N(t') \rangle = 2\gamma k_B T \delta(t - t'), \quad (2.126)$$

using the Einstein relation. Using the relation that $\langle f_N(\omega)^2 \rangle = 4\gamma k_B T$, the power spectrum of the Brownian motion is represented as:

$$\langle x(\omega)^2 \rangle = \frac{4\gamma k_B T}{|-m\omega^2 + i\omega\gamma + k|^2}. \quad (2.127)$$

Taking the limit and using the relation that $\gamma = m\omega_0/Q$,

$$\langle x(\omega)^2 \rangle \sim \frac{4k_B T}{m\omega_0^3 Q} \quad (\omega \ll \omega_0) \quad (2.128)$$

$$\sim \frac{4\omega_0 k_B T}{m\omega^4 Q} \quad (\omega \gg \omega_0), \quad (2.129)$$

which is proportional to T/Q in both cases. Thus,

1. Decreasing the temperature
2. Increasing the mechanical quality factor Q of the oscillator

are effective to reduce the thermal noise.

This mechanical quality factor Q can be measured as follows. First, resonant vibration should be excited. Then, ring down time τ_r should be examined after the excitation force was removed. The decay of vibration at time t is proportional to

$$\exp \left[-\frac{\gamma t}{2m} \right] = \exp \left[-\frac{\omega_0 t}{2Q} \right], \quad (2.130)$$

namely, we obtain

$$Q = \frac{\omega_0 \tau_r}{2}. \quad (2.131)$$

Thermal oscillation of a harmonic oscillator with general dissipation

If the spring constant is complex $k \rightarrow k[1 + i\phi(\omega)]$, the equation of motion is

$$m \{ -\omega^2 + \omega_0^2 [1 + i\phi(\omega)] \} x(\omega) = f(\omega). \quad (2.132)$$

If

$$\phi(\omega) = \gamma\omega/k, \quad (2.133)$$

the situation is the same as in the previous discussion and $Q = 1/\phi(\omega_0)$. Even in the general case, where the fluctuation force is no longer white noise, fluctuation dissipation theorem holds:

$$\langle f_N(\omega)^2 \rangle = \frac{4m\omega_0^2 \phi(\omega) k_B T}{\omega} \quad (2.134)$$

and

$$\langle x(\omega)^2 \rangle = \frac{4k_B T}{\omega} \frac{\omega_0^2 \phi(\omega)}{m | -\omega^2 + \omega_0^2 [1 + i\phi(\omega)] |^2}. \quad (2.135)$$

Taking the limit of ω ,

$$\langle x(\omega)^2 \rangle \sim \frac{4k_B T}{\omega} \frac{\phi(\omega)}{m\omega_0^2} \quad (\omega \ll \omega_0) \quad (2.136)$$

$$\sim \frac{4k_B T}{\omega} \frac{\omega_0^2 \phi(\omega)}{m\omega^4} \quad (\omega \gg \omega_0). \quad (2.137)$$

Thermal noise of suspension

Because the restoring force of a pendulum is mainly gravity without loss, the dissipation is much smaller than the intrinsic dissipation (e.g. inner loss of wire). The restoring force of a pendulum made by a mass of M and a wire of length ℓ is given as:

$$F = -(Mg/\ell + k_{\text{el}}[1 + i\phi(\omega)])x \quad (2.138)$$

$$= -(Mg/\ell + k_{\text{el}})[1 + i\phi_{\text{p}}(\omega)]x, \quad (2.139)$$

where

$$\phi_{\text{p}} = \frac{k_{\text{el}}}{Mg/\ell + k_{\text{el}}} \phi \approx \frac{k_{\text{el}}\ell}{Mg} \phi. \quad (2.140)$$

Here, k_{el} is the spring constant due to the elasticity of the wire as:

$$k_{\text{el}} = \frac{\sqrt{TEI}}{2\ell^2}, \quad (2.141)$$

where $T = Mg$ is the tension of the wire, E is Young's modulus and I is the wire cross section's moment of inertia. Thus,

$$\phi_{\text{p}} \approx \frac{\phi}{2\ell} \sqrt{\frac{EI}{Mg}}, \quad (2.142)$$

where I is proportional to the square of the cross section and the cross section is proportional to the tension (Mg). If ϕ is independent of the tension, ϕ_{p} is proportional to $M^{1/2}$. Equation (2.135) shows that thermal noise (a root mean square) is proportional to $M^{-1/4}$.

Assuming that the resonant frequency is $f_{\text{p}} = 1$ Hz, eq.(2.137) can be calculated as:

$$\sqrt{\langle x(\omega)^2 \rangle} \sim 3.85 \times 10^{-22} \left(\frac{T}{20 \text{ K}} \right)^{1/2} \left(\frac{30 \text{ kg}}{M} \right)^{1/2} \left(\frac{f_{\text{p}}}{1 \text{ Hz}} \right) \left(\frac{\phi}{10^{-8}} \right)^{1/2} \left(\frac{100 \text{ Hz}}{f} \right)^{5/2} \text{ m}/\sqrt{\text{Hz}}. \quad (2.143)$$

The equivalent GWs' amplitude is

$$h_{\text{sus}} = \frac{2}{\ell} \sqrt{\langle x(\omega)^2 \rangle}. \quad (2.144)$$

Thermal noise of a mirror

The Brownian noise of the mirror substrate and its coating is given as[6]:

$$h_{\text{mirror}} = \frac{2}{\ell} \sqrt{\frac{4k_B T(1 - \sigma^2)}{\pi^{3/2} f E w_0}} \phi_{\text{sub}} \left[1 + \frac{2}{\sqrt{\pi}} \frac{1 - 2\sigma}{1 - \sigma} \frac{\phi_{\text{coat}}}{\phi_{\text{sub}}} \frac{d_{\text{coat}}}{w_0} \right], \quad (2.145)$$

where E , σ , ϕ_{sub} are Young's modulus, Poisson's ratio, mechanical loss of the mirror substrate, d_{coat} , ϕ_{coat} are thickness, mechanical loss of the mirror coating, and w_0 is radius of the laser beam.

One of the other noise sources is thermoelastic damping, which is caused by heat flows between compressed (heated) and stretched (cooled) area when mirror has elastic vibration[7, 8]. Thermoelastic noise of the mirror is given as[8]:

$$h_{\text{mirror thermo}} = \frac{2}{\ell} \sqrt{\frac{8\alpha^2(1+\sigma)^2 k_B T^2 w_0}{\sqrt{\pi} \kappa}} J(\Omega), \quad (2.146)$$

where

$$J(\Omega) = \frac{\sqrt{2}}{\pi^{3/2}} \int_0^\infty du \int_{-\infty}^\infty dv \frac{u^3 e^{-u^2/2}}{(u^2 + v^2)[(u^2 + v^2)^2 + \Omega^2]} \quad (2.147)$$

$$\Omega = \frac{\omega}{\omega_c} \quad (2.148)$$

$$\omega_c = \frac{2\kappa}{\rho C w_0^2}. \quad (2.149)$$

Here, α , κ , ρ and C are thermal expansion coefficient, thermal conductivity, density and specific heat of the mirror substrate, respectively.

For room temperature sapphire mirrors, conditions that $\Omega \gg 1$ and that $J(\Omega) \simeq 1/\Omega^2$ hold. Then,

$$h_{\text{mirror thermo}} = \frac{2}{\ell} \sqrt{\frac{32\alpha^2(1+\sigma)^2 k_B T^2 \kappa}{\sqrt{\pi}(\omega \rho C)^2 w_0^3}}. \quad (2.150)$$

2.7 Advantages of cryogenic mirrors

The idea of using sapphire cryogenic mirrors was originally proposed in Ref.[9]. There are three main advantages of the cryogenic sapphire mirrors. The first is reduction of thermal noise. While this thermoelastic noise is approximately constant between 300 K and 50 K, it steeply decreases below around 50 K. The thermoelastic noise finally becomes lower than other thermal noise sources, becoming dominated by the Brownian noise in the coating, at around 20 K[10, 11]. Therefore, design temperature of the KAGRA mirrors is 20 K. Here, examples of noise spectrum of sapphire mirrors at 300 K and 20 K are shown in Figures 2.7 and 2.8, respectively. h_{shot} , h_{rad} , h_{SQL} , h_{seismic} , h_{sus} , h_{mirror} , and h_{thermo} in the case of a Fabry-Perot interferometer, namely eqs.(2.99), (2.110), (2.121), (2.124), (2.144), (2.145), and (2.146) are

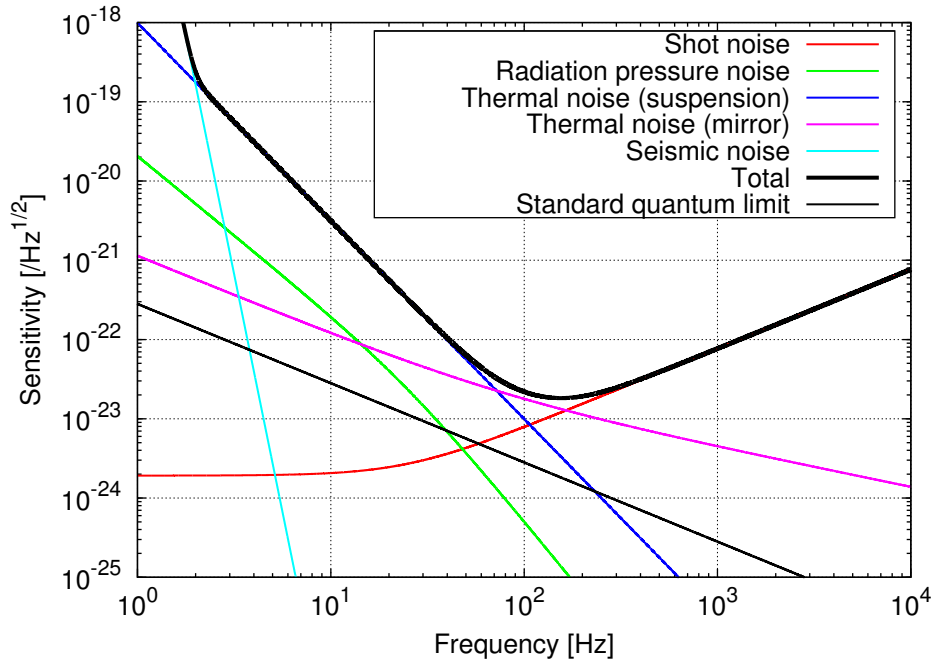


Figure 2.7: Example of noise spectrum of an interferometer (sapphire mirrors at 300 K).

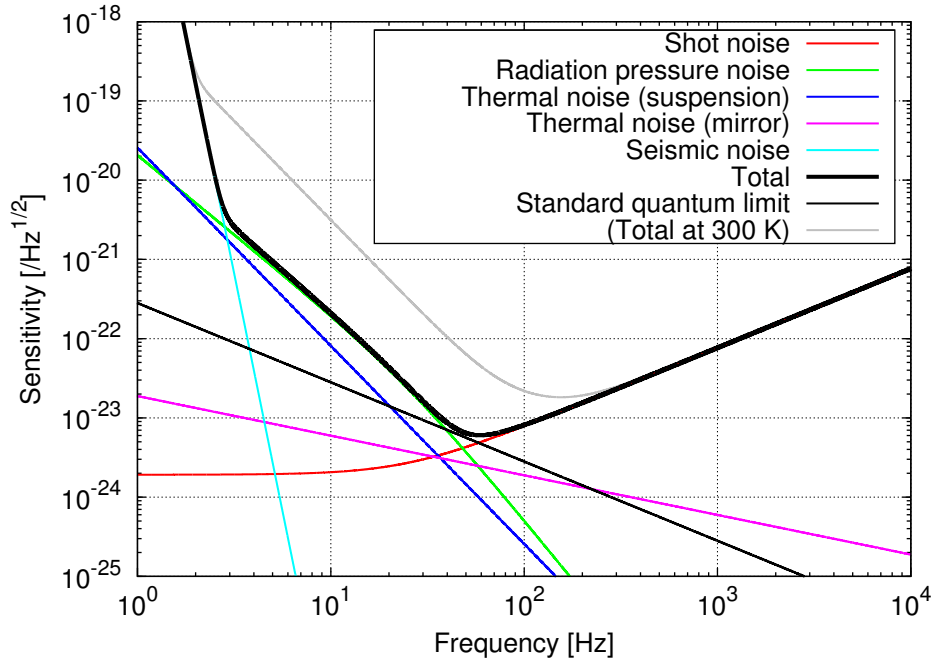


Figure 2.8: Example of noise spectrum of an interferometer (sapphire mirrors at 20 K).

plotted, where

$$\lambda = 1064 \text{ nm}, \quad \ell = 3 \text{ km}, \quad P = 200 \text{ W}, \quad M = 30 \text{ kg}, \quad \mathcal{F} = 1000, \\ \rho = 4000 \text{ kg/m}^3, \quad E = 400 \text{ GPa}, \quad \sigma = 0.27, \quad d_{\text{coat}} = 5 \text{ }\mu\text{m}, \quad w = 0.035 \text{ m}. \quad (2.151)$$

Values of ϕ_{sub} were taken from Ref.[12]. A value of $\phi_{\text{coat}} = 6 \times 10^{-4}$ (independent of temperature) was taken from Ref.[13, 14]. Material values of sapphire, such as specific heat, thermal expansion coefficient, and thermal conductivity, were from Ref.[15, 16]. At 300 K, the suspension thermal noise and the mirror thermal noise are dominant from several Hz to several hundred Hz. However, the cryogenic mirrors will make this thermal noise negligible level compared to noise intrinsic in the laser light (the shot noise and the radiation pressure noise).

The second advantage of the cryogenic mirrors is that they have less thermal lensing. When the mirror absorbs the laser, it will have a temperature gradient. Since refractive index depends on temperature, the refractive index is not uniform over whole of the mirror. It will distort the optical wavefronts of a laser beam. This is an effect called thermal lensing. This effect in the cryogenic interferometer is negligible mainly due to the higher thermal conductivity and lower dependence of the refractive index on temperature at 20 K[17]. The third advantage is the reduction of parametric instability. Parametric instability is an undesirable resonance of the transversal optical mode in interferometer cavities caused by the laser beam being modulated by elastic vibration of the mirrors. When the resonance happens, the transversal optical mode and the mirror elastic vibration will excite each other, and then, the resonance will grow up. This effect is also suppressed by using the cryogenic sapphire mirrors mainly because of the smaller diameter of the laser beam and the higher Young's modulus of sapphire[18].

2.8 Interferometric gravitational wave detectors in the world

The first generation of interferometric gravitational wave detectors, such as LIGO[19] in USA, VIRGO[20] in Italy, GEO[21] in Germany, and TAMA[22] in Japan, have already been in operation, and several second-generation detectors are currently under construction, such as AdLIGO, AdVIRGO, and KAGRA[23] (the Large-scale Cryogenic Gravitational wave Telescope (LCGT), a km-scale cryogenic detector project in Japan). Construction of KAGRA has started since 2010, and observation will start by the end of 2017. KAGRA aims to detect the gravitational waves from coalescence of binary neutron stars more than once per year. Third-generation gravitational wave detectors, such as ET (the Einstein Telescope)[24] in Europe, are also being planned. KAGRA and ET will enjoy two key advantages over other detectors: they will be constructed in an underground site with small seismic motion, and they will be equipped with the cooled mirror.

Cooling technique

This chapter describes principle of cooling the mirror of the interferometric gravitational wave detectors, a cooling system of KAGRA[25], and a problem of the cooling system.

3.1 Cooling mirrors of the interferometric gravitational wave detectors

Goal of cooling mirrors of the interferometric gravitational wave detectors is to extract heat from suspended mirrors without an external connection in vacuum. Such a connection usually causes noise by introducing mechanical vibration. There are several candidate methods to cool down the mirrors.

3.1.1 Heat switch

When the mirror is cooled down, a conductor of heat is attached to the mirror. Heat can be extracted from the mirror through the conductor. When the detector is operating, the conductor is detached not to introduce vibration.

In principle, cooling performance of the heat switch is determined by thermal conductivity of the conductor. However, thermal contact resistance between the contact parts is difficult to handle. Although it typically depends on the applied force to touch the conductor, large force on the conductor causes it to adhere to the mirror, especially if the conductor is soft pure metal with high thermal conductivity. Another problem is that heat switch needs a mechanical structure to attach and detach to the mirror. This structure tends to cause trouble and sacrifice a high stability required for a large-scale detector. It can also produce mechanical vibration due to the conductor's mechanical resonance, which can vibrate the mirror through another cooling path even if the conductor is detached from the mirror.

3.1.2 Gas cooling

Heat is extracted from the mirror by gas exchange. The mirror is surrounded by a cold box and the exchange gas extracts heat from the mirror to the cold box. This is a kind of the heat switch because the exchange gas is introduced during cooling phase, and pumped out during observation phase.

In the case of the interferometric gravitational wave detectors, holes on the box is necessary for the laser beam and for vibration isolation system. Thus, this method also needs some mechanical device to open and close the holes. Another problem with this method is that evacuation speed of turbo-molecular pumps for helium gas, often used for this purpose, is slow.

3.1.3 Optical cooling

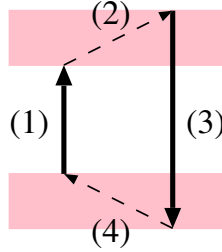


Figure 3.1: Schematic diagram of optical cooling.

A solid composed of Yb^{3+} with two groups of energy levels can be cooled down by laser as shown in Figure 3.1[26]. (1)It is excited by laser with energy $h\nu$ (h : the Planck constant, ν : frequency). (2)It absorbs energy from the heat bath. (3)It emits light with energy $h\nu_f$ ($\nu < \nu_f$). (4)It absorbs energy from the heat bath again. The minimum temperature achieved by this method currently is around 100 K[27].

3.1.4 Increasing radiation

Radiation is enhanced by increasing emissivity of the mass to be cooled. This method is not efficient means of heat transfer especially in low temperature T since transferred heat is limited by black body radiation, which is proportional to T^4 , as described in Section 4.1.

However, it requires no apparatus and has a high stability appropriate for large-scale detectors. Thus, thermal radiation is adopted as a method to cooling the mirror in KAGRA. Since thermal radiation is even less effective at lower temperature (than ~ 150 K), thermal conduction will also be used. For the conductor, long and thin wires or fibers are used in order

to minimize vibration introduced to the mirror. A main topic of this thesis is how to speed up this thermal radiation to decrease the cooling time of the mirror.

Near-field radiation

An experiment has shown that radiation between a small gap ($\sim \mu\text{m}$) exceeds the black body radiation due to photon tunneling[28]. In this case, force applied to the mirror by molecular collisions between the gap is problematic[29].

3.2 CLIO, a prototype of KAGRA

A KAGRA prototype called CLIO (Cryogenic Laser Interferometer Observatory)[30] is above the KAGRA location in the Kamioka Mine in Japan. CLIO has two 100 m arms, each of which includes a Fabry-Perot cavity. Each of these cavities is formed from two sapphire mirrors, each of which weighs 2 kg; the mirrors are cooled down to 20 K. The most important milestones that have been achieved at CLIO to date are the measurement of the thermal noise of the suspension[31] and the experimental demonstration of the thermal noise reduction by cooling[32].

An important lesson was learned from CLIO. In CLIO, thermal radiation through the duct shield (details are described in Chapter 5) was 1000 times larger than our expectation because reflections from the duct shield had been neglected[33]. To reduce this heat load, donut-shaped structures (called baffles) were introduced[34]. In KAGRA, I designed the duct shields on the basis of a detailed calculation from the manufacture stage onward.

3.3 KAGRA

KAGRA project will construct a 3 km arm length Fabry-Perot Michelson interferometer. KAGRA aims to detect gravitational waves from coalescence of binary neutron stars more than once per year. For this purpose, KAGRA is intended to achieve a sensitivity that is several orders of magnitude better than that of CLIO by using a longer arm length, larger mirrors (each mass is 23 kg), a larger seismic attenuation system, and higher laser power. Because of the heavier suspension, one of the issues is that the needed cooling time will be longer, which is the main topic of this thesis. Because of the higher laser power (KAGRA: 800 W, CLIO: 0.5 W, where both powers are at the interferometer beam splitter), heat will be absorbed by each mirror at a rate of 1 W in KAGRA while the corresponding value is on the order of 100 mW in CLIO. In addition, the heat load on the radiation shield from scattered light by the mirrors in KAGRA is expected to be larger than that of CLIO. For these reasons, the KAGRA cryogenic system is required to achieve better cooling performance than that of CLIO while

maintaining the same vibration isolation level. To achieve this performance, there are two independent cooling paths for the heat absorbed by the mirror and the heat from scattered light in KAGRA, as described in Subsection 3.3.

Figure 3.2 shows a schematic diagram of the KAGRA suspension system. Figure 3.3 shows a picture of the payload. Figure 3.4 shows photographs of one of the KAGRA cryostats and one of the cryocooler units. The four main mirrors of the Fabry-Perot cavities will be cooled down to 20 K in order to reduce thermal noise. The mirror will be suspended because it has to be a free test mass and has thus to be isolated from seismic vibration. The mirror will be suspended at the lowest part of the suspension system, which is made of multi-stage pendulums[36]. The mirror and the lower part of the suspension system (payload) will be cooled down. Each cryostat will cool down the payload in its double radiation shields. The inner shield, the size of which is limited by the maximum transportation size on Japanese public roads, is designed to be as large as possible to allow humans to work inside the shield. Four cryocooler units, which include double-stage cryocoolers (RP-082B PT made by Sumitomo Heavy Industries, cooling power 0.9 W at 4 K) inside, will be connected to each cryostat. The purpose of these units is to extract heat and simultaneously to isolate vibration of the cryocoolers[37, 38]. The first stages of the four cryocoolers cool the outer shield. The second stages of two of the cryocoolers cool the inner shield. The second stages of the other two cryocoolers cool the payload.

3.4 A problem of the KAGRA cooling system

3.4.1 Formularization of water adsorption

In KAGRA, water molecules will come from the 3 km duct through the duct shield onto the mirror. These molecules adsorbed by the mirror will decrease the mirror reflectivity, the finesse of the cavity, and then the sensitivity to the gravitational waves[39]. This subsection formularizes the water molecule adsorption to the mirror.

In the Maxwell-Boltzmann distribution, the number of molecules with a velocity between (v_x, v_y, v_z) and $(v_x + dv_x, v_y + dv_y, v_z + dv_z)$ is

$$f(v_x, v_y, v_z)d^3v = N \left(\frac{m}{2\pi k_B T} \right)^{\frac{3}{2}} \exp \left(-\frac{mv^2}{2k_B T} \right) d^3v, \quad (3.1)$$

where N is the total number of the molecules included in the whole volume V , m is mass of one molecule, k_B is the Boltzmann constant and T is temperature. The number of the molecules

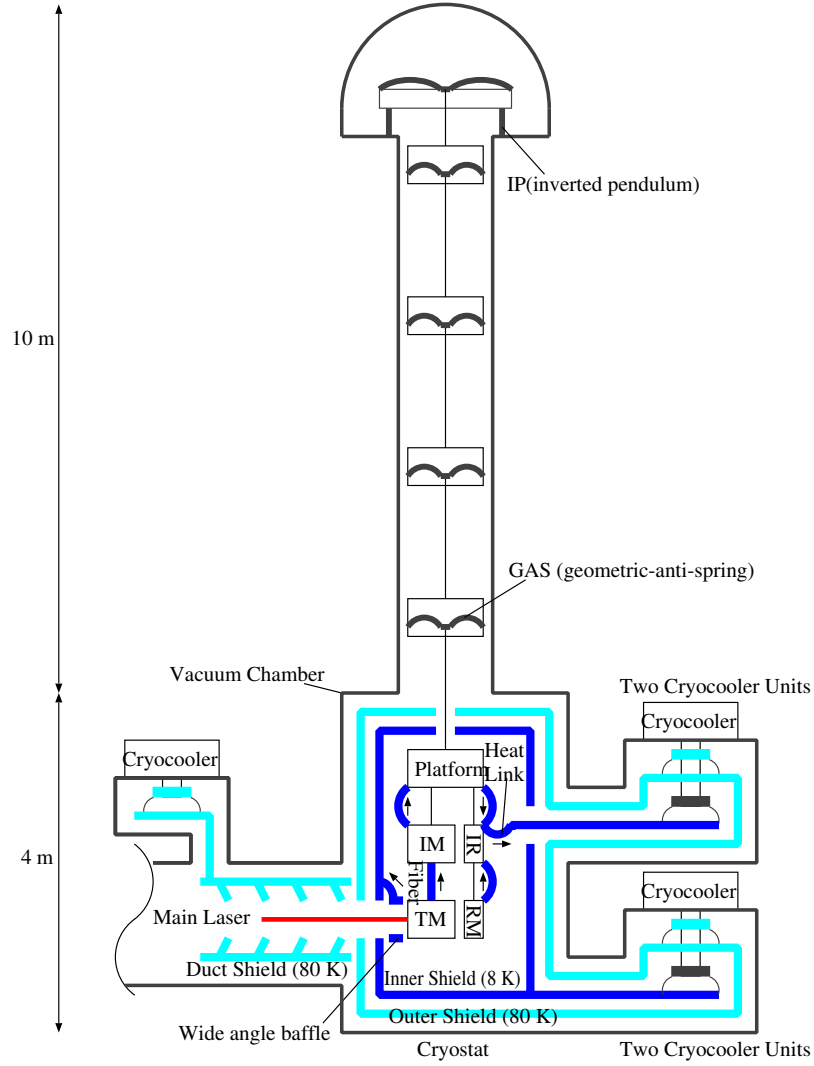


Figure 3.2: Schematic diagram of KAGRA's suspension system. The mirror represented by TM is suspended from a seismic attenuation system (SAS), which consists of seven stages of pendulum. Cryogenic payload, which consist of TM: test mass (mirror), RM: recoil mass, IM: intermediate mass, IR: intermediate recoil mass, and platform, are cooled down. They are surrounded by double (inner and outer) radiation shields. The mirror made of sapphire is suspended by sapphire fibers from IM. The arrows show the direction of heat flow. Heat from the mirror is extracted to IM through the fibers, transferred to platform, IR and to the cryocoolers by thin metal wires called heat links. Duct shields are installed to reduce thermal radiation through a hole in the shields.

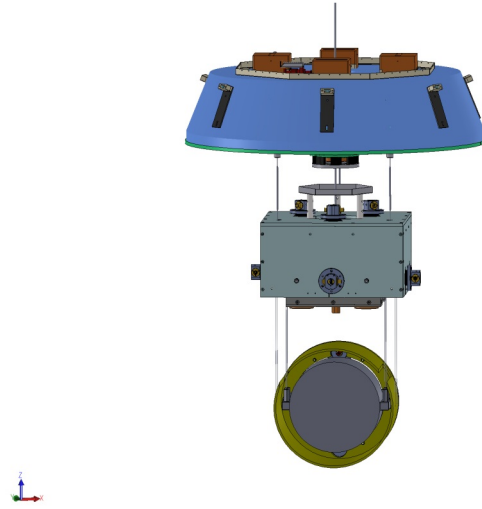


Figure 3.3: Picture of the KAGRA cryogenic payload, taken from Ref.[35]. The diameter of the mirror is 220 mm.

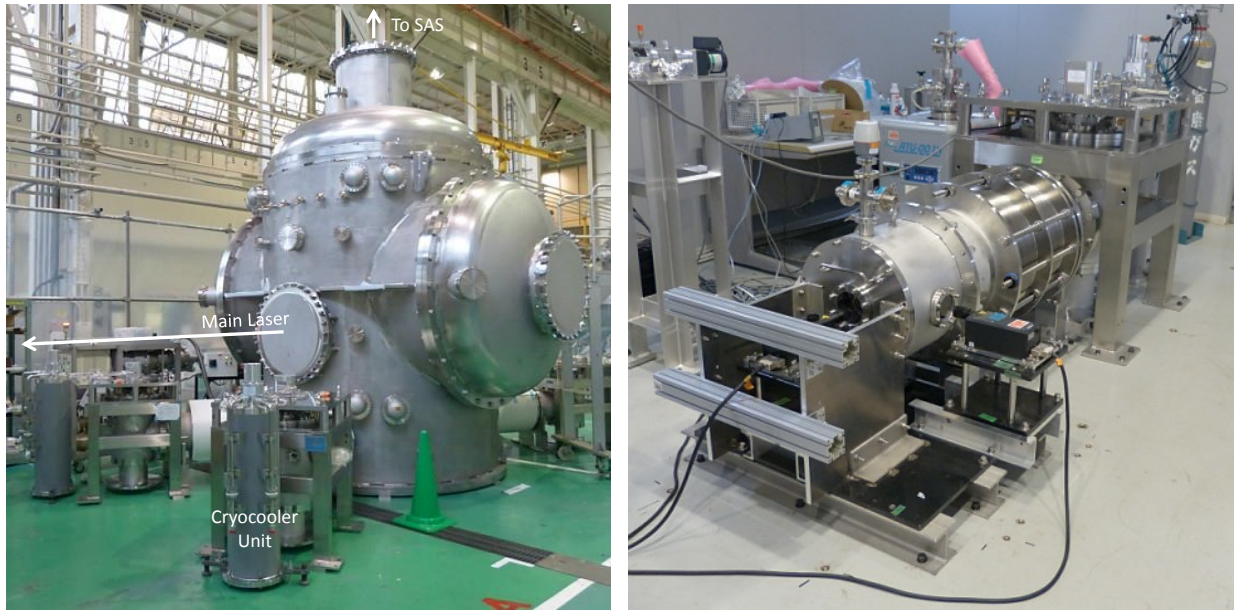
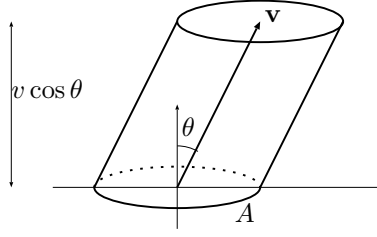


Figure 3.4: Photographs of a KAGRA cryostat (left) and one of the cryocooler units (right)[25].

Figure 3.5: Calculation of the number of the molecules which hit an area A during time Δt .

which hit an area A during time Δt is, considering a box shown in Figure 3.5,

$$N_{\text{hit}} = \int \frac{Av \cos \theta \Delta t}{V} \cdot f \cdot 2\pi v^2 dv \sin \theta d\theta \quad (3.2)$$

$$= \frac{NA\Delta t}{V} \int v \left(\frac{m}{2\pi k_B T} \right)^{\frac{3}{2}} \exp \left(-\frac{mv^2}{2k_B T} \right) 4\pi v^2 dv \cdot \frac{1}{2} \int_0^{\pi/2} \cos \theta \sin \theta d\theta \quad (3.3)$$

$$= \frac{NA\Delta t}{V} \frac{1}{4} \bar{v}, \quad (3.4)$$

where \bar{v} is the averaged velocity of the molecules:

$$\bar{v} = \sqrt{\frac{8k_B T}{\pi m}}. \quad (3.5)$$

Using the equation of state of ideal gas $pV = Nk_B T$ (p : pressure),

$$\frac{N_{\text{hit}}}{A\Delta t} = \frac{p}{\sqrt{2\pi m k_B T}}. \quad (3.6)$$

A viewing solid angle through a duct shield (aperture diameter d , length h , view angle $\tan \theta_d = d/(2h)$) divided by the whole solid angle 4π is:

$$\frac{1}{2} (1 - \cos \theta_d) \simeq \frac{1}{4} \theta_d^2 = \left(\frac{d}{4h} \right)^2. \quad (3.7)$$

Multiplying eq.(3.6) by eq.(3.7) yields the number of the molecules through the duct shield:

$$\left(\frac{d}{4h} \right)^2 \frac{p}{\sqrt{2\pi m k_B T}}. \quad (3.8)$$

From this equation, time T_{water} which is necessary to form one layer of water molecules can be calculated[39]. Using a typical scale of a water molecule $l_{\text{water}} = 1 \text{ \AA}$,

$$T_{\text{water}} \sim \left[\left(\frac{d}{4h} \right)^2 \frac{p}{\sqrt{2\pi m k_B T}} l_{\text{water}}^2 \right]^{-1}. \quad (3.9)$$

Parameters for KAGRA ($p = 2 \times 10^{-7}$ Pa[45], $T = 300$ K, $d = 0.313$ m, $h = 6.3$ m) yield:

$$T_{\text{water}} \sim 300 \text{ days.} \quad (3.10)$$

The surface roughness of the mirrors with one layer of water molecules is expected to be l_{water} multiplied by a factor 2 or 3 due to random position of the molecules. This is comparable to the surface roughness of KAGRA mirror without water molecules, 0.5 nm[40]. Thus, to recover the mirror from the adsorption, it is necessary to heat up the mirror to room temperature, and then, to cool down again once per 300 days.

3.4.2 Dead time due to heating up and cooling down

An operation stop of KAGRA due to heating and cooling is expected to reach several months (it will take two months without any trick to cool down the cryostat as later shown in Figure 4.9). This stop will happen once per year as shown in eq.(3.10). In the other words, cooling and heating will occupy 20 % of the available time. This dead time is one of the most important problems of KAGRA. This is why the topic of this thesis is to reduce the dead time by reducing the cooling time with effective thermal radiation.

Cooling time reduction

This chapter describes calculation of thermal radiation, candidates of high-emissivity coatings, calculation of cooling time with and without the coating, a small-scale experiment and an experiment in the actual KAGRA cryostat[41].

4.1 Theory of thermal radiation

4.1.1 Thermal radiation

Infinitesimal heat, dQ , which is radiated per unit time from an infinitesimal surface area of a body, dA , to an infinitesimal area in the (θ, ϕ) direction on a unit sphere, dA' , is proportional to dA and $dA' \cos \theta$:

$$dQ = I(\theta, \phi) dA dA' \cos \theta. \quad (4.1)$$

Here, the intensity of radiation, $I(\theta, \phi)$, generally includes radiation with various wavelengths. Assuming that $I_\lambda(\lambda, \theta, \phi) d\lambda$ represents radiation within a wavelength range of $\lambda \sim \lambda + d\lambda$,

$$I(\theta, \phi) = \int_0^\infty I_\lambda(\lambda, \theta, \phi) d\lambda. \quad (4.2)$$

Using a relation that

$$dA' = \sin \theta d\theta d\phi, \quad (4.3)$$

eq.(4.1) is written as:

$$dQ = I(\theta, \phi) dA \sin \theta \cos \theta d\theta d\phi. \quad (4.4)$$

Thus, the total heat radiated from dA is given as:

$$Q = dA \int_0^\infty d\lambda \int_0^{2\pi} d\phi \int_0^{\frac{\pi}{2}} \sin \theta \cos \theta d\theta I_\lambda(\lambda, \theta, \phi). \quad (4.5)$$

Heat radiated per unit time and unit surface area, called emissive power, is obtained as:

$$E = \frac{Q}{dA} = \int_0^\infty d\lambda \int_0^{2\pi} d\phi \int_0^{\frac{\pi}{2}} \sin \theta \cos \theta d\theta I_\lambda(\lambda, \theta, \phi). \quad (4.6)$$

Using monochromatic emissive power, defined as:

$$E_\lambda = \int_0^{2\pi} d\phi \int_0^{\frac{\pi}{2}} \sin \theta \cos \theta d\theta I_\lambda(\lambda, \theta, \phi), \quad (4.7)$$

one can obtain

$$E = \int_0^\infty E_\lambda d\lambda. \quad (4.8)$$

If I_λ is independent of the direction of radiation, (θ, ϕ) , eq.(4.6) and eq.(4.7) become:

$$E = \int_0^\infty I_\lambda d\lambda \int_0^{2\pi} d\phi \int_0^{\frac{\pi}{2}} \sin \theta \cos \theta d\theta = \pi I, \quad (4.9)$$

$$E_\lambda = I_\lambda \int_0^{2\pi} d\phi \int_0^{\frac{\pi}{2}} \sin \theta \cos \theta d\theta = \pi I_\lambda. \quad (4.10)$$

4.1.2 Black body radiation

Definition of a black body

A black body is defined as follows:

1. It absorbs all radiation of any wavelength coming from any direction.
2. It emits the largest intensity of thermal radiation at the same temperature and wavelength among any surface.
3. The intensity of its radiation is independent of the direction of the radiation.

Planck's law

The energy density of electromagnetic waves from the black body within a frequency range from ν to $\nu + d\nu$ is given as:

$$D_\nu = \frac{8\pi h}{c^3} \frac{\nu^3}{e^{h\nu/k_B T} - 1} d\nu, \quad (4.11)$$

where h is Planck's constant, k_B is Boltzmann's constant, c is the speed of light and T is temperature. Using the wavelength λ ,

$$D_\nu = \frac{8\pi hc}{\lambda^5 (e^{hc/k_B \lambda T} - 1)} d\lambda. \quad (4.12)$$

The black body intensity per unit solid angle and unit wavelength, $I_{\lambda,b}$, is written as:

$$I_{\lambda,b} = \frac{c}{4\pi} D_\nu = \frac{2hc^2}{\lambda^5(e^{hc/k_B\lambda T} - 1)}. \quad (4.13)$$

Equation (4.10) gives the monochromatic emissive power of a black body,

$$E_{\lambda,b} = \pi I_{\lambda,b} = \frac{2\pi hc^2}{\lambda^5(e^{hc/k_B\lambda T} - 1)}, \quad (4.14)$$

which is called Planck's law.

Wien's displacement law

The wavelength where the monochromatic emissive power of a black body has the maximum value at temperature T , $\lambda_{\max}(T)$, is a solution of the following equation:

$$\frac{\partial E_{\lambda,b}}{\partial \lambda} = 0. \quad (4.15)$$

In eq.(4.14), this condition gives equation:

$$x = 5(1 - e^{-x}) \rightarrow x = 4.965, \quad (4.16)$$

where $x = hc/k_B\lambda T$. Namely,

$$\lambda_{\max}T = 2898 \mu\text{m K}. \quad (4.17)$$

This is called Wien's displacement law.

Stefan-Boltzmann law

Equations (4.8) and (4.14) give the Stefan-Boltzmann law:

$$E_b = \int_0^\infty E_{\lambda,b} d\lambda = \int_0^\infty \frac{2\pi hc^2}{\lambda^5(e^{hc/k_B\lambda T} - 1)} d\lambda = \sigma T^4, \quad (4.18)$$

where σ is the Stefan-Boltzmann constant.

4.1.3 Emissivity

Because of the definition of a black body, the emissive power and the monochromatic emissive power of an actual body are smaller than those of a black body. Then, the ratio to a black body,

$$\epsilon_\lambda = \frac{E_\lambda}{E_{\lambda,b}}, \quad (4.19)$$

is called monochromatic emissivity and

$$\epsilon = \frac{E}{E_b} \quad (4.20)$$

is called total emissivity or simply emissivity. Namely, the heat of radiation per unit time from an actual body (surface area S), Q is given as:

$$\frac{Q}{S} = \epsilon \sigma T^4. \quad (4.21)$$

In addition, a body that satisfies the following conditions is called a gray body:

- Its monochromatic emissivity ϵ_λ is a constant independent of the wavelength, $\epsilon_\lambda = \epsilon$.
- Its radiation intensity is independent of the direction of radiation.
- Its reflection of incident thermal radiation with any incident angle is isotropic.

4.1.4 Kirchhoff's law

Assuming that the reflectivity and absorptivity of a body for all wavelengths is r and α , respectively, the following equation holds:

$$r + \alpha = 1. \quad (4.22)$$

Next, this body (surface area S) is surrounded by a black body with temperature T , as shown in Figure 4.1. When the body and the black body are in thermal equilibrium, the temperature of the body is also T and radiates heat

$$\epsilon \sigma T^4 S. \quad (4.23)$$

On the other hand, α of the heat radiation from the black body is absorbed by the body and r returns to the black body. Thus, the body absorbs

$$\alpha \sigma T^4 S. \quad (4.24)$$

Due to thermal equilibrium, eq.(4.23) and eq.(4.24) have to be balanced as:

$$\epsilon = \alpha = 1 - r. \quad (4.25)$$

This discussion also holds for a certain wavelength λ , using reflectivity for wavelength λ , r_λ :

$$\epsilon_\lambda = 1 - r_\lambda. \quad (4.26)$$

Equation (4.26) is called Kirchhoff's law.

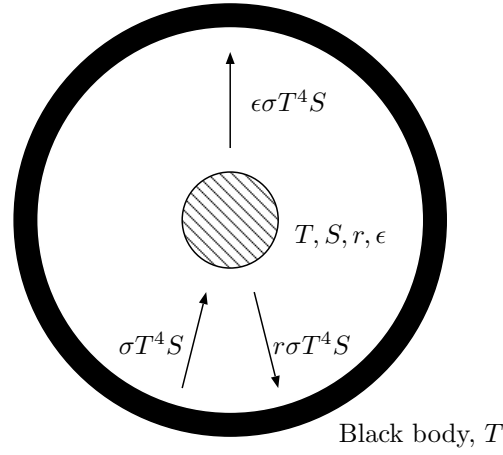


Figure 4.1: Derivation of Kirchhoff's law

4.1.5 Diffusive and specular surfaces

There are two limiting surfaces to calculate thermal radiation[42]. One surface reflects coming radiation to all the direction uniformly. The other surface reflects rays according to the reflection law. For an incident ray, the reflected ray is at the same angle away from the surface normal within the plane including the incident ray and the surface normal.

Calculation of radiation heat transfer strongly depends on whether the surfaces reflect rays of radiation diffusely or specularly. For example, radiation propagates differently through a pipe with diffusive and specular surfaces. Figure 4.2 shows that radiation is reflected more times by a diffusive pipe than by a specular pipe. In other words, radiation passes through the specular pipe with small number of reflections. Figure 4.3 shows calculated power of thermal radiation through a pipe with $L/d = 50$ (L , d are length and diameter of the pipe). The calculation method is the same as that used in Section 4.4. The reflectivity was assumed to be independent of the incident angle. As a result, power through the specular pipe is several orders of magnitude larger than that through the diffusive pipe depending on reflectivity of the pipe.

Experiment using a metal pipe supports the model of specular reflection of thermal radiation on the surface (experiments in Ref.[33, 34, 43, 44] and one conducted in Chapter 5). An experiment, described in Section 4.4, has clearly shown that black coating (DLC, a diamond-like carbon coating) used here is a specular surface.

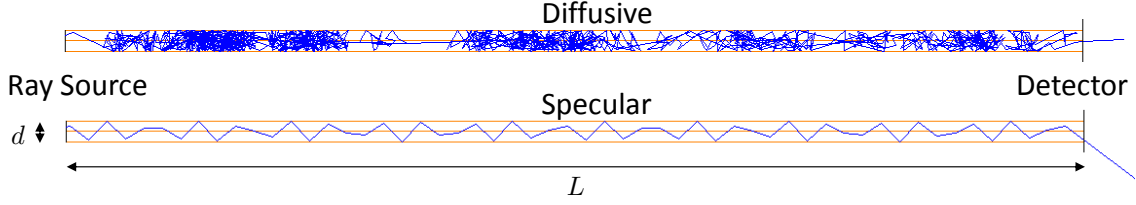


Figure 4.2: Examples of ray paths through pipes with diffusive and specular surfaces. Aspect ratio of the pipe is $L/d = 50$. (L , d is length and diameter of the pipe.) Rays go from ray sources to detectors. Radiation passes through a specular pipe with smaller number of reflections. More heat will be transferred through a specular pipe. Quantitative calculation of thermal radiation is shown in Figure 4.3.

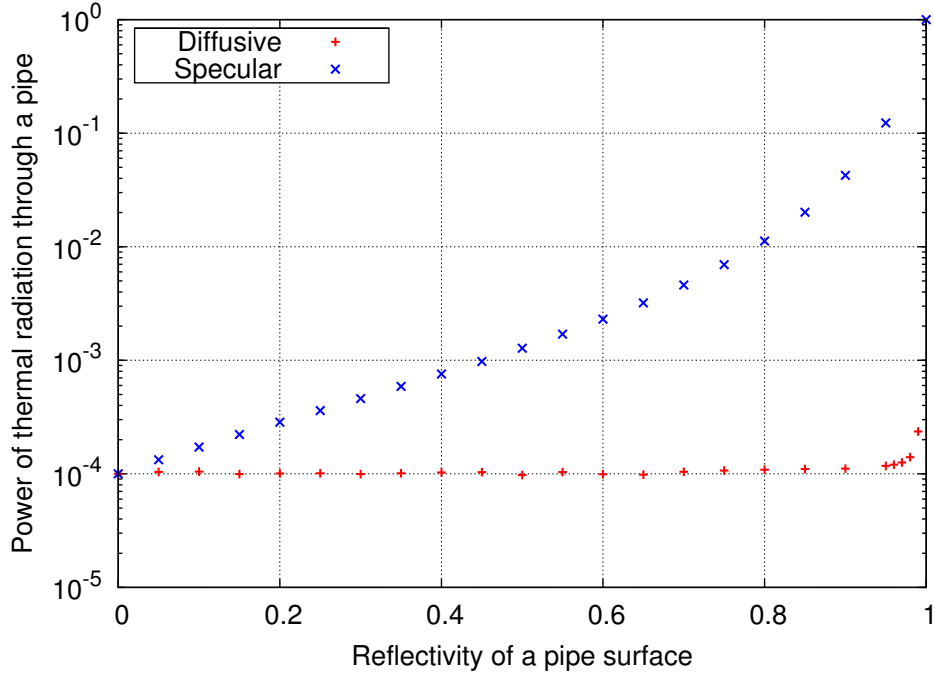


Figure 4.3: Calculated power of thermal radiation through the pipe with $L/d = 50$. The vertical axis represents ratio of radiation power passing through the pipe to radiation power emitted by the source. (The source emits radiation with power 1.) Calculation method is the same as that used in Section 4.4. Unless reflectivity of the pipe is extremely high, power through the diffusive pipe is reduced approximately by 10^{-4} , which is portion directly transferred from the source to the detector without reflected or scattered by the pipe. On the other hand, depending on the reflectivity, power through the specular pipe is several orders of magnitude larger than that through the diffusive pipe.

4.2 High-emissivity coating

There are many high-emissivity or black coatings. However, ultra-high vacuum (2×10^{-7} Pa in KAGRA[45]) is required in the interferometric gravitational wave detectors since scatter of laser by molecules causes noise. Thus, small outgassing rate from the coating is required. Here, two candidates of the black coatings are introduced from this point of view.

4.2.1 Diamond Like Carbon (DLC) coating

DLC is an intermediate material between diamond and graphite[46]. Diamond is crystal composed of carbon atoms connected with the sp^3 hybrid bonds. Graphite is composed of carbon atoms connected with the sp^2 hybrid bonds. DLC is a film composed of carbon and hydrogen atoms. The black color of the DLC coating may represent the fact that π bonds create energy levels over wide energy range, which absorbs light. Their structures are shown in Figure 4.4.

The outgassing rate was lower than stainless steel, which is main component of the vacuum chamber[47]. Smooth surface due to the amorphous structure of DLC absorbs little water molecules. Emissivity of DLC,

$$\epsilon = \epsilon_r \left(\frac{T}{300 \text{ K}} \right) \quad (4.27)$$

$$\epsilon_r = 0.3 \sim 0.4 \quad (4.28)$$

is obtained in the experiment described later. The value at 300 K is comparable to absorptivity 0.41 at $10 \mu\text{m}$ [43], where 300 K black body radiation has the largest intensity. Emissivity of DLC is not so high. However, from the viewpoint of outgassing rate, the DLC coating is the best candidate[48].

Another point is absorptivity for $1 \mu\text{m}$, wavelength of the main laser. This point is critical for the scattered light noise as described in Chapter 5. DLC was originally used for room temperature interferometric gravitational wave detectors as an absorber for scattered light of the main laser. Absorptivity of DLC at $1 \mu\text{m}$ is 0.65[48].

4.2.2 Solblack

Solblack is a commodity from Asahi Precision. Co. Ltd. Solblack is a chemically-treated nickel coating. Zigzag structures shown in Figure 4.5 seem to cause high absorptivity. Although the company is familiar with how to make the coating, detailed material properties of the coating is still unknown.

The outgassing rate was one or two orders of magnitude larger than that of stainless steel even if Solblack is baked under vacuum[49]. There is a measurement showing that emissivity

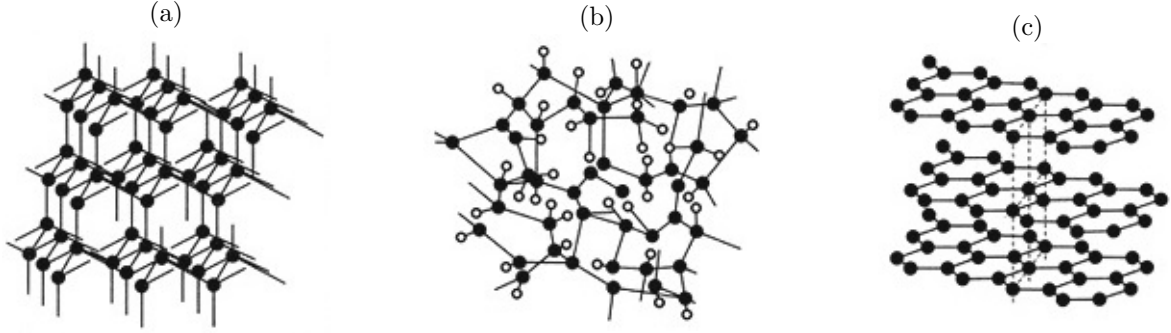


Figure 4.4: Structures of (a) diamond, (b) DLC (Diamond Like Carbon), (c) graphite. Black dots represent carbon atoms, and white dots represent hydrogen atoms. Figures are taken from Ref.[46].

of Solblack is[50]

$$\epsilon = 0.4 \times \left(\frac{T}{300 \text{ K}} \right). \quad (4.29)$$

Absorptivity at $1 \mu\text{m}$ is larger than 99%[51]. While DLC is better in terms of the vacuum compatibility, Solblack is better for absorption of the scattered light of the main laser.

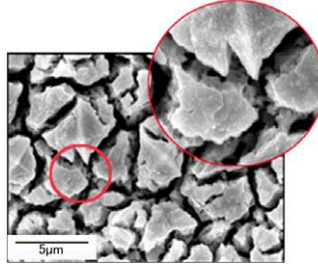


Figure 4.5: Photograph of Solblack taken by an electron microscope. This photograph is cited from [51].

4.3 Calculation of cooling time of KAGRA

This section describes a calculation model of the cooling time of KAGRA cooling system to show the effect of the high-emissivity coating. Measurement of the emissivity and experimental verification of this model are presented in Subsections 4.4 and 4.5.

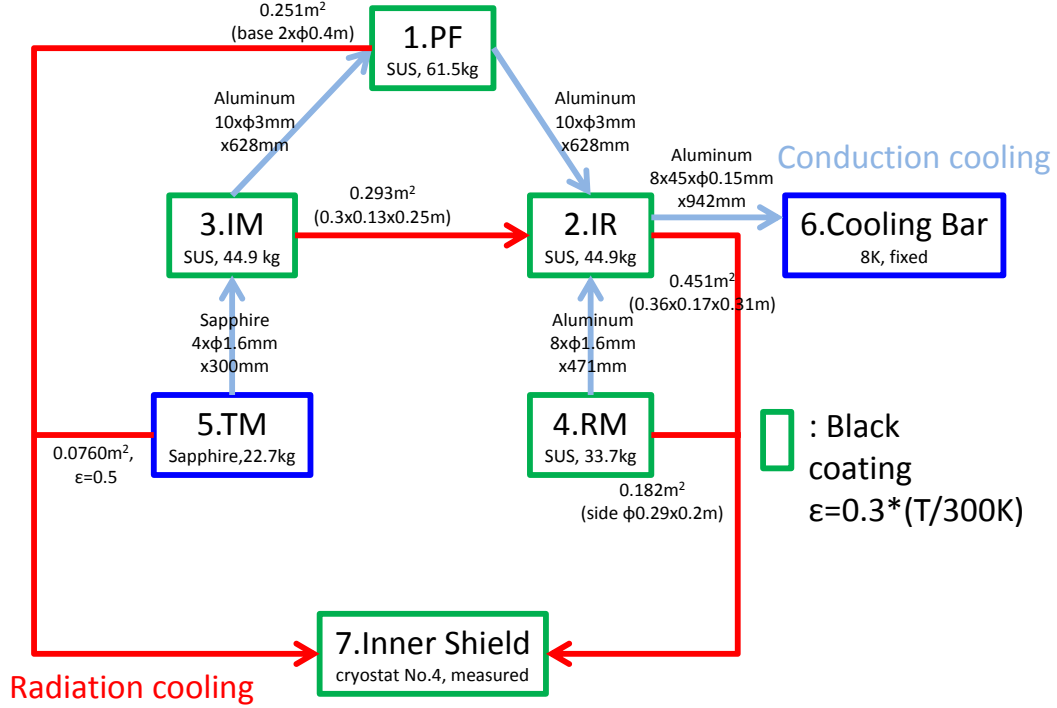


Figure 4.6: Schematic diagram of a calculation model of the KAGRA cryogenic system. Dimension, mass, and effective surface area of each mass are shown. $N \times \phi d \times \ell$ represents dimension of the wires or the fibers (N : number, d : diameter, ℓ : length).

4.3.1 Method

To calculate the cooling time, each mass of the cryogenic payload was modeled as a mass point as shown schematically in Figure 4.6. The point masses were thermally connected by thermal conduction and radiation. Since IM is surrounded by IR, thermal radiation from IM to IR is considered. Radiation from the other masses conducts heat to the inner shield. The heat links are connected to extract heat from the mirror to the cooling bar, which is connected to the cryocoolers. Parameters of the heat links, such as the number, thickness, and length, were determined considering the vibration isolation[52]. Parameters of each mass and the heat links and the sapphire fibers between the masses are also shown in Figure 4.6. The inner surface of the inner shield and all the masses except the test mass will be coated with the high-emissivity coating. In this calculation, temperature of the inner shield was taken from the measured value of the actual cryostat during a cooling test described in Subsection 4.5. Temperature of the

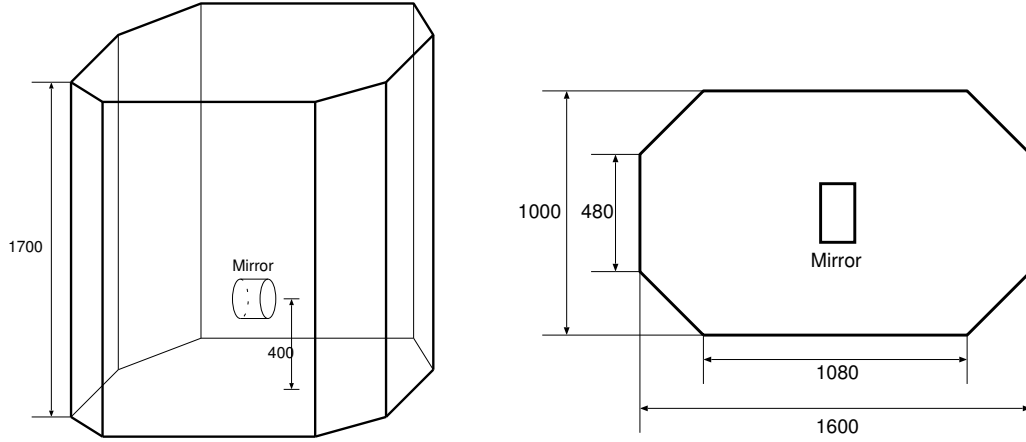


Figure 4.7: Schematic diagram of the inner shield of the KAGRA cryostat. The picture on the right-hand side is a top view of the inner shield (units: mm). The DLC coating approximately covered 50% of the surface area of the inner surface of the inner shield[41].

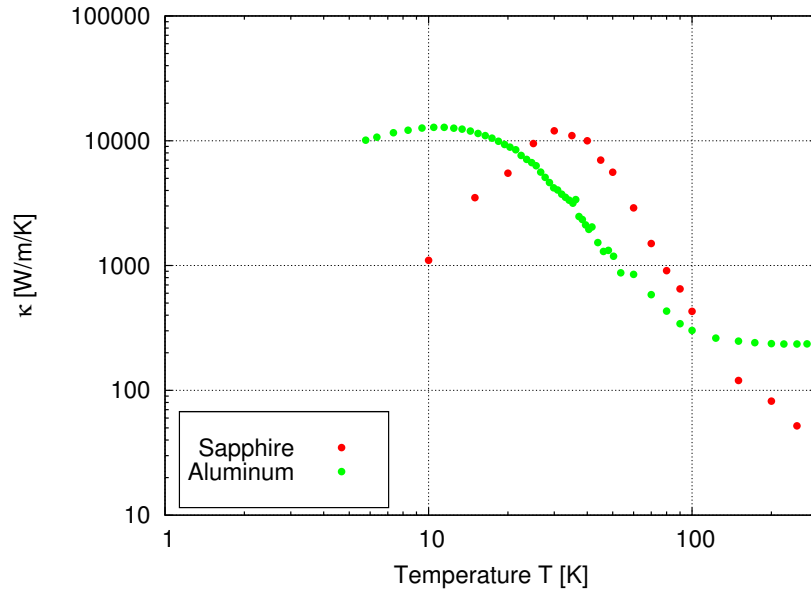


Figure 4.8: Thermal conductivity of a sapphire fiber with diameter 1.6 mm[54] and aluminum (below 60 K measured data shown in Figure A.6, above 60 K from Ref. [15]).

cooling bar was fixed at 8 K in this calculation. The equation solved here is:

$$\frac{dT_i}{dt} = -\frac{\sum_j Q_{ij}(T)}{M_i C_i(T_i)}, \quad (4.30)$$

where t is time, i is index for each mass, T_i is temperature, M_i is mass, and $C_i(T_i)$ is the specific heat at temperature T_i of mass i . Q_{ij} is heat transferred from mass i to mass j , including thermal radiation (described by eqs.(4.31), (4.32)) and thermal conduction (described by eq.(4.33)). The heat radiated by the mass i to the inner shield (temperature T_{sh}) is:

$$Q_{i,\text{sh}}(T_i, T_{\text{sh}}) = \epsilon_i A_i \sigma (T_i^4 - T_{\text{sh}}^4), \quad (4.31)$$

where σ is the Stefan-Boltzmann constant, ϵ_i and A_i are the emissivity and the effective surface area of mass i , respectively. Radiation from IM to IR is:

$$Q_{\text{IM,IR}}(T_{\text{IM}}, T_{\text{IR}}) = \frac{A_{\text{IM}} \sigma (T_{\text{IM}}^4 - T_{\text{IR}}^4)}{1/\epsilon_{\text{IM}} + 1/\epsilon_{\text{IR}} - 1}. \quad (4.32)$$

Derivation of eqs.(4.31), (4.32) is given in eqs.(4.39), (4.40). The effective surface area represents the surface area which contributes to thermal radiation. Namely, surfaces hidden by another mass are excluded. Since the surface area of the inner shield is, as shown in Figure 4.7, sufficiently large compared to that of the payload, the heat transfer is independent of the emissivity of the inner shield. On the other hand, the heat conducted by N fibers with temperatures T_i, T_j at the ends, a cross-section of S , a length of ℓ , and a thermal conductivity of $\kappa(T)$ is:

$$Q_{ij}(T_i, T_j) = -\frac{NS}{\ell} \int_{T_i}^{T_j} \kappa(T') dT'. \quad (4.33)$$

It is important to note that the thermal conductivity of the sapphire fibers is proportional to their diameter[53]. Here, the measured value of a monolithic sapphire fiber with diameter 1.6 mm in Ref.[54] was used. Since thermal conductivity of aluminum below ~ 70 K strongly depends on its purity or diameter[55], measured thermal conductivity of aluminum wire (5N: 99.999 % purity, 0.15 mm in diameter, made by Tanaka-kikinzoku) was used in this temperature region (the detail of the measurement is described in Appendix A). The other material values such as the thermal conductivity of the aluminum fibers above 70 K and the specific heat of stainless steel or sapphire were taken from the literature (e.g, [15, 16, 56]). Figure 4.8 shows thermal conductivity of aluminum and sapphire used for this calculation. The emissivity of the high-emissivity coating and that of sapphire are assumed as:

$$\epsilon_{\text{DLC}} = 0.3 \times \left(\frac{T}{300 \text{ K}} \right) \quad (4.34)$$

$$\epsilon_{\text{sap}} = 0.5. \quad (4.35)$$

These are obtained values in the following experiments. The emissivity without any coating was assumed to be 0.03, a typical value of metal surface (e.g. [57]).

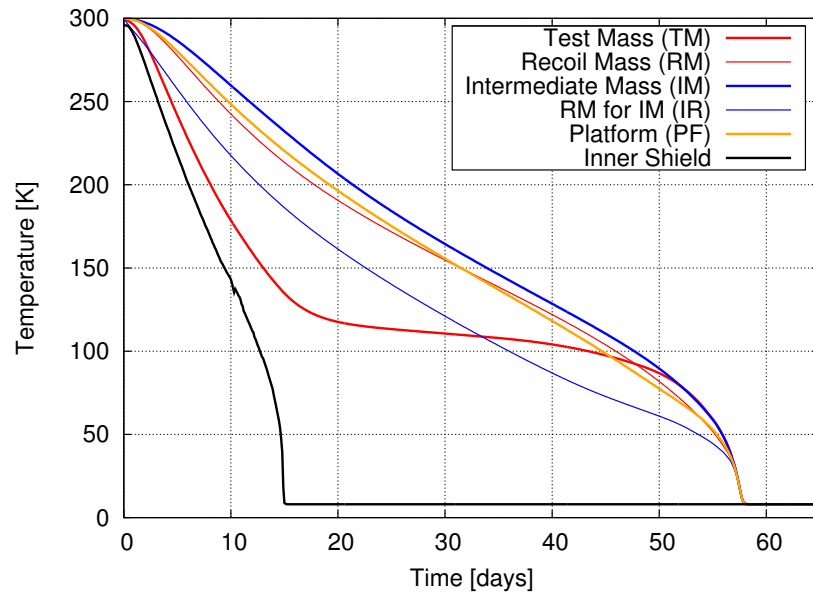


Figure 4.9: Calculation results of cooling time of the KAGRA payload without any coating.

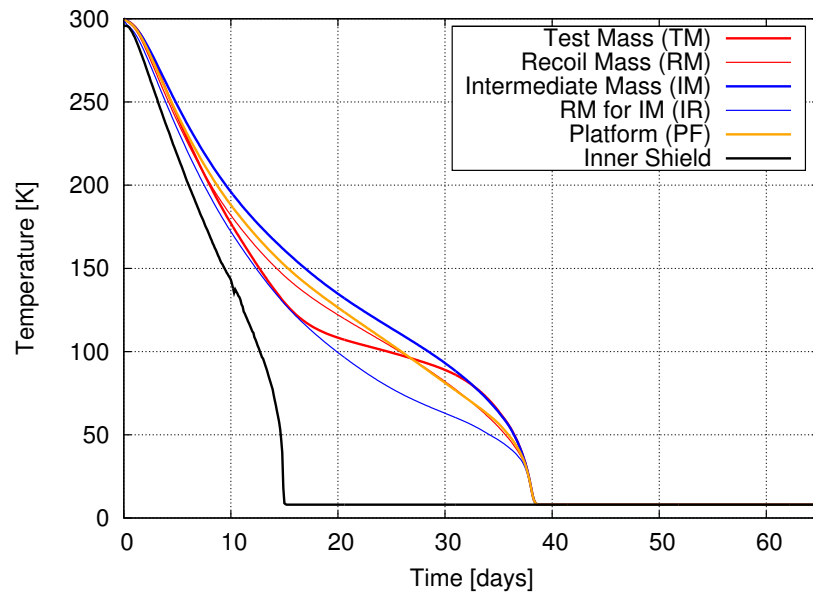


Figure 4.10: Calculation results of cooling time of the KAGRA payload with the high-emissivity coating.

4.3.2 Results

The calculation results are shown in Figures 4.9 and 4.10. Approximately above 150 K, the payload is cooled mainly by thermal radiation. Below that temperature, the conduction cooling is dominant. The high-emissivity coating can reduce the cooling time when the radiation cooling is dominant. The calculation predicts that the high-emissivity coating can reduce the cooling time from 58 days to 39 days.

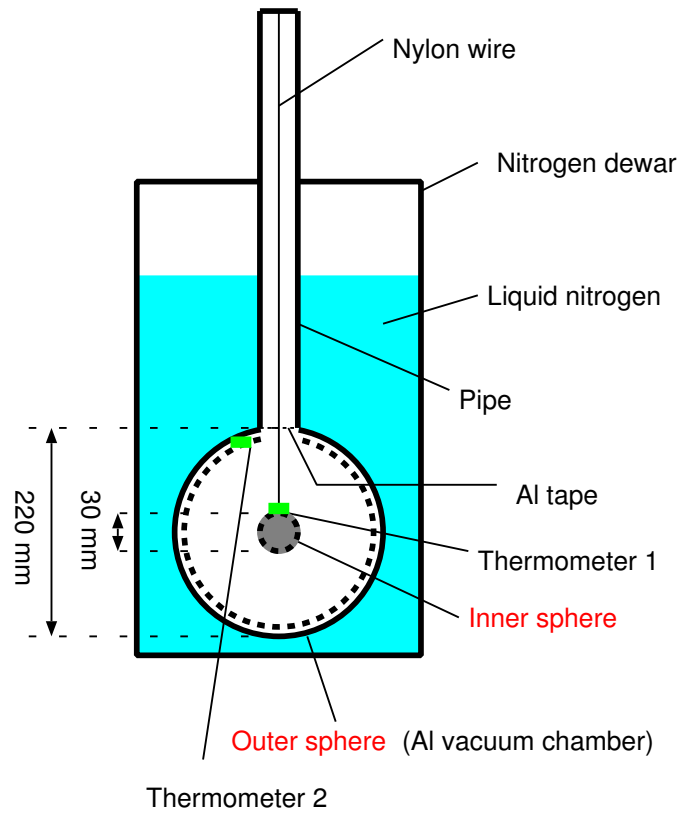


Figure 4.11: Experimental setup. In the outer sphere (vacuum chamber), the inner sphere is suspended by a nylon wire. Its thermal conduction is negligible. Thick dotted lines represent a diamond-like carbon (DLC) coating. Heat transfer by radiation was examined.

4.4 Small-scale experiment

4.4.1 Purpose

This experiment was conducted to verify calculation models to calculate thermal radiation (diffusive or specular surface) and to evaluate the emissivity of the DLC coating.

4.4.2 Method

An experimental setup is shown in Figure 4.11. In the outer sphere (220 mm in diameter, made of aluminum A1070), the inner sphere made of oxygen-free copper with 30 mm in diameter

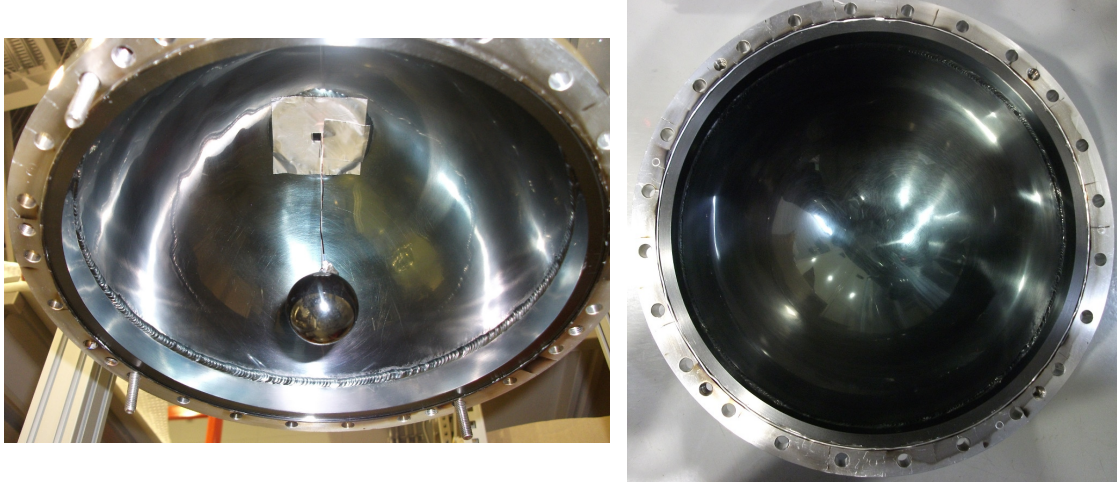


Figure 4.12: Left: photograph of the inner sphere suspended inside of the top half of the outer sphere. Right: photograph of the bottom half of the outer sphere.

was suspended by a nylon wire, thermal conduction of which is negligible ¹. The outer sphere was composed of two hemisphere-shaped vacuum chambers, as shown in Figure 4.12. The inner sphere and the inner surface of the outer sphere were buffed under #400 in JIS (Japanese Industry Standard), where whetstones with $\sim 30 \mu\text{m}$ in diameter polish the surfaces. Thermometers (DT-670-CU made by LakeShore, calibrated) were attached on the inner sphere (thermometer 1) and the outer sphere (thermometer 2). An aluminum tape covered the hole except the nylon wire to block out thermal radiation of 300 K coming through a pipe to the outer sphere. At the beginning of the experiment, the inside of the outer sphere was kept less than 10^{-3} Pa to prevent the residual gas molecules from transferring heat. This vacuum was necessary also to keep the sphere surfaces clean from water molecules, which can change the emissivity of the surfaces. Next, the outer sphere kept soaked into liquid nitrogen. Temperature of the outer sphere stayed at the boiling point of liquid nitrogen, 77 K. The temperature of the inner sphere and the outer sphere was monitored.

The measurement was conducted in four cases shown in Table 4.1. First, the inner sphere was suspended at the center point of the outer sphere. Next, to examine the dependence of heat transfer on the position of the inner sphere in the outer sphere, the inner sphere with DLC was shifted by 5 cm inside the outer sphere with DLC.

The intuitional understanding of the heat transfer in the two limiting surfaces is as follows:

- Diffusive surfaces

¹The extra heat loads, such as thermal conduction via the nylon wire, the thermometer wire (made of phosphor bronze), thermal radiation from the pipe were estimated. The extra heat is found to be negligible, as shown in Figure 4.14.

	Inner sphere	Outer sphere
1	Not coated	Not coated
2	Coated with DLC	Not coated
3	Coated with DLC	Coated with DLC
4	Not coated	Coated with DLC

Table 4.1: List of four cases in the small-scale experiments.

When the inner sphere is at the center point of the outer sphere, the relation that

$$Q_{\text{diff,center}}(T_1, T_2) = \frac{A_1 \sigma (T_1^4 - T_2^4)}{\frac{1}{\epsilon_1} + \frac{A_1}{A_2} \left(\frac{1}{\epsilon_2} - 1 \right)}, \quad (4.36)$$

can be obtained (e.g.[58]). No matter where the inner sphere exists in the outer sphere, rays from the inner sphere are reflected mainly by the outer sphere (rays rarely come back to the inner sphere). The heat transfer does not depend strongly on the position of the inner sphere in the outer sphere.

- Specular surfaces

When the inner sphere is at the center point of the outer sphere, all the rays from the inner sphere are reflected alternatively by the inner sphere and the outer sphere. This heat transfer is equal to the case where the two bodies are diffusive infinite parallel planes:

$$Q_{\text{spec,center}}(T_1, T_2) = \frac{A_1 \sigma (T_1^4 - T_2^4)}{\frac{1}{\epsilon_1} + \frac{1}{\epsilon_2} - 1} \quad (4.37)$$

(derivation is described in eq.(4.39)). If the inner sphere is shifted from the center point, rays are reflected by the outer sphere more times. Namely, more heat can be absorbed by the outer sphere. Thus, radiation can transfer more heat from the inner sphere to the outer sphere when the inner sphere is shifted from the center point. That is why eq.(4.37) is minimum heat transfer in the specular calculation.

Exact radiation heat transfer can be calculated by tracing rays using the Monte-Carlo method. Here, a c-code was used for this calculation. In the calculation, rays, obeying the Lambert's cosine law, are emitted from uniformly distributed positions on the inner sphere. (The total power is $\epsilon_1 A_1 \sigma T_1^4$. Here, A_i is surface area, T_i is temperature, ϵ_i is emissivity, and σ is the Stefan-Boltzmann constant. Index i ($= 1, 2$) represents the inner sphere and the outer sphere, respectively.) Next, the ray hits on the outer sphere. The ray is reflected or scattered to direction determined by the surface. If the surface is diffusive, the ray is reflected to a random direction, probability of which is proportional to $\cos \theta$ (θ is the angle between the surface normal and the reflected ray). If the surface is specular, the ray is reflected to the same angle

as its incident angle. After that, it hits on either the inner or the outer sphere depending on the position and the direction of the ray. When the ray hits on the sphere i , portion ϵ_i of its power is absorbed and the remaining portion $1 - \epsilon_i$ is reflected. (Reflectivity is equal to $1 - \epsilon_i$.) The same calculation for the direction of the next ray is repeated until the ray power becomes sufficiently small. The number of rays traced N_{ray} was increased to make deviation of calculated value with different random seeds less than 1%. Here, $N_{\text{ray}} = 10000$ was adopted. The fact that the power of radiation from the sphere i is proportional to T_i^4 and that no heat is transferred under $T_1 = T_2$ gives relation as:

$$Q(T_1, T_2) \propto A_1 \sigma (T_1^4 - T_2^4). \quad (4.38)$$

However, the factor depends on the position of the inner sphere in the outer sphere.

When the inner sphere is at the center point of the specular outer sphere, all the rays from the inner sphere are reflected alternatively by the inner sphere and the outer sphere. This case heat transfer can be easily calculated. Since $\epsilon_1 A_1 \sigma T_1^4$ is radiated from the inner sphere, $1 - \epsilon_2$ is reflected back, and $1 - \epsilon_1$ goes again to the outer sphere \dots , heat transfer is given as:

$$\begin{aligned} & \epsilon_1 A_1 \sigma T_1^4 [1 - (1 - \epsilon_2) + (1 - \epsilon_1)(1 - \epsilon_2) - (1 - \epsilon_1)(1 - \epsilon_2)^2 + (1 - \epsilon_1)^2(1 - \epsilon_2)^2 - \dots] \\ &= \epsilon_1 A_1 \sigma T_1^4 \frac{1 - (1 - \epsilon_2)}{1 - (1 - \epsilon_1)(1 - \epsilon_2)} \\ &= \frac{A_1 \sigma T_1^4}{\frac{1}{\epsilon_1} + \frac{1}{\epsilon_2} - 1}. \end{aligned} \quad (4.39)$$

Combining with eq.(4.38), eq.(4.37) can be obtained.

When the reflection by the outer sphere rarely comes back to the inner sphere, for example, in the case that the outer sphere is sufficiently larger than the inner sphere,

$$Q(T_1, T_2) = \epsilon_1 A_1 \sigma (T_1^4 - T_2^4). \quad (4.40)$$

4.4.3 Results

The results are shown in Figure 4.13. Heat transfer shown in Figure 4.14 was calculated from the cooling time. Each dot has an error bar of 10 % of the value of the heat transfer. This error is caused by the fact that the thermometer covers approximately 10 % of the surface area of the inner sphere. Result where the inner sphere is center can be compared with the case where the shift is 1 cm in the specular calculation because error of the position of the inner sphere is approximately 1 cm. Experimental results are consistent with the prediction for specular surfaces.

From the fitting to the result, the emissivity of DLC:

$$\epsilon_1 = \epsilon_2 = 0.3 \times \left(\frac{T}{300 \text{ K}} \right), \quad (4.41)$$

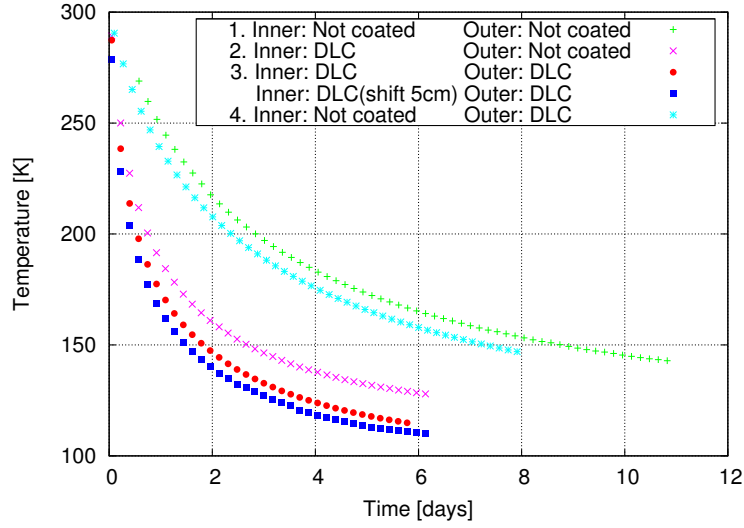


Figure 4.13: Cooling of the inner sphere. The outer sphere was kept at 77 K. The case without any coating is the slowest. The case with both the inner and the outer spheres coated is the fastest especially when the inner sphere is shifted from the center.

was obtained, which is proportional to temperature T . This fact can be explained as follows: the emissivity is equal to the absorptivity at the wavelength of radiation λ . The wavelength is inversely proportional to T according to Wien's displacement law in eq.(4.17). When the coating has a constant absorption coefficient, the absorptivity is proportional to the coating thickness d (approximately $1 \mu\text{m}$ in these experiments) and inversely proportional to λ . Namely, the coating looks thinner for longer wavelengths. Thus, the absorptivity is proportional to T .

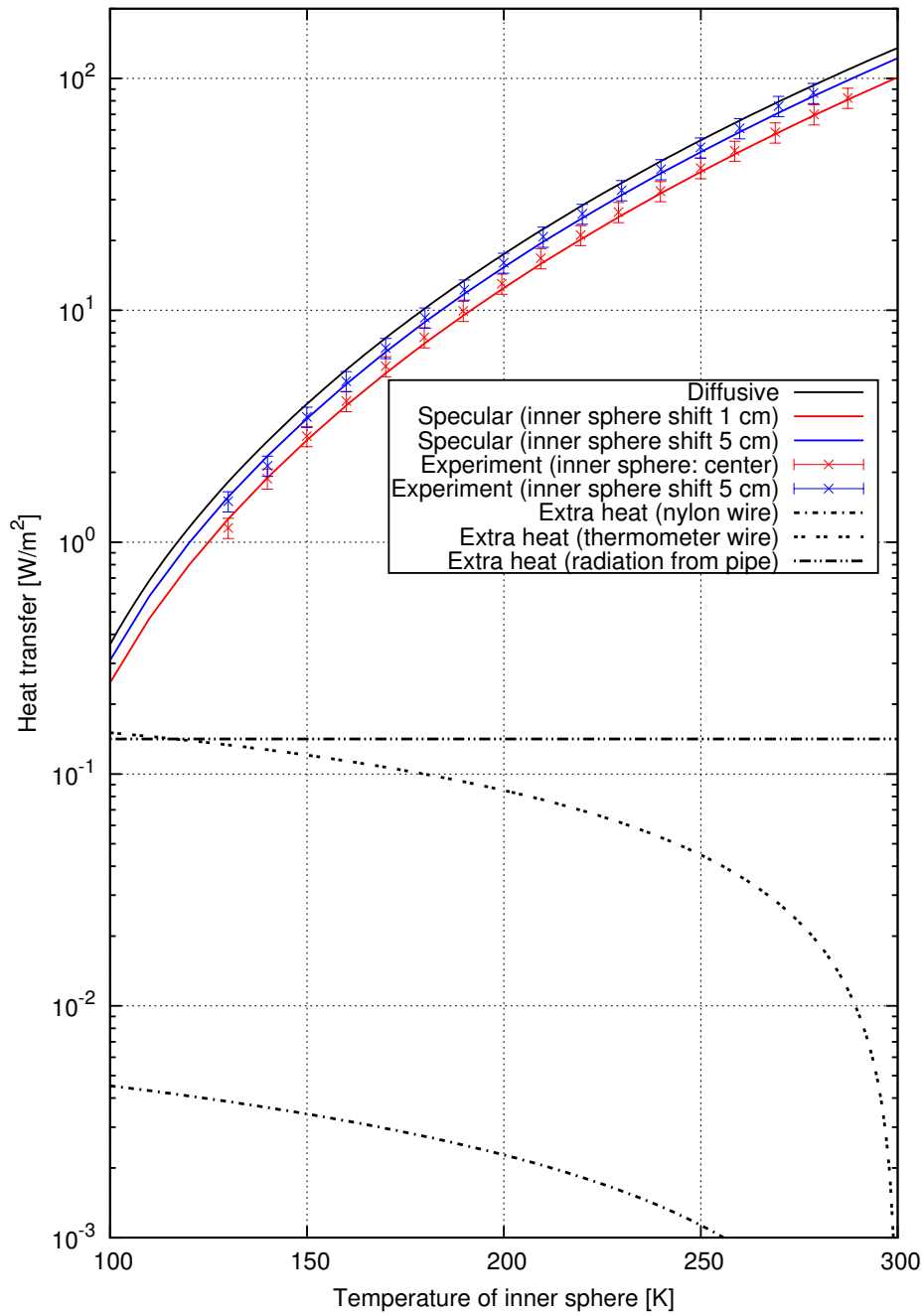


Figure 4.14: Heat transfer where both the inner and the outer spheres are coated with DLC. Calculation results of the diffusive surfaces and the specular surfaces are also shown. Result where the inner sphere is center can be compared with the case where the shift is 1 cm because error of the position of the inner sphere is approximately 1 cm. Since the calculation results of the diffusive surfaces were independent of the shift (1 cm or 5 cm) within the calculation error 1%, only the one is shown as “Diffusive.” Each error bar comes from the surface area covered by the thermometer on the inner sphere. This is systematic error acting in the same direction on the case where the inner sphere is at the center and on the case where it is shifted by 5 cm. Experimental results are consistent with the calculation using specular surfaces. This graph also shows that the extra heat is sufficiently smaller than the heat transfer interested.

4.5 Experiments in the actual KAGRA cryostat

4.5.1 Purpose

This experiment was conducted to confirm the calculation model of KAGRA described in Subsection 4.3 using the actual KAGRA cryostats.

4.5.2 Method

A cooling test of the KAGRA cryostats was conducted in Toshiba (manufacturing company of the cryostats), Yokohama, Japan[38, 25]. During the cooling test, spheres with and without the DLC coating, shown in Figure 4.15, were suspended inside the inner shields of cryostat No.1 and No.2, respectively, to focus on examining the emissivity of aluminum with and without the DLC coating. A half-sized payload, shown in Figure 4.16, was suspended in the inner shield of cryostat No.3. The holes for the laser beam and for the vibration isolation system were closed by aluminum plates to block out the 300 K thermal radiation. After the pressure reached the order of 10^{-3} Pa, the cryocoolers were turned on, and the cooling of the inner shield began. Temperature of the inner and outer shields was monitored using several thermometers (DT-670-CU made by LakeShore, not calibrated) on the shields.

The spheres are made of aluminum A5000 lathed and chemically polished (CP) with a diameter of 105 mm. One has no coating, and the other one is coated with DLC on the CP surface. Each sphere is hollow and made of two hemispheres. The total mass of each sphere is 1.2 kg. Thermometers (DT-670-CU made by LakeShore, not calibrated) were attached to each sphere. (Two thermometers were attached to each sphere to obtain the temperature gradient over the spheres.) The sphere was suspended at the position where the actual KAGRA mirror would be suspended (400 mm in height from the bottom of the inner shield) within the inner shield. As suspension wires, four Kevlar wires (commercial aramid fibers[59]), the thermal conduction of which is negligible, were used.

The half-sized payload was designed to have half the size of the actual KAGRA payload to reduce the cooling time (their parameters are shown in Figure 4.17). All the masses except the mirror were made of SUS304 and coated with DLC. Thermometers (DT-670-CU made by LakeShore, not calibrated) were attached to each mass. The payload was suspended within the inner shield by SUS wires, the thermal conduction of which is negligible. The mirror of the half-sized payload was at the position where the actual KAGRA mirror would be suspended (400 mm in height). Neither the aluminum heat links nor the sapphire fibers were used since this experiments concentrated on an analysis of the radiation cooling.

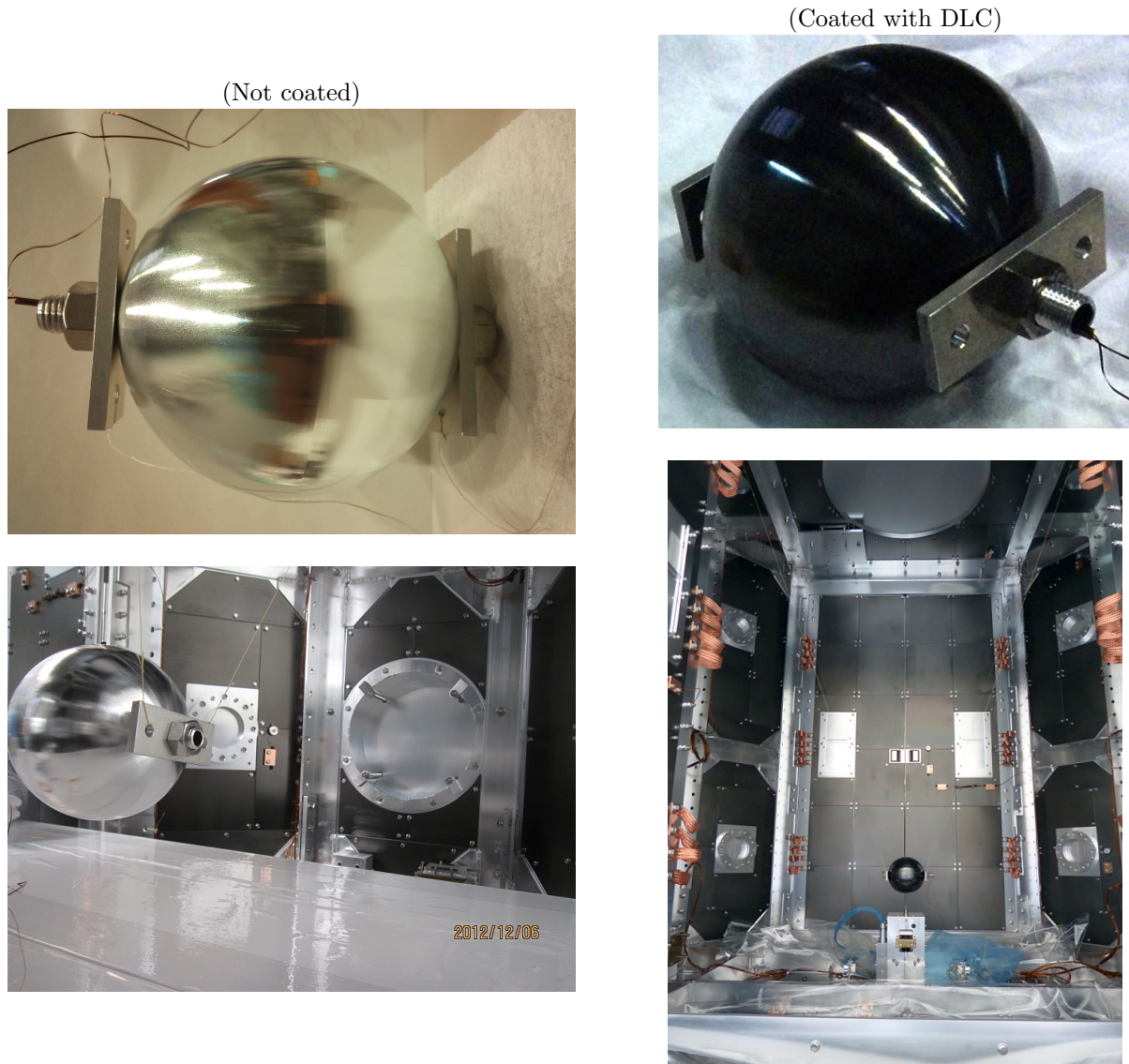


Figure 4.15: Photographs of the spheres suspended inside the inner shields of the KAGRA cryostats.

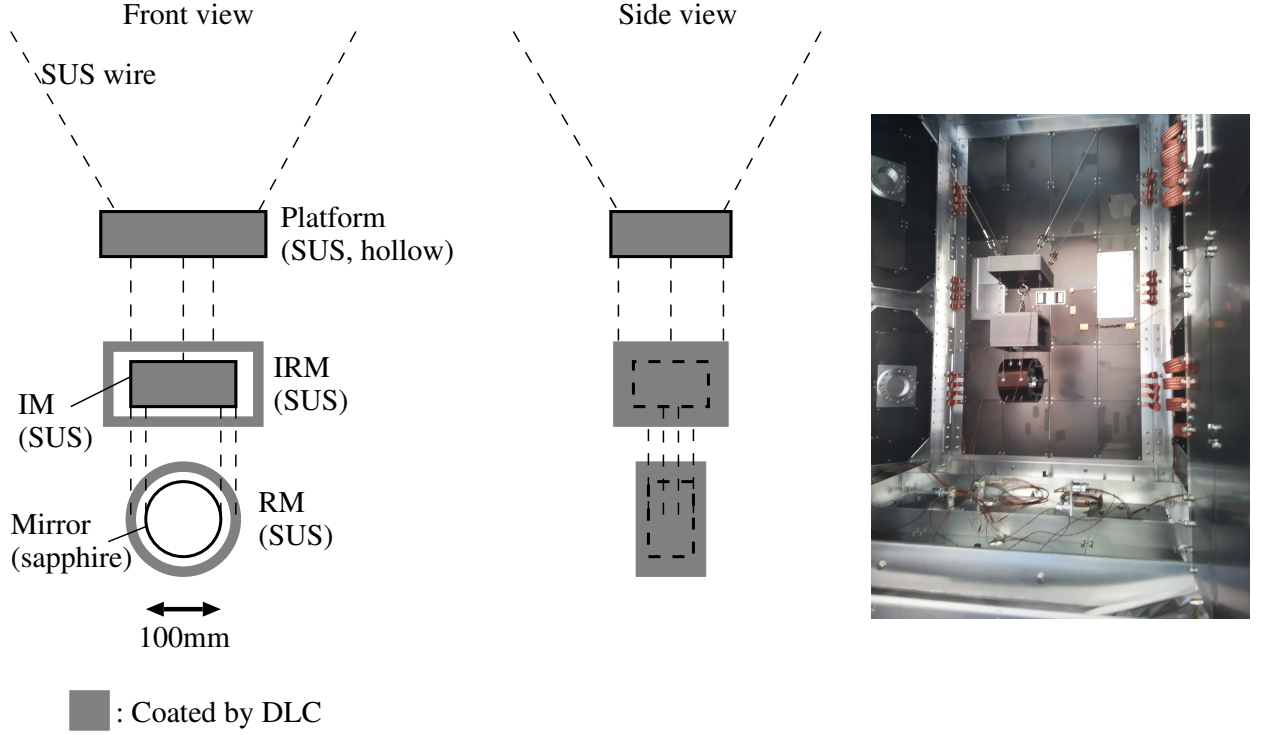


Figure 4.16: Schematic diagram and photograph of the half-sized payload. All the masses except the mirror were coated with DLC. The payload was suspended inside the inner shield by SUS wires[41].

4.5.3 Results

The results of the experiments are shown in Figures 4.18-4.20. The temperature of the spheres and each mass of the payload was also calculated from the temperature of the inner shield. In this case, the rays from the sphere or the payload rarely come back because the inner shield is not so symmetric as the outer sphere in the experiment described in Section 4.4, no matter the surface is diffusive or specular. (Less than 10^{-2} W comes back to the sphere per 1 W of radiation from the sphere according to calculation tracing rays specularly.) This is why diffusive and specular calculations yield the same results, which can be calculated by eq.(4.31) or eq.(4.40). Namely, the cooling time is independent of emissivity of the inner surface of the inner shield.

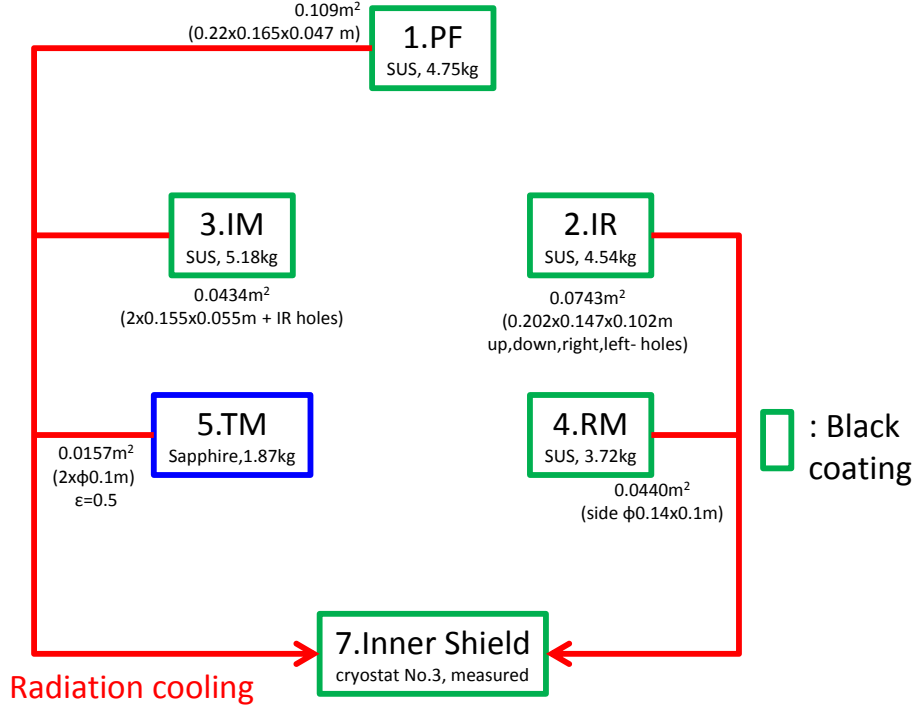


Figure 4.17: Schematic diagram of a calculation model of the half-sized payload. The inner surface of the inner shield and all the masses except the test mass (that is, the boxes with green borders) are coated with the high-emissivity coating. Dimension, mass, and effective surface area of each mass are shown.

4.6 Discussion

The small-scale experiment has verified the effect of the high-emissivity coating. The experimental results are found to be consistent with calculation using the specular surfaces. This fact means that the surfaces can be regarded as flat planes at wavelength of radiation. Wavelength of black body radiation is in the order of 10 μm at 300 K and longer at lower temperatures. On the other hand, as described in the Subsection 4.4.2, surface roughness of the spheres are around 30 μm . It is natural that the surface with smaller roughness than wavelength can be approximated as a flat plane.

The case where the inner sphere is diffusive and the outer sphere is specular, and the case where the inner sphere is specular and the outer sphere is diffusive, have also been calculated. The result was independent of whether the inner sphere is diffusive or specular within the calculation accuracy 1%. It only depends on whether the outer sphere is diffusive or specular. This

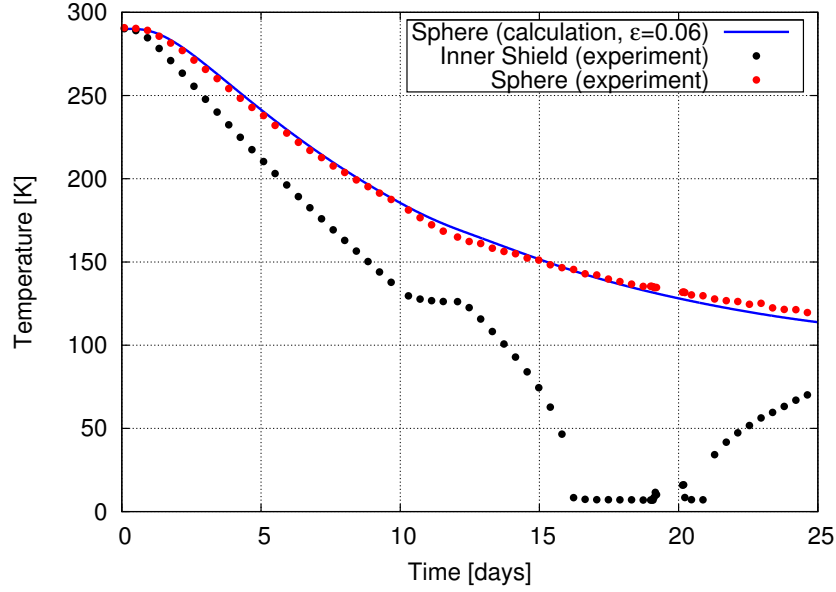


Figure 4.18: Results of the experiments in the KAGRA cryostats using the sphere without any coating. The temperature of the inner shield stayed constant between the 10th and the 12th day because the power supply was turned off. On the 21st day, the cryocoolers were turned off in order to heat up the cryostat. The calculated temperature of the sphere is the value calculated from the temperature of the inner shield, including the constant temperature between the 10th and the 12th day.

calculation shows that this experiment can distinguish the outer sphere diffusive or specular, not the inner sphere.

In the experiments in the actual KAGRA cryostat, the emissivity of the sphere without any coating and that of the sphere with the DLC coating was calculated from the temperature of the spheres and the inner shields using eq.(4.40). Figure 4.21 shows the result. The error bars come from temperature gradients over whole of the inner shields (4 K for cryostats No.1 and No.2) and over whole of the aluminum spheres (2 K for the sphere without coating and 0.5 K for the DLC sphere). These temperature gradients were obtained from data of the plural thermometers on the inner shield and the spheres. For the sphere without coating, the value when the power supply was turned off was removed. For the DLC sphere, the values over 200 K were removed because $T_1^4 - T_2^4$ in eq.(4.40) cannot be calculated due to small temperature difference between the inner shield and the sphere (smaller than or comparable to the temperature gradients of the inner shield and the sphere).

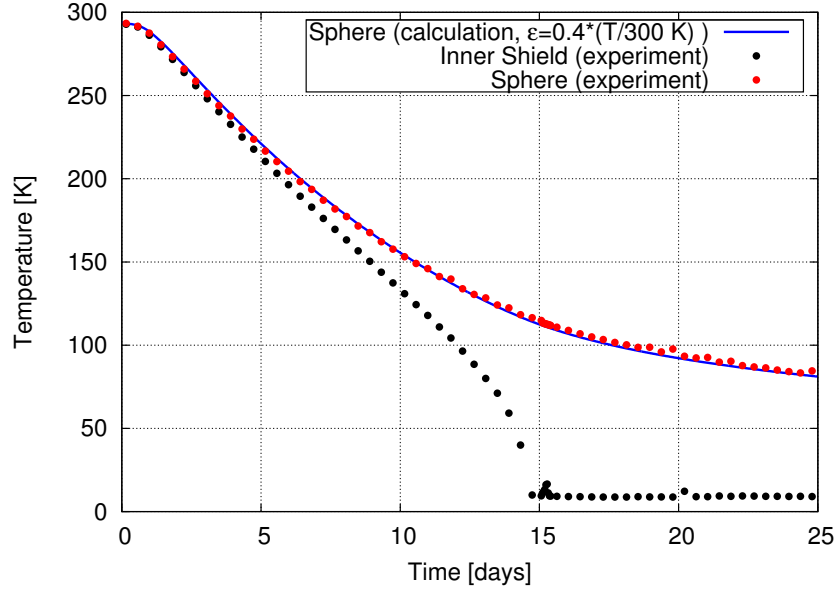


Figure 4.19: Results of the experiments in the KAGRA cryostats using the sphere with the DLC coating. The calculated temperature of the sphere is the value calculated from the temperature of the inner shield.

The weighted least squares method gives values of the emissivity:

$$\epsilon_{\text{sphere,no DLC}} = 0.052 \pm 0.002, \quad (4.42)$$

$$\epsilon_{\text{sphere,DLC}} = A \left(\frac{T}{300 \text{ K}} \right) + B \quad (4.43)$$

$$A = 0.24 \pm 0.07 \quad (4.44)$$

$$B = 0.04 \pm 0.03. \quad (4.45)$$

The fact that B is equal to $\epsilon_{\text{sphere,no DLC}}$ within the error indicates that the first term of eq.(4.43) corresponds to the absorption of coating layer and that the second term corresponds to the absorption of the aluminum surface. Equations (4.42) and (4.43) are also shown in Figure 4.21. In the temperature region which we are interested in, namely, temperature above 150 K, where thermal radiation is dominant in cooling of the KAGRA payload, the sphere with the DLC coating has a higher emissivity than the sphere without any coating. The effect of the DLC coating on the reduction of the cooling time has also been verified in the KAGRA cryostat. This is the first experiment in the world using an actual interferometric cryogenic gravitational wave detector.

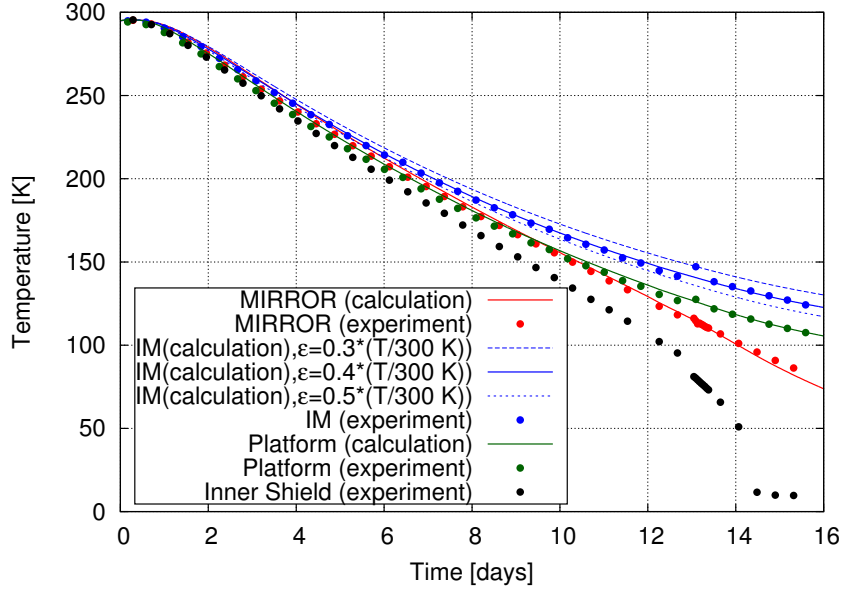


Figure 4.20: Results of the experiments in the KAGRA cryostats using the half-sized payload. The calculated temperature of the payload is the value calculated from the temperature of the inner shield.

To estimate the emissivity values of the payload, the emissivity values at 300 K ϵ_r in equation

$$\epsilon = \epsilon_r \left(\frac{T}{300 \text{ K}} \right) \quad (4.46)$$

are changed for each mass every 0.1. Figure 4.20 also shows the calculation results of IM as a representative with three different emissivity values. The values which fit the measured temperature best are:

$$\epsilon_{\text{Platform,DLC}} = 0.3 \times \left(\frac{T}{300 \text{ K}} \right) \quad (4.47)$$

$$\epsilon_{\text{IM,DLC}} = 0.4 \times \left(\frac{T}{300 \text{ K}} \right) \quad (4.48)$$

$$\epsilon_{\text{TM,sap}} = 0.5. \quad (4.49)$$

Equations (4.41), (4.43), (4.47) and (4.48) give several different values for the emissivity of the DLC coating. This can be caused by differences in the thickness of the coating or the surface treatment of the metal. And this is the reason why ϵ_r was changed every 0.1. Among these values, $0.3 \times (T/300 \text{ K})$ was used in the calculation of the cooling time of the KAGRA payload

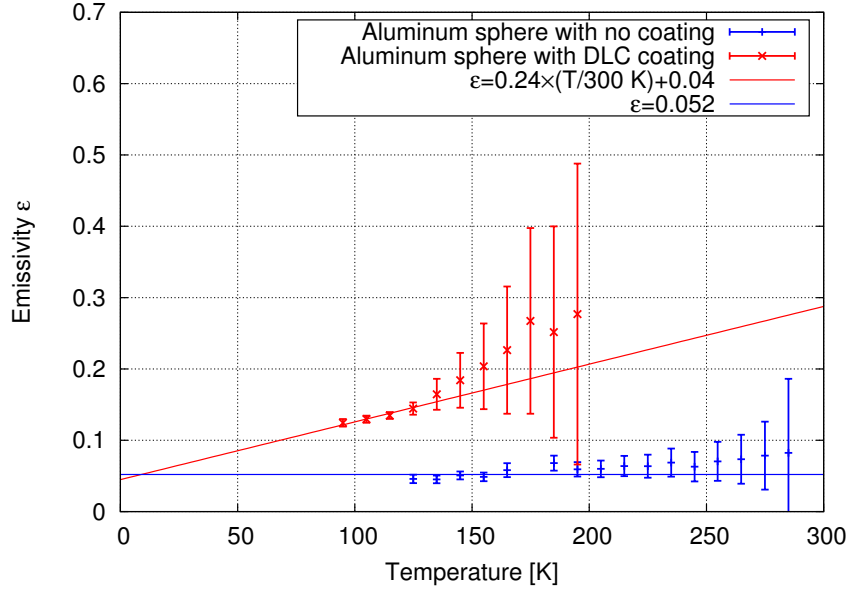


Figure 4.21: Calculated emissivity from the temperature of the spheres and the inner shields.

as shown in eq.(4.34). As described in Chapter 6, difference of 0.1 in the emissivity of the DLC coating corresponds to 5% difference in the total cooling time of KAGRA cooling system. The emissivity of sapphire obtained here was used in eq.(4.35).

The calculation model of the KAGRA cooling system and the calculated cooling time reduction with the DLC coating in Section 4.3 has been experimentally verified.

Duct shield

To reduce the cooling time and to cool down the mirror to the designed temperature, an extra heat load coming through the hole of the radiation shield should be reduced. For this purpose, the duct shields will be used in KAGRA. This chapter describes design and performance test of the duct shields.

5.1 Design of the duct shields

The cryostats contain only the mirrors and their suspension systems, and no 3 km beam duct, because it is difficult to cool the entire interferometer for its large scale. Although the mirror must be surrounded by the radiation shield, an opening in the shield is necessary to allow the laser beam to pass through. Large amount of 300 K thermal radiation would come through the opening without the duct shield. On the other hand, the amount of heat extractable from the mirror will be limited by the long and thin fibers. Thus, the duct shields are necessary to reduce 300 K thermal radiation. The idea is that the duct shield connected to a cryocooler with higher cooling power due to higher temperature (around 80 K) absorbs heat, which should not be absorbed by the mirrors. On the other hand, the duct shield can cause scattered light noise since the duct shield is placed near the mirror. When the scattered laser beam by the mirror is reflected by something vibrating (e.g. the duct shields), phase of the scattered light will be modulated by this vibration. If the scattered light comes back to the mirror and recombines to the main laser beam, it will affect the phase of the interferometer laser beam, and will cause noise.

As a result of the calculation about thermal radiation (Subsection 5.2.1) and the scattered light noise (Subsection 5.3), three duct shields, shown in Figure 5.1, have been manufactured. The duct shield is contained in a vacuum chamber, made of stainless steel. The duct was made by high-pure aluminum (15 mm in thickness, 1000 series with high thermal conductivity) to be cooled down easily. In the connected five ducts (each duct has 1 m in length), five baffles made by aluminum (5000 series with high strength to be shaped easily) are inserted every 1 m

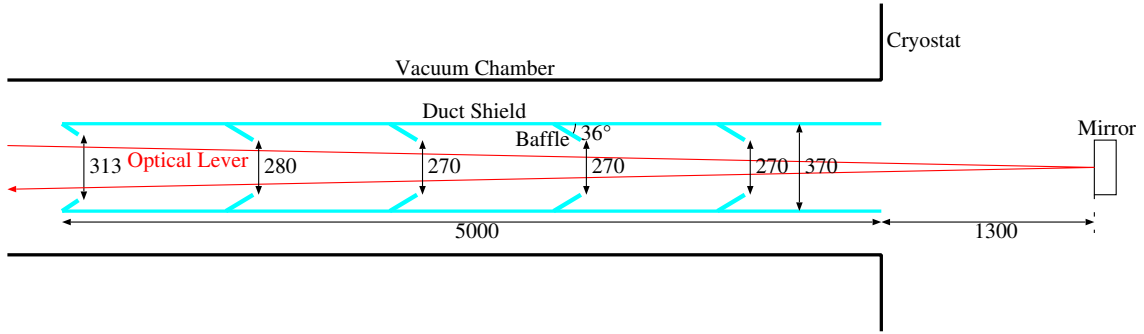


Figure 5.1: Schematic diagram of the duct shield (unit: mm). The five baffles are inserted every 1 m. The baffles are cone-shaped to catch the scattered light effectively.

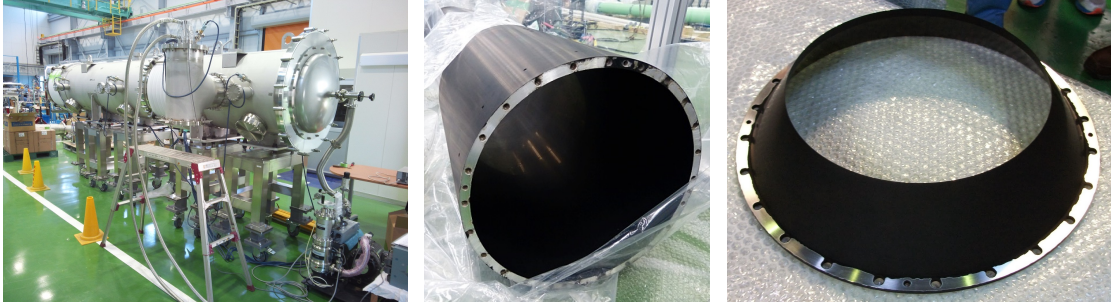


Figure 5.2: Photograph of the vacuum chamber including the duct shield, the duct (1 m), and the baffle, from the left hand side, respectively. The duct and the baffles are coated with a black coating Solblack. Whole of the duct shield (5 m) is composed of the five ducts and the five baffles.

to reduce thermal radiation by increasing the number of reflections. The baffles are designed not to block out the optical lever, which monitors the angle of the mirror, as shown in Figure 5.1. The ducts and the baffles are coated with a black-coating Solblack to enhance absorptivity for thermal radiation and the scattered light. All the Solblack surfaces used here were made as follows: (1) Aluminum was treated under ECB (Electro-Chemical Buffing). (2) Solblack was coated on the surface under standard condition (total thickness $18 \mu\text{m}$ including a black layer $2 \mu\text{m}$) by Asahi Precision. Co. Ltd. Reflectivity of Solblack coated on an aluminum sample was measured for three different incident angles using a CO_2 laser (wavelength $10.6 \mu\text{m}$). Figure 5.2 shows photographs of the vacuum chamber, the duct, and the baffle. Figure 5.3 shows photographs of inner surfaces of duct shields No.1-3. These photos are taken by a manually-focused camera with a flush light. From cryogenic temperature side, the surface looks entirely coated with Solblack since the aluminum surface without coating would have higher

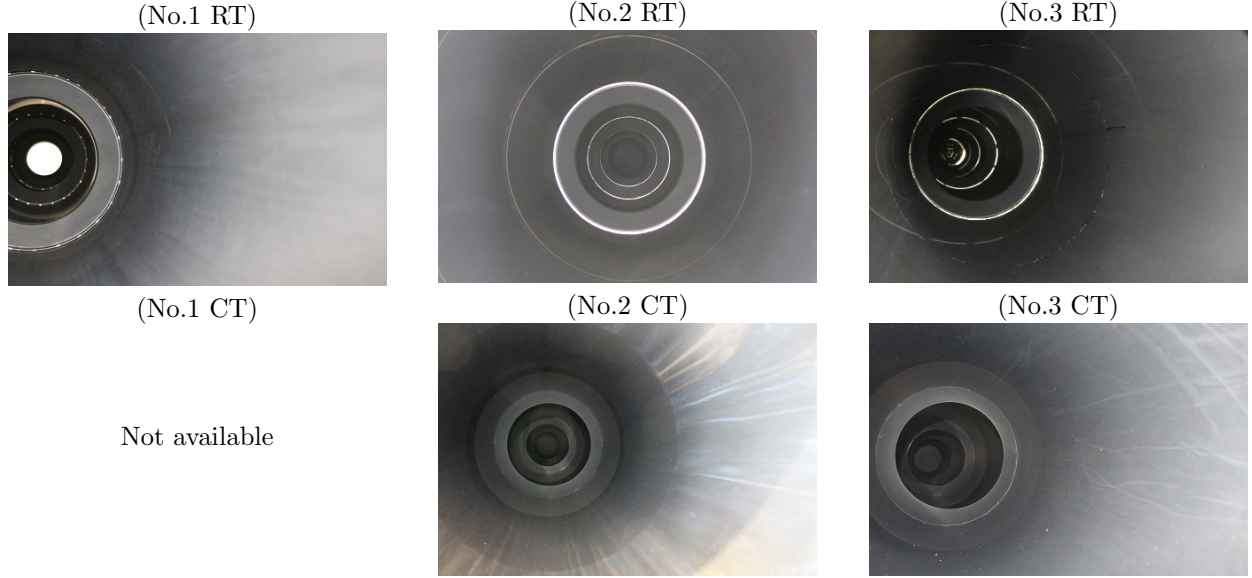


Figure 5.3: Photographs of inner surface of duct shields No.1-3. These are taken from room temperature (RT) side (side to the 3 km duct in KAGRA) and cryogenic temperature (CT) side (side to the mirror in KAGRA) of each duct shield.

reflectivity and strongly contribute to the scattered light noise.

The duct shield (mass 250 kg in total) was supported from the vacuum chamber by three stainless steel pipes (outer diameter 40 mm, inner diameter 38 mm) and six PEEK (polyetheretherketone, cross section 30 mm \times 10 mm, length 400 mm) bars. Multilayer insulators (MLI) surrounded the duct shield inside the vacuum chamber.

In the experiment described here, only the duct shield and the surrounding vacuum chamber were used without the KAGRA cryostat. Although one cryocooler will be attached to the duct shield with a vibration reduction stage[60] during KAGRA observation, the cryocooler was directly connected to the duct shield in this experiment. A single-stage Gifford-McMahon (GM) cryocooler, model CH-110 (typical cooling power 175 W at 77 K), manufactured by Sumitomo (SHI) Cryogenics of America, Inc. was used.

5.2 Thermal radiation

I constructed a calculation model of thermal radiation through the duct shield, designed the duct shield on a basis of the calculation, and then measured thermal radiation.

5.2.1 Calculation

A similar Monte-Carlo calculation of thermal radiation to one described in Section 4.4.2 was conducted. Since the duct surface is parallel to the direction of heat transfer, many reflections occurs at larger incident angle, where the black coating has higher reflectivity. Thus, calculation including dependence of the reflectivity on the incident angle was conducted on a commercial ray-tracing software ZEMAX. First, the duct shield was constructed in ZEMAX, as shown in Figure 5.4. Next, rays from any point selected randomly on the opening of the duct shield (the distribution of the point positions is uniform) at the left hand side of Figure 5.4 were traced. Their directions at the start points were chosen randomly with the distribution uniform over the solid angle. In this calculation, the rays are reflected only regularly by surfaces since the duct shield surfaces can be regarded as flat planes for thermal radiation as described in Section 4.4 or Section 5.4. Power of the j th ray was obtained by multiplying reflectivity R of the surface per each reflection (the incident angle for the k th reflection is $\theta_{j,k}$):

$$R(\theta_{j,1}) R(\theta_{j,2}) \cdots R(\theta_{j,N_j}). \quad (5.1)$$

The number of reflections of the j th ray by the surface of the duct is denoted as N_j . The measured reflectivity is shown in Figure 5.5. Interpolated value of this reflectivity was used for the calculation of thermal radiation. Some rays are reflected back while other rays pass through the duct shield. For the rays passing through the duct shield, the sum:

$$P = \frac{P_0}{N_{\text{ray}}} \sum_{j=1, \text{through duct}}^{N_{\text{ray}}} R(\theta_{j,1}) R(\theta_{j,2}) \cdots R(\theta_{j,N_j}) \quad (5.2)$$

was calculated. Here, P_0 is the total power emitted from the opening and j is the index for the N_{ray} rays. It is important to point out that in eq.(5.2), the rays returned to the room temperature side are excluded, and only those reflected to the cryogenic temperature side are included. N_{ray} was increased to make deviation of P smaller than 1 %. Here, $N_{\text{ray}} = 10^7$ was used.

Calculated heat input P is

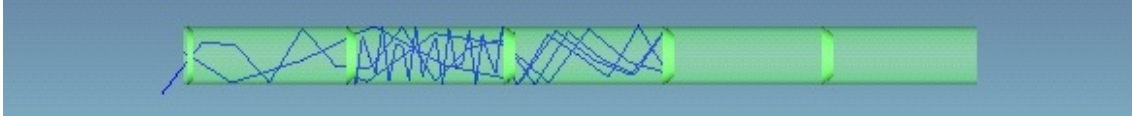
$$P = 0.19^{+0.08}_{-0.06} \text{ W}, \quad (5.3)$$

using

$$P_0 = \epsilon_0 \sigma T^4 (\pi a^2) = 49.4 \text{ W}, \quad (5.4)$$

where emissivity of radiation from the opening is assumed to be unity ($\epsilon_0 = 1$) for pessimistic estimation. The temperature T and diameter of the duct $2a$ were assumed to be 300 K and 0.370 m, respectively. The number and the positions of the baffles were determined to make P smaller than KAGRA requirement described in Subsection 5.4.

(a)



(b)

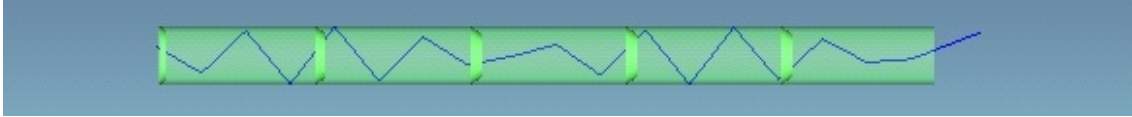


Figure 5.4: The duct shield constructed in the commercial ray-tracing software ZEMAX. (a) Some rays are reflected back by baffles. (b) Other rays pass through the duct shield.

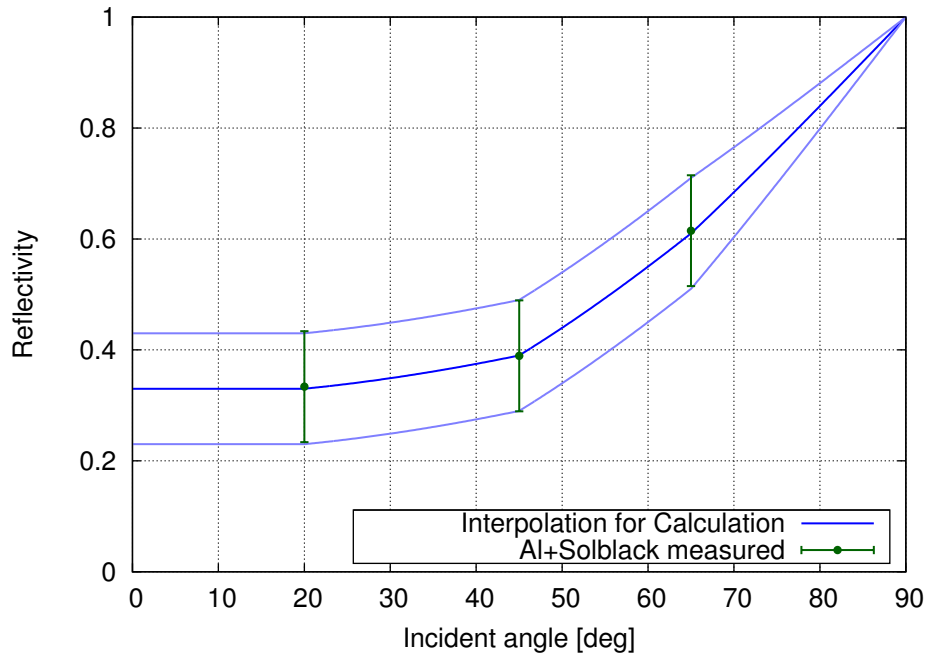


Figure 5.5: Reflectivity of Solblack on aluminum measured using CO₂ laser with wavelength 10.6 μm . Three dots represent measured values. The error bars are ± 0.1 , estimated variation over one sample or between several samples which comes from difference of surface treatment or surface roughness. The values are interpolated for the calculation.

5.2.2 Measurement

Method

To measure thermal radiation passing through the duct shield, two black aluminum plates were suspended at both edges of the duct shield, as shown in Figure 5.6. One was heated up to room temperature and radiated thermal radiation. The other absorbs thermal radiation through the duct shield, thermal radiation passing through the duct shield was derived from temperature of this plate. The plates thickness was made as thin as possible to decrease response time to heat. To keep rigidity of the thin plates, 5000 series of aluminum was used. Plate 1, suspended at the left edge, had 264 mm in diameter and 0.5 mm in thickness. Plate 2, suspended at the right edge, had 320 mm in diameter and 0.5 mm in thickness. Plates 1 and 2 had 230 g and 260 g, including aluminum blocks to attach heaters, respectively. To block out thermal radiation from the vacuum chamber, two aluminum flanges (1000 series of aluminum for good thermal conductivity) were attached to cover both the edges. The inner surfaces of the aluminum plates were coated by a black-coating Solblack to enhance absorptivity for thermal radiation, or emissivity. The Kevlar wires (commercial aramid fibers), thermal conductivity of which is negligible, were used to suspend the plates from the aluminum flanges. Each plate had thermometer and heater attached. Figures 5.7 and 5.8 show photographs of the plates and flanges.

Measurement was conducted after the duct shield cooled down completely as follows:

1. Plate 1 was heated up to 300 K by the heater.
2. Plate 1 was kept at 300 K by the heater until plate 2 reached constant temperature T_{eq} .
3. The heater on plate 1 was turned off to cool both plate 1 and plate 2.
4. The heater on plate 2 was turned on to heat up plate 2 to temperature T_{eq} . From the current and the voltage measured by the four electrodes method, the heater power P_{heater} was obtained.

Next, the same measurement where the roles of plate 1 and plate 2 were exchanged was conducted.

These measurements were repeated for three duct shields with the same specification to check if the same results were reproduced.

To confirm that the heat from the plates was extracted by the cryocooler, heat load test was conducted for duct shields No.1,3. Heat was input by a heater attached on the aluminum flange, “Duct Heater” shown in Figure 5.6. From this test, the relation between the heat from “Duct Heater” and temperature of the cryocooler cold head was obtained. If the heat from the plates satisfies this relation, the fact that the heat from the plates is extracted by the cryocooler can be confirmed.

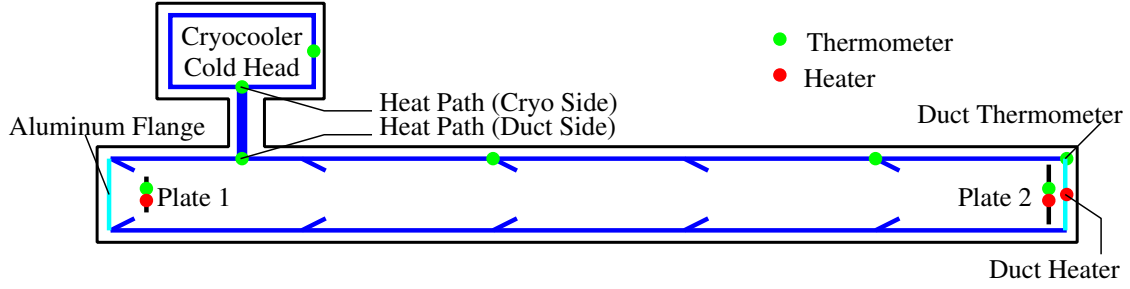


Figure 5.6: Schematic diagram of the experimental setup.

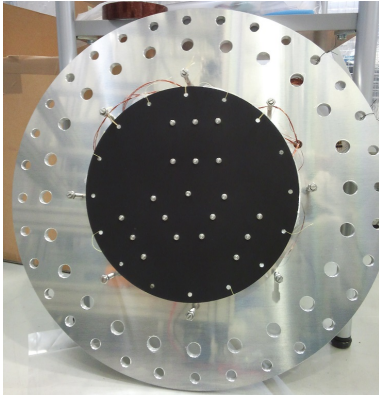


Figure 5.7: Photo of plate 1 suspended from the aluminum flange.

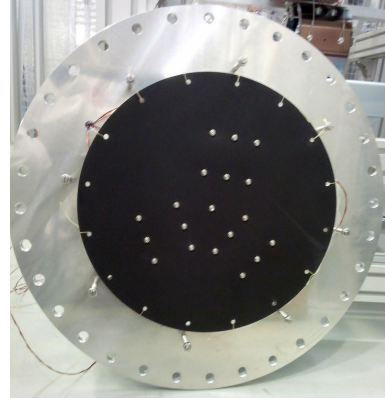


Figure 5.8: Photo of plate 2 suspended from the aluminum flange.

Result

Figure 5.10 shows the result of the thermal radiation measurement. Heat “Radiated by Plate 1” is calculated as:

$$P_{0,\text{plate1}} = \epsilon_1 \sigma T^4 S_{\text{plate1}}, \quad (5.5)$$

where $T = 300$ K, S_{plate1} is surface area of plate 1. Emissivity of Solblack ϵ_1 was assumed to be equal to absorptivity for incident angle 0:

$$\epsilon_b = 0.7 \pm 0.1. \quad (5.6)$$

The error bar in heat “Radiated by Plate 1” comes from this error in ϵ_b .

Heat “Absorbed by Plate 2 (calculation)” was calculated by the ray-tracing calculation as described in Subsection 5.2.1. While the calculation in Subsection 5.2.1 regarded the whole opening of the duct shield as the source or detector of rays, the calculation here changed

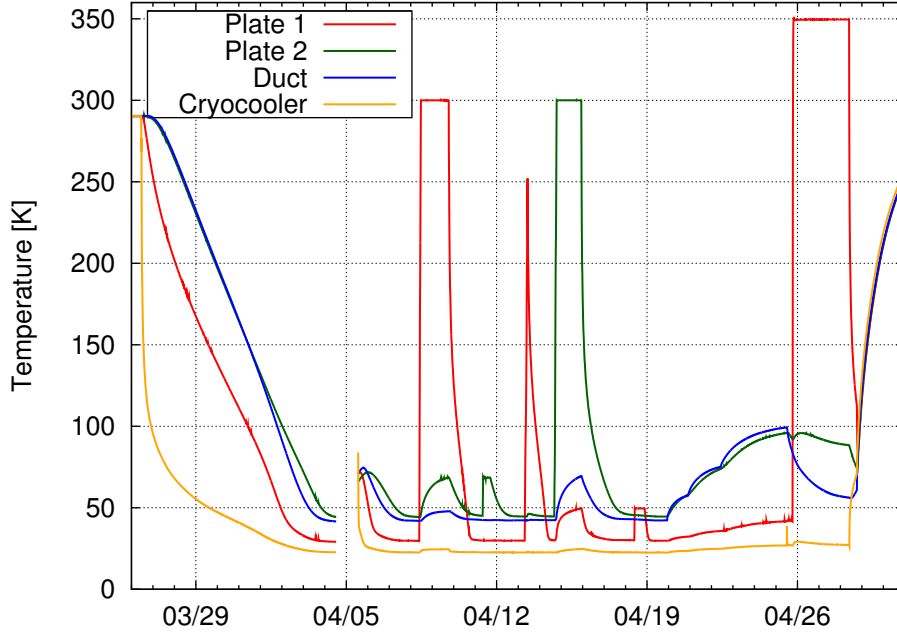


Figure 5.9: Temperature log of the duct shield No.1. A working log is shown in Table 5.1. “Duct” represents temperature measured by “Duct Thermometer” in Figure 5.6.

geometry of the ray source and the detector to that of the plates 1 and 2, respectively. It is important to point out that ϵ_b is multiplied twice when the ray is emitted from plate 1 as eq.(5.5) and when the ray is absorbed by plate 2. The error in the reflectivity is accumulated to yield larger error in the heat “Absorbed by Plate 2 (calculation)” since the ray is reflected by the duct shield many times.

Heat “Absorbed by Plate 2 (measurement)” is exactly the heat P_{heater} , which is applied by the heater on plate 2 to reproduce the temperature rise without the radiation from plate 1. The error comes from temperature rise of surrounding of plate 2, namely temperature of the duct. Although there is variance between the three duct shields, the result shows that the measured values are consistent with the calculation within the error.

When the roles of plate 1 and plate 2 were exchanged, heat “Absorbed by Plate 1 (measurement)” was obtained similarly. This heat should be equal to the heat “Absorbed by Plate 2 (measurement).” Otherwise, even if the two plates had the same temperature, heat would be transferred between them. The experimental result well agrees with this discussion for all of the three duct shields.

Figure 5.11 shows the result of the heat load test in duct shield No.1. The heat without

4/4	The duct shield was heated up due to stopping of power supply.
4/8	Plate 1 was heated up to 300 K.
4/9	Constant temperature of plate 2, $T_{\text{eq}} = 68.5$ K, was obtained.
4/11	Plate 2 was heated up to T_{eq} for calibration.
4/14	Plate 2 was heated up to 300 K.
4/18	Plate 1 was heated up for calibration.
4/20	Heat load test was conducted.
4/28	The cryocooler was turned off.

Table 5.1: Working log of the duct shield.

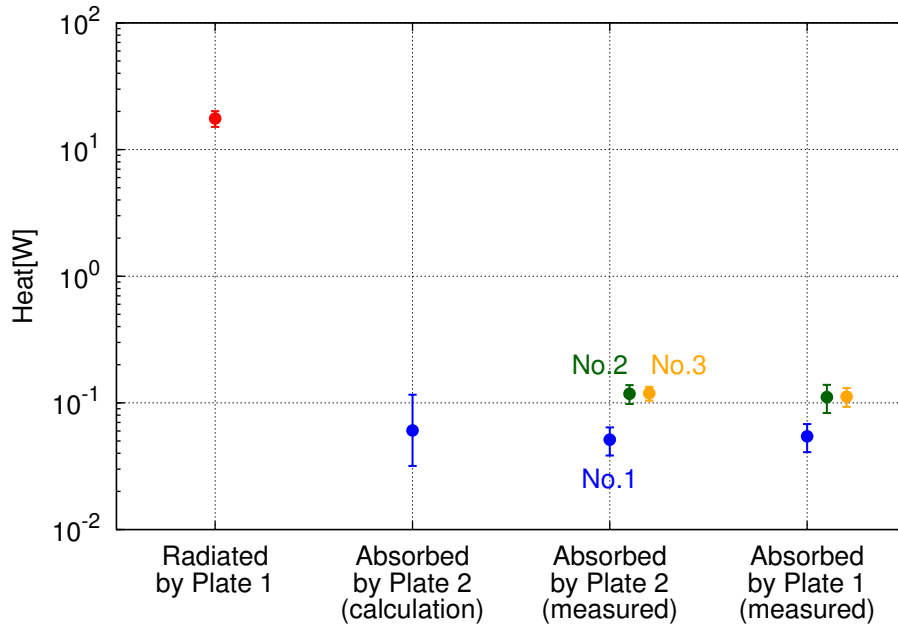


Figure 5.10: Result of the thermal radiation measurement. Heat “Radiated by Plate 1” was reduced by the duct shield to the level of heat “Absorbed by Plate 2.” Heat “Absorbed by Plate 1” represents the result where the roles of plate 1 and plate 2 were exchanged, namely, Plate 2 was heated up to 300 K. All the results for duct shield No.1-3 are shown.

heaters was estimated to be 11.5 W from the difference between the cold head temperature achieved in this experiment and the one without heat load[61]. This heat is mainly composed of thermal radiation through multilayer insulators (MLI) surrounding the duct shield and conduction via the support rods from the vacuum chamber to the duct shield. Since outer surface area of the duct shield is 6.28 m^2 , this heat corresponds to 1.8 W/m^2 . The linearity of the

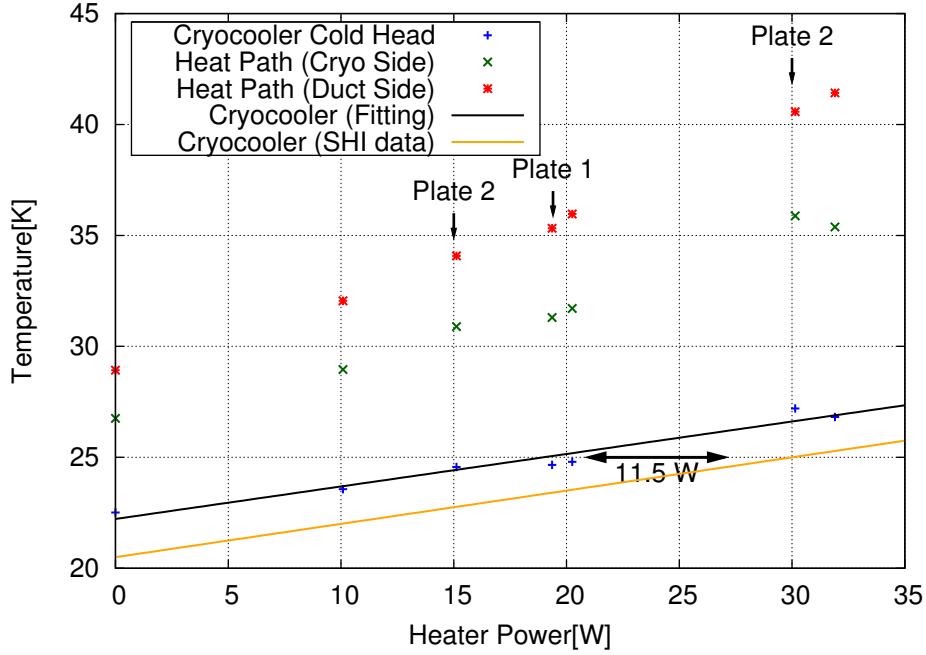


Figure 5.11: Result of the heat load test in duct shield No.1. “SHI data” shows the cooling power of the cryocooler without heat load[61]. The values when plate 1 or plate 2 was heated up is indicated by “Plate 1” or “Plate 2”. The heater attached on the aluminum flange was used for the other dots.

plot of the cold head temperature confirms that the heat from the plates was extracted by the cryocooler. This result was reproduced in duct shield No.3.

5.3 Scattered light noise

This section formularize scattered light noise, describes measurement of the duct shield vibration necessary to estimate the scattered light noise, and presents the calculated scattered light noise.

5.3.1 Formularization of the scattered light noise

The scattered light, the phase of which is modulated by vibration of the scatterer (here, the duct shield), contributes to the phase difference of the interferometer as follows: the electric field of the interfered light is proportional to

$$e^{i\phi_g} + Ae^{i\phi_s} \simeq 1 + A \cos \phi_s + i(\phi_g + A \sin \phi_s), \quad (5.7)$$

where $\phi_g (\ll 1)$ is the phase shift due to the gravitational waves, and $\phi_s (= 2kNx_s)$ is phase shift of the scattered light. Here, $k (= 2\pi/\lambda)$ is wave number, $\lambda (= 1 \mu\text{m})$ is wavelength of the laser, N is the number of reflections by the scatterer, and x_s is the displacement of the scatterer. Since effect of x_s is multiplied by N in the worst case, Nx_s was used instead of x_s . Amplitude scattering coefficient A is given as:

$$A = \sqrt{\frac{P_{\text{scat}}}{P_{\text{cav}}}}, \quad (5.8)$$

where P_{cav} is the arm cavity power, and P_{scat} is the scattered light power recombined to the main laser beam.

When $\phi_s \ll 1$, the equivalent GW amplitude of the scattered light is equal to GW causing phase shift of $A\phi_s$ [62] as:

$$h_{\text{scat}} \sim \frac{2Nx_s}{L}A \quad (x_s \ll \lambda), \quad (5.9)$$

where L is the arm length.

However, eq.(5.9) only includes linear term of the scatterer motion, which holds only when x_s is sufficiently small compared to the laser wavelength λ . When x_s is comparable to or larger than the laser wavelength λ , eq.(5.9) should be extended as[63]:

$$h_{\text{scat}} = \frac{2}{L}A [H_p(\omega)S(\omega) + H_a(\omega)C(\omega)]. \quad (5.10)$$

$S(\omega)$ and $C(\omega)$ are the amplitude spectral densities of $\sin(2kNx_s)$, and $\cos(2kNx_s)$, respectively. Equation (5.10) shows that $\sin \phi_s$ contributes to the phase and $\cos \phi_s$ contributes to the amplitude as eq.(5.7) shows. Here, $H_p(\omega)$ and $H_a(\omega)$ are represented as:

$$H_p(\omega) = \frac{1}{2} \frac{\lambda}{4\pi}, \quad (5.11)$$

$$H_a(\omega) = 2 \frac{\Gamma}{M} \frac{1}{\omega_0^2 - \omega^2} \frac{2}{c} P_{\text{cav}}. \quad (5.12)$$

These are the transfer functions from phase and amplitude of the light to displacement of the mirror, respectively. $\Gamma = 25$ is power gain of the signal recycling cavity, $M = 23 \text{ kg}$ is mass of the mirror, $\omega_0/(2\pi) = 1 \text{ Hz}$ is the suspension Eigen frequency, and c is the light speed.

5.3.2 Calculation of amplitude scattering coefficient

In this subsection, the amplitude scattering coefficient A is calculated, which depends mainly on geometry of the duct shields shown in Figure 5.1 as well as angular distribution of the scattered light from the mirror. As the angular distribution, scattering by microroughness of

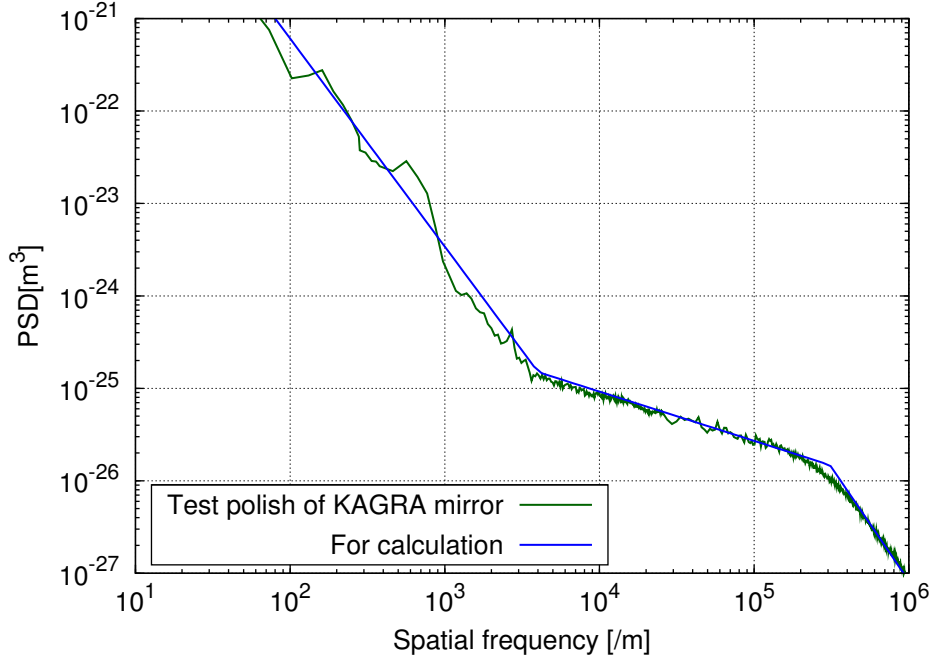


Figure 5.12: PSD of microroughness of the KAGRA test-polished mirror[40]. Values are fitted by $1.92 \times 10^{-17} f^{-2.25}$ ($f < 4 \times 10^3 \text{ m}^{-1}$), $1.25 \times 10^{-23} f^{-0.533}$ ($4 \times 10^3 \text{ m}^{-1} < f < 3 \times 10^5 \text{ m}^{-1}$), and $4.75 \times 10^{-13} f^{-2.46}$ ($3 \times 10^5 \text{ m}^{-1} < f$).

the mirror (scattering angle is determined by spatial wavelength of microroughness) and point scattering (light is uniformly scattered) are considered.

A range of θ which directly sees the duct shield is $\theta_{\min} < \theta < \theta_{\max}$, where

$$\theta_{\max} = 0.141 \text{ rad} = 8.10 \text{ deg} \quad (5.13)$$

$$\theta_{\min} = 0.0250 \text{ rad} = 1.43 \text{ deg}. \quad (5.14)$$

They correspond to spatial frequencies $f = \theta/\lambda$

$$f_{\max} = 1.33 \times 10^5 \text{ /m} \quad (5.15)$$

$$f_{\min} = 2.36 \times 10^4 \text{ /m}. \quad (5.16)$$

Scattering caused by microroughness of the mirror

Figure 5.12 shows a power spectral density (PSD) of microroughness of the KAGRA test-polished mirror. The Bi-directional Reflectivity Distribution Function (BRDF) can be calcu-

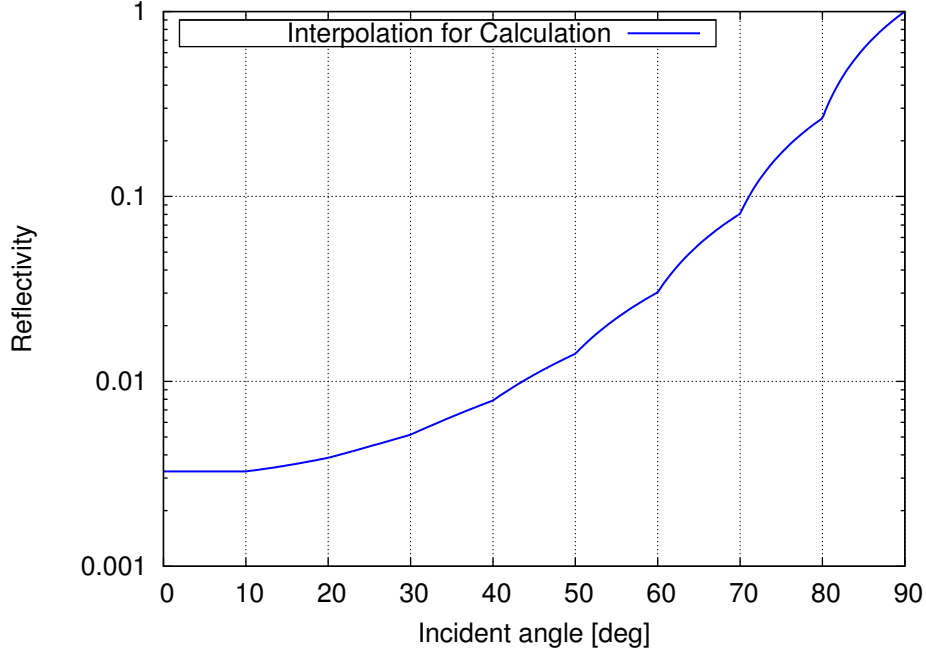


Figure 5.13: Reflectivity of Solblack on aluminum (ECB) measured at wavelength 650 nm by Genesis Corporation[65]. Eight values at $10^\circ, 20^\circ, \dots, 80^\circ$ were interpolated or extrapolated.

lated as[64]:

$$\frac{dP}{d\Omega}(\theta) = \left(\frac{4\pi}{\lambda^2}\right)^2 D \frac{\text{PSD}(f)}{f}. \quad (5.17)$$

Here, D was approximated as $1/(2\pi)$.

Thus, ratio of the input power to the cavity power is given as:

$$\frac{P_{\text{in}}}{P_{\text{cav}}} = \int_{\theta_{\text{min}}}^{\theta_{\text{max}}} \frac{dP}{d\Omega}(\theta) 2\pi \sin \theta d\theta = 5.09 \times 10^{-7}. \quad (5.18)$$

When the cavity power $P_{\text{cav}} = 400$ kW is assumed,

$$P_{\text{in}} = 0.204 \text{ W}. \quad (5.19)$$

Calculation of the scattered light recombined to the main laser beam was conducted on ZEMAX. First, the duct shield was constructed in ZEMAX. Next, rays from the center point of the mirror were traced. Their directions at the start point were chosen randomly with the distribution obeying eq.(5.17). When the ray hits the duct or the baffles, the power of the

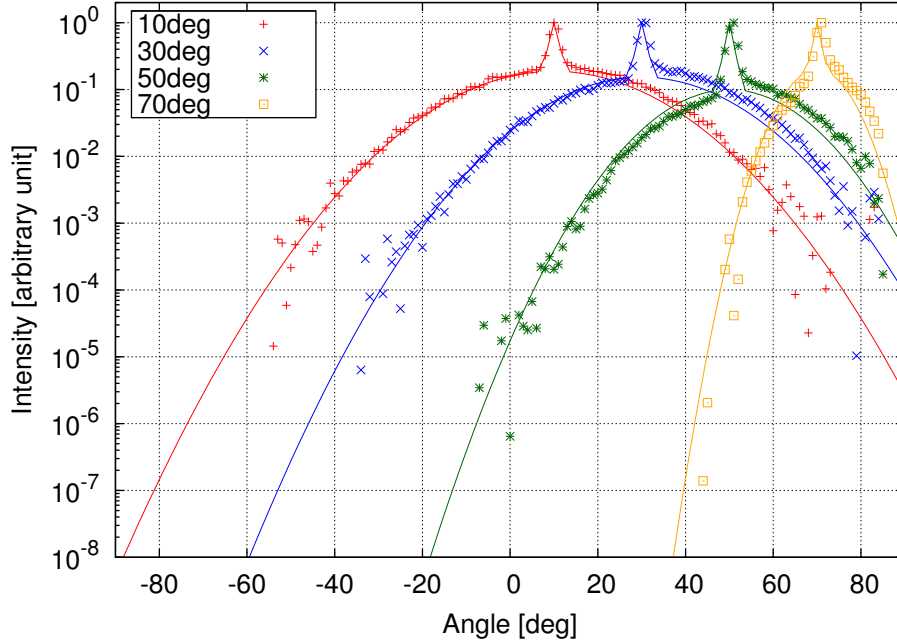


Figure 5.14: Angular distribution of rays reflected by Solblack on aluminum (ECB). The incident angle before the reflection was shown in the legend. The lines represent the fitted models to the data measured for white light by Genesis Corporation[65]. The dots represent the values obtained by ZEMAX using this model. There are seven models at the incident angles $10^\circ, 20^\circ, \dots, 70^\circ$ (here, only the representatives are shown). All the models were included in the calculation, and interpolated values by ZEMAX were used for the incident angle between them.

ray was multiplied by reflectivity, shown in Figure 5.13. The direction of the reflection was determined by the angular distribution function of the Solblack surface, shown in Figure 5.14, fitted curve to the measured values.

Power of the j th ray was obtained by multiplying reflectivity R of the surface per each reflection (the incident angle for the k th reflection is $\theta_{j,k}$):

$$R(\theta_{j,1}) R(\theta_{j,2}) \cdots R(\theta_{j,N_j}). \quad (5.20)$$

The number of reflections of the j th ray by the surface of the duct shield is denoted as N_j . Some rays are reflected back while other rays pass through the duct shield. For the rays reflected back by the duct shield, the sum which is represented as:

$$P_{\text{ref}} = \frac{P_{\text{in}}}{N_{\text{ray}}} \sum_{j=1, \text{reflected back}}^{N_{\text{ray}}} R(\theta_{j,1}) R(\theta_{j,2}) \cdots R(\theta_{j,N_j}) \quad (5.21)$$

was calculated. N_{ray} was increased to make deviation of P smaller than 10 %. $N_{\text{ray}} = 10000$ was used here. Since the input power eq.(5.19) is fixed and the angular distribution follows eq.(5.17) on ZEMAX, the sum \sum_j can be calculated easily.

Next, the light power recombined to the main beam is given as:

$$P_{\text{scat}} = \frac{P_{\text{in}}}{N_{\text{ray}}} \sum_{j=1, \text{reflected back}}^{N_{\text{ray}}} R(\theta_{j,1}) R(\theta_{j,2}) \cdots R(\theta_{j,N_j}) \frac{dP}{d\Omega}(\theta_{\text{scat},j}) \pi \theta_{\text{beam}}^2, \quad (5.22)$$

where $\theta_{\text{scat},j}$ is the angle between the j th ray coming back to the mirror and the surface normal of the mirror. Using the radius of the beam waist $w_0 = 0.016$ m, the diffraction angle of the main beam is as follows:

$$\theta_{\text{beam}} = \frac{\lambda}{\pi w_0} = 2.12 \times 10^{-5} \text{ rad}. \quad (5.23)$$

Scattering caused by point defects of the mirror

Point defects on the mirror cause wide angle scattering. Its angular distribution can be assumed as uniform over $0 < \theta < \pi/2$:

$$\frac{dP}{d\Omega}(\theta) = \frac{1 \times 10^{-5}}{\pi} \cos \theta \quad (5.24)$$

with total scattered power:

$$\int_0^{\pi/2} \frac{dP}{d\Omega}(\theta) 2\pi \sin \theta d\theta = 10 \text{ ppm}. \quad (5.25)$$

The ratio of the input power to the cavity power is evaluated as:

$$\frac{P_{\text{in}}}{P_{\text{cav}}} = \int_{\theta_{\text{min}}}^{\theta_{\text{max}}} \frac{dP}{d\Omega}(\theta) 2\pi \sin \theta d\theta = \frac{1 \times 10^{-5}}{2} (\cos 2\theta_{\text{min}} - \cos 2\theta_{\text{max}}) \quad (5.26)$$

$$= 1.91 \times 10^{-7}. \quad (5.27)$$

When the cavity power P_{cav} of 400 kW is assumed,

$$P_{\text{in}} = 0.0765 \text{ W}. \quad (5.28)$$

Using the above equations, eq.(5.22) can be calculated.

Calculated results

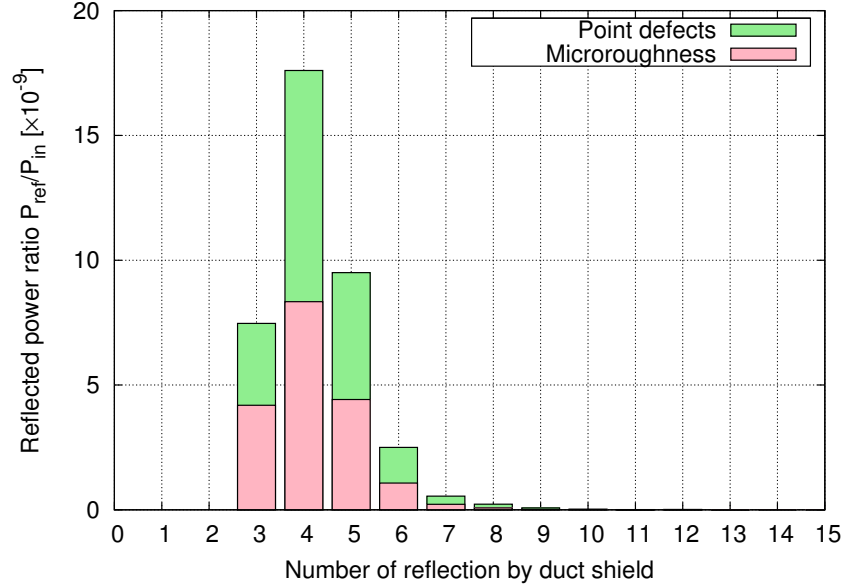
Amplitude scattering coefficient A was calculated by eq.(5.22) using ZEMAX in Table 5.2.

$$A^2 = A_{\text{Microroughness}}^2 + A_{\text{Point defects}}^2 = 8.00 \times 10^{-29} \quad (5.29)$$

$$A = 8.94 \times 10^{-15} \quad (5.30)$$

was obtained. Contribution to $P_{\text{ref}}/P_{\text{in}}$ from each number of reflections is shown in Figure 5.15.

	$P_{\text{in}}/P_{\text{cav}}$	$P_{\text{ref}}/P_{\text{in}}$	$P_{\text{scat}}/P_{\text{in}}$	$A^2 = P_{\text{scat}}/P_{\text{cav}}$	A
Microroughness	5.09×10^{-7}	1.84×10^{-8}	1.24×10^{-22}	6.31×10^{-29}	7.94×10^{-15}
Point defects	1.91×10^{-7}	1.97×10^{-8}	8.84×10^{-23}	1.69×10^{-29}	4.11×10^{-15}

Table 5.2: Detailed calculation results of amplitude scattering coefficient A Figure 5.15: Contribution to $P_{\text{ref}}/P_{\text{in}}$ from each number of reflections

5.3.3 Measurement of duct shield vibration

Vibration of the duct shield was measured in Saitama prefecture, where seismic motion is higher than that in Kamioka. And then, the result was converted to the seismic vibration level in Kamioka.

Method

Although the vacuum chamber will be rigidly fixed to the ground by five legs, vibration was measured with the five legs on casters here as shown in the photo of Figure 5.2 or Figure 5.17. The number of legs was increased as much as possible within the space to fix rigidly and then to reduce vibration. Result of finite element analysis of the duct shield and the vacuum chamber in Figure 5.16 shows that 26 Hz mode has the larger amplitude on the duct shield and that 33 Hz mode has the larger amplitude on the vacuum chamber. Namely, the frequency of the

second mode ~ 30 Hz, near to the frequency of the first mode, a good indicator of the rigidity, is currently limited by the vacuum chamber.

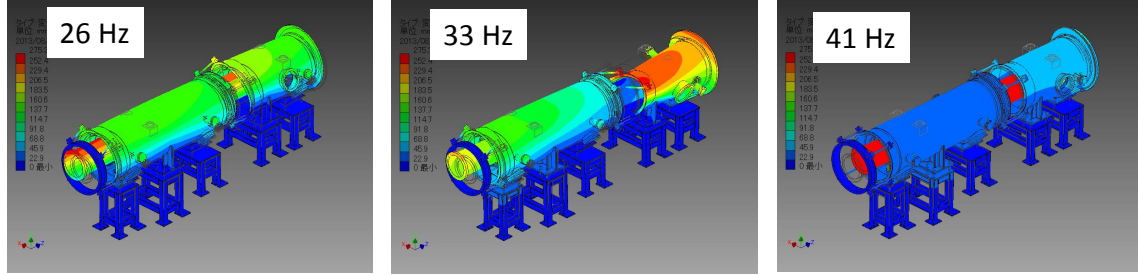


Figure 5.16: Result of finite element analysis of the duct shield and the vacuum chamber by S.Koike. Displacement and frequencies of mechanical resonances from the lowest mode to the 3rd mode are shown.

To measure seismic vibration, the accelerometer unit MMI-06 made by Tokkyokiki Corporation was used. It is composed of three sensors to measure vibration. These sensors were placed at the ground of the laboratory (Jecc Torisha Co, Ltd in Saitama prefecture), and measured the three directions of seismic vibration as shown in Figure 5.17. Relative displacement between the ground and the duct shield was measured by a laser displacement sensor (LV-9300 Ono Sokki) as shown in Figure 5.18 when the duct shield was completely cooled down. Here, the laser displacement sensor was used since the accelerometer could not operate in cryogenic temperature. Vibration under the condition where the cryocooler is turned on and off was measured. Although the cryocooler will be attached to the duct shield with the vibration reduction stage during KAGRA observation, the cryocooler was directly connected to the duct shield in this experiment. The data when the cryocooler is turned on is for reference. Signals from the accelerometers and the laser displacement sensor were sampled at 1 kHz for 1 minute. The power spectral density was estimated using Welch's method with Hanning window.

Result

Figure 5.19 shows vibration measured at 12:03 on 24 June, 2014. The seismic motion in vertical direction was several times larger than that in horizontal direction above 3 Hz. Floor level of the duct shield vibration between 3 Hz and 40 Hz is comparable to the vertical seismic vibration. The peak around 20 Hz is clearly seen in the duct shield vibration, which seems to correspond to the first mode shown in Figure 5.16. No peak around 1.7 Hz from circulation of compressed helium gas of the cryocooler cold head could be seen.

From the measurement, transfer function from the seismic motion to the vibration of the duct shield was calculated when the cryocoolers are turned off. Namely, the ratio of the shield vibration to the seismic vibration is equal to the transfer function. Using the seismic motion

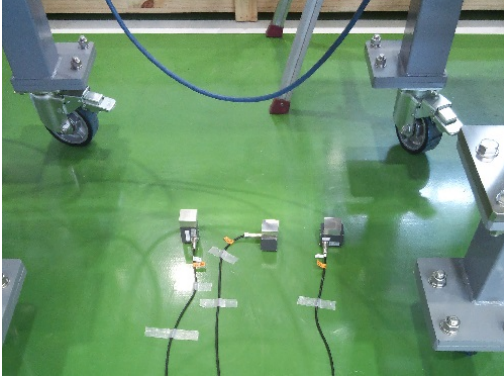


Figure 5.17: Photograph of the three accelerometers on the ground.



Figure 5.18: Photograph of the laser displacement sensor to measure vibration of the aluminum flange attached to the duct shield. There is a window in the vacuum chamber. Using Doppler shift of modulation of the laser light reflected by the duct shield, the displacement was measured.

measured at Kamioka, vibration of the duct shield at Kamioka was estimated. The duct shield vibration at Kamioka without any cryocooler operation, product of the transfer function and the seismic vibration at Kamioka, is shown in Figure 5.20. Since the place where the measurement was conducted has two orders of magnitude larger seismic vibration than that in Kamioka, it is likely to hide the cryocoolers vibration even if the cryocoolers are turned on in this measurement. In future, it is necessary to measure the vibration of the duct shield at Kamioka when the cryocoolers are turned on.

To estimate the scattered light noise caused by the estimated shield vibration shown in Figure 5.20, $S(\omega)$ and $C(\omega)$ were calculated. Using a self-correlation function $R_\phi(\tau) = \langle \phi_s(t)\phi_s(t+\tau) \rangle$, self-correlation functions of $\sin(2kNx_s)$ and $\cos(2kNx_s)$ are

$$R_S(\tau) = \sinh[R_\phi(\tau)] e^{-R_\phi(0)} \quad (5.31)$$

$$R_C(\tau) = \cosh[R_\phi(\tau)] e^{-R_\phi(0)}, \quad (5.32)$$

respectively, according to Appendix D of Ref.[66]. Fourier transformations of these are equal to power spectral density of $\sin(2kNx_s)$ and $\cos(2kNx_s)$. Figure 5.21 shows $S(\omega)$ with $N = 1, 10$. Figure 5.22 shows the calculation result.

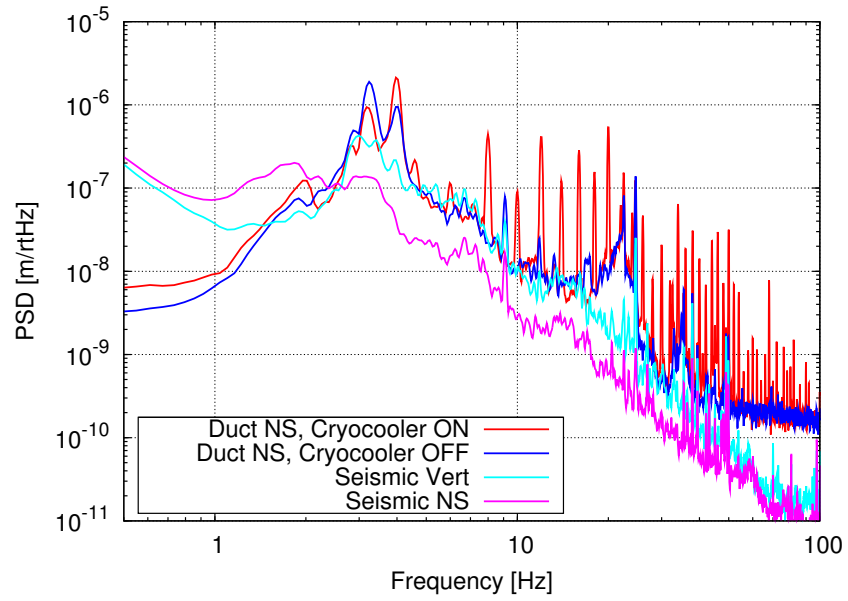


Figure 5.19: Result of vibration measurement (NS: the direction along the duct, Vert: vertical direction).

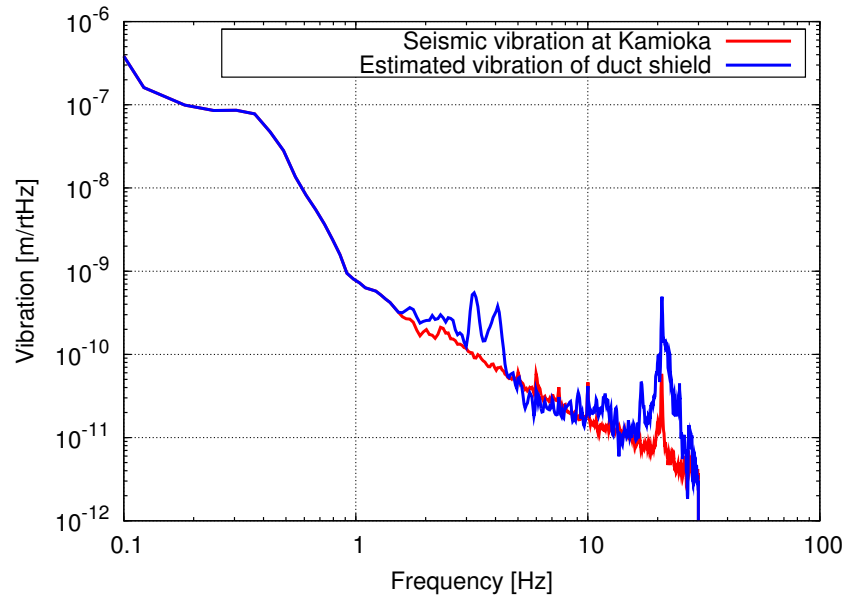


Figure 5.20: Estimated vibration of the duct shield at Kamioka. The seismic vibration was measured by a seismometer CMG-3T at 16:00 on 22 August, 2011 in Kamioka.

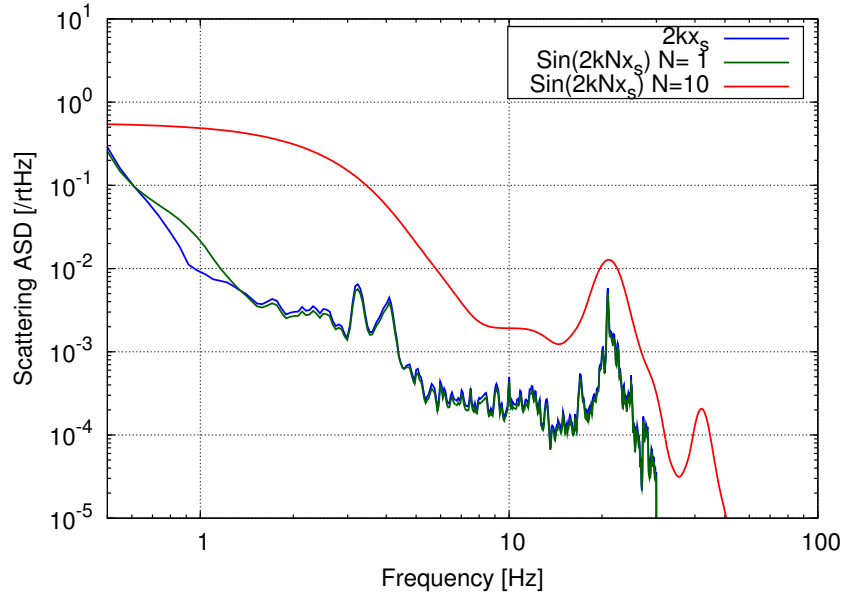


Figure 5.21: Calculated scattering amplitude spectral density (ASD)

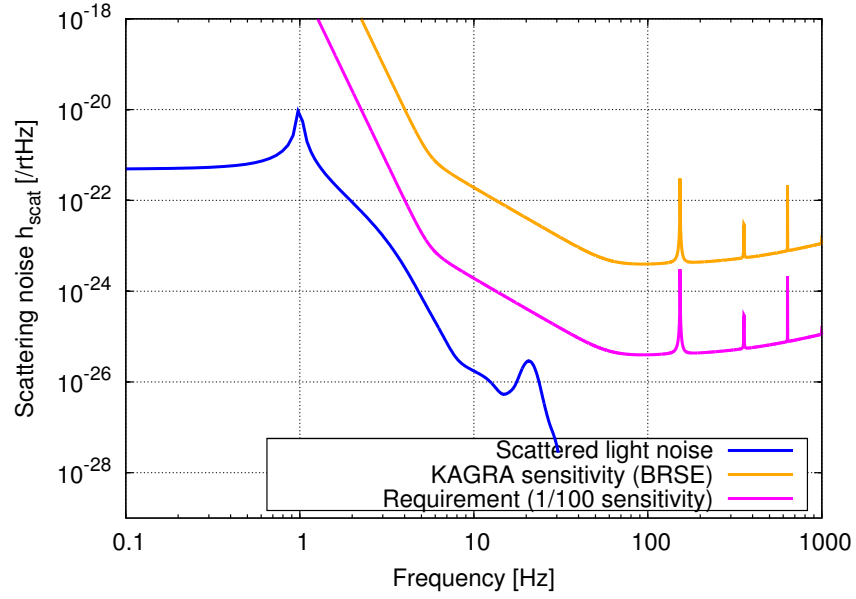


Figure 5.22: Scattered light noise caused by the duct shield at Kamioka without any cryocoolers. KAGRA sensitivity was taken from Ref.[67].

5.4 Discussion

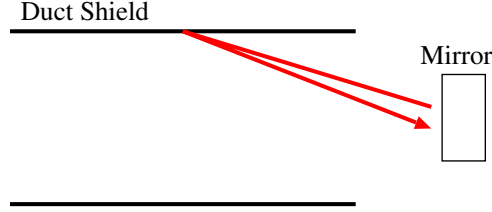


Figure 5.23: Back scattering. The light scattered at the mirror is scattered again at the duct shield, and directly goes back to the mirror.

Figure 4.2 shows that a diffusive pipe can reduce thermal radiation more effectively than a specular pipe. However, the KAGRA duct shields (and also the 3 km duct) are basically designed to be specular for the main laser beam (wavelength $1\ \mu\text{m}$) because the diffusive surface would cause back scattering (shown in Figure 5.23, these back scattered light would be hit only once by the black duct surface, and thus would have higher light power) to contribute to the scattered light noise strongly. Namely, the surface roughness of the duct shields should be less than $1\ \mu\text{m}$. To obtain this flat surface, the ducts and the baffles were treated under ECB (Electro-Chemical Buffing) before the Solblack coating. For thermal radiation, wavelength larger than $10\ \mu\text{m}$, this roughness is sufficiently small. This is why the experimental results are consistent with the specular calculation.

According to eq.(5.3), based on the calculation verified experimentally here, heat around 0.5 W at most will enter the cryostat containing the mirror since there are the two duct shields per one mirror. Heat absorbed by the mirror is typically $1/10$, product of absorptivity of the mirror and solid angle of the mirror viewed from the cryostat aperture. Namely, the mirror absorbs 50 mW, which is sufficiently smaller than the designed heat (1 W including absorption of the main laser[25, 54]). Thus, thermal radiation through the duct shield satisfies the requirement of KAGRA. Here, validity of the specular calculation and sufficient reduction of thermal radiation by the duct shield have been experimentally shown in an interferometric cryogenic gravitational wave detector for the first time in the world.

Although the measured values of thermal radiation through the three duct shield are within the error, there is variance between the duct shields. For duct shield No.1, the measured value is around the center value of the calculation. For duct shields No.2,3, the measured values are near the upper edge of the error bar in the calculation. These difference possibly comes from difference of reflectivity of Solblack over whole of the duct inner surface of the three duct shields, due mainly to non-uniform thickness of Solblack (deviation of reflectivity, and thus deviation of thickness on the assumption that the absorptivity is proportional to the thickness, should be around 20 % according to the error bar in Figure 5.5) and partly to cracks or dripping of

Solblack.

The calculated scattered light noise is found to satisfy requirement of KAGRA (1/100 of the goal sensitivity). It is necessary to investigate performance of the cryocooler vibration reduction stage and to measure the duct shield vibration in Kamioka when the cryocooler is turned on with the stage in future.

Discussion and conclusion

6.1 Discussion

Duty factor of KAGRA

To calculate how much the duty factor can be increased in KAGRA, time necessary for one cycle of heating up and cooling down is summarized in Table 6.1. Time for cooling down is the calculation result shown in Chapter 4. Time for heating up is measured value during the cooling test of the cryostats. “Other maintenance” includes repairing or adjusting some apparatus inside the cryostat and so on. Time for this “Other maintenance” is just assumption. Assuming that this cycle happens every 300 days, as shown in eq.(3.10), the duty factor of KAGRA has been increased from 71 % to 77 % as a result of introducing the high-emissivity coating.

	No coating	With coating
Cooling down	58	39
Heating up (using nitrogen gas)	10	10
Other maintenance	20	20
Total	88	69

Table 6.1: Time necessary for one cycle of heating up and cooling down.

Scale dependence

Dependence of the cooling time on scale is discussed. Using length scale ℓ of mass M to be cooled down,

$$M \propto \ell^3, \quad (6.1)$$

since mass is proportional to its volume. Although heat conducted by thermal conduction Q_c is constant with the same conduction wires, heat conducted by thermal radiation Q_r is written

as:

$$Q_r \propto \ell^2 \quad (6.2)$$

since Q_r is proportional to surface area of the mass. According to eq.(4.30), the cooling time t is represented as:

$$t \propto \frac{M}{Q}. \quad (6.3)$$

Thus, eq.(6.3) gives relation:

$$t \propto \ell^3 \quad (6.4)$$

for conduction cooling, and relation:

$$t \propto \ell^1 \quad (6.5)$$

for radiation cooling. This discussion shows an advantage of thermal radiation for larger-scale mass, which will be used in higher-sensitivity future detectors.

Emissivity dependence

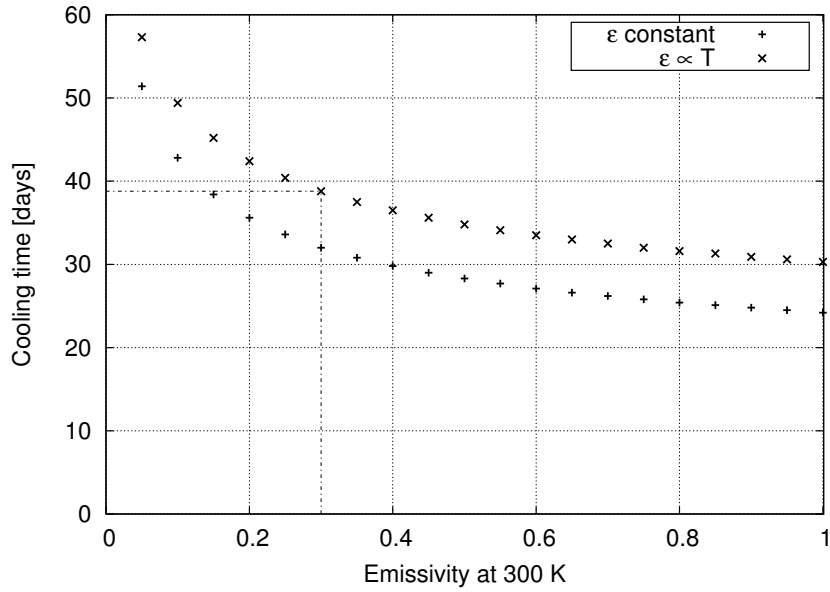


Figure 6.1: Dependence of the cooling time on the emissivity of the coating. “+” represents the result where the emissivity is independent from temperature. “x” represents the result where the emissivity is proportional to temperature.

An error in the calculated cooling time is discussed. One of the most important parameters to calculate the cooling time is the emissivity of the material. Thus, dependence of the cooling time

on the emissivity of the coating has been calculated in Figure 6.1 using the calculation model of KAGRA cooling system described in Chapter 4. According to this result, the emissivity value of $0.4 \times (T/300 \text{ K})$ gives cooling time 37 days instead of 39 days with $0.3 \times (T/300 \text{ K})$. The variation of the emissivity of DLC coating (the difference of 0.1 at 300 K) yields 5% error in the cooling time, and then, 3% error in the time of one cycle of heating up and cooling down.

Future prospect

There are two ways to make the cooling time even shorter. The one is to look for material which has both higher emissivity than the DLC coating and vacuum compatibility to use in cryogenic interferometric gravitational wave detectors. For this purpose, all one has to do is to measure emissivity and outgassing rate of the materials one by one. The zigzag structure on the surface to increase absorption might be candidate. However, there are problems that the tracing of the scattered light is not easy because of the complex surface structure and that the out-gassing rate is large due to effectively large surface area of the zigzag structure. According to Figure 6.1, the minimum cooling time, where the material is black body even in cryogenic temperature, is 24 days, which is a theoretical limit of the cooling time reduction by increasing radiation when no other change is made. The other way is to cool down the shields faster. Cooling of the payload with the high-emissivity coating is limited by cooling of the inner shield above approximately 150 K, as shown in Figure 4.10. Although cryogenics, such as liquid nitrogen, can help the cooling of the shields, there is a higher risk for gas from the cryogenics to fill the underground environment. Another problem of cooling the shields by cryogenics is complexity of structure of the cryostat with pipes where the cryogen flows. Research on and development of other methods, such as ones described in 3.1, will be useful.

6.2 Conclusion

The direct detection of gravitational waves is of great importance in physics and astronomy. Several second-generation detectors including KAGRA are currently under construction. Third-generation gravitational wave detectors, such as ET (the Einstein Telescope) in Europe, are also being planned. One of the most important problems in the cryogenic mirrors, advanced technology adopted in KAGRA and ET, is the long cooling time of the mirrors. During that time, the detectors cannot observe gravitational waves, and then gravitational wave events, such as the coalescence of binary neutron stars, will be missed. Because the detectors expect to have the periodical maintenances including heating up and cooling down of the mirrors, the long cooling time decreases observation time of the detectors. Therefore, it is necessary to reduce the cooling time.

In this thesis, I have constructed the calculation model of heat transfer in KAGRA cooling system. And then, I have verified the model experimentally. Namely, I have succeeded in

understanding the heat transfer among the complex cooling system.

According to this calculation model, the duty factor of KAGRA has been increased from 71 % to 77 % as a result of introducing the high-emissivity coating. Table 6.1 shows that one cycle of heating up and cooling down can be reduced from 88 days to 69 days. This cycle will happen every 300 days, as shown in eq.(3.10).

I have experimentally verified the calculation model and demonstrated that the observation efficiency of the cryogenic interferometric gravitational wave detectors can be increased, using an actual detector KAGRA, for the first time in the world. This research will be applicable to ET (Einstein Telescope), which is now being planned.

A

Thermal conductivity measurement of heat links

A.1 Purpose

Thermal conductivity of copper and aluminum wires for the heat links, made by Hitachi-densen, has already been measured[68]. However, the company is not available now due to their withdrawal. It is necessary to examine thermal conductivity of other possible candidates for the heat links to use in the calculation model described in Section 4.3.

A.2 Samples

The samples measured are:

- Copper wires made by Mitsubishi-densen
 - High-purity 99.99999 % (7N) twisted copper wires (the diameter of a single wire is 0.08 mm, 154 wires are twisted, yielding a total cross sectional area of 0.774 mm^2)
 - * Not annealed
 - * Annealed at $500 \text{ }^\circ\text{C}$ for 3 hours
 - * Annealed at $700 \text{ }^\circ\text{C}$ for 3 hours
 - High-purity 99.9999 % (6N) wire with 0.8 mm in diameter
 - * Annealed at unknown condition
- Aluminum wires made by Tanaka-kikinzoku
 - High-purity 99.999 % (5N) wire with 0.15 mm in diameter
 - * Not annealed
 - * Annealed at $500 \text{ }^\circ\text{C}$ for 3 hours

A.3 Method

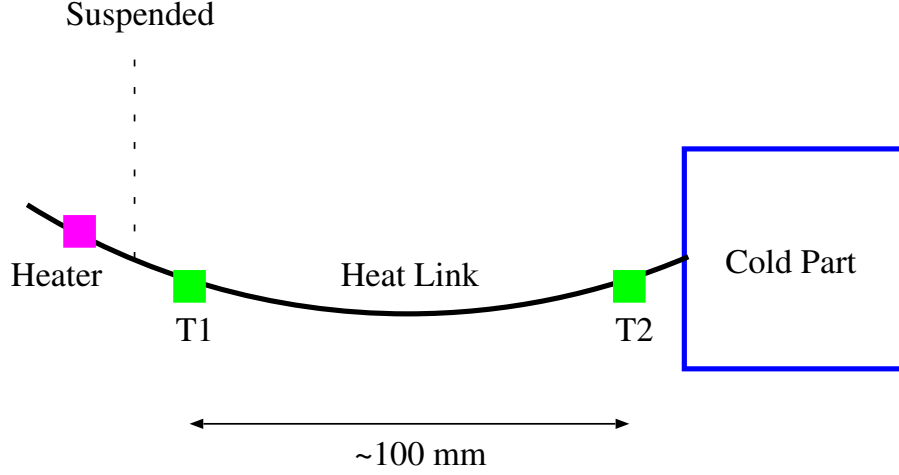


Figure A.1: Schematic diagram of the experimental setup. The one edge of the sample is attached to the cold part (copper block). The other edge is suspended by a Kevlar wire to isolate thermally. Two thermometers (T1, T2) and one heater are attached to the sample. Temperature of the copper block is controlled by a cryocooler and another heater (not shown).

The experimental setup is shown in Figure A.1-A.3. The one edge of the sample was attached to a copper block using a crimp contact. The other edge is suspended by a Kevlar wire for thermal isolation. Three jigs made of copper were attached to the sample with indium inserted (drawing of the jig is shown in Figure A.4). On these jigs, two thermometers (DT-670-CU made by LakeShore, calibrated) and one heater (1 k Ω SMD resistor) were attached. As electronic cables, phosphor bronze wires are used to minimize heat input. To block out thermal radiation, the sample was covered by an aluminum foil radiation shield as shown in Figure A.3.

Temperature of the copper block was controlled by a Lakeshore model 336 temperature controller with a cryocooler (Sumitomo Heavy Industry model RP-062B) and another heater. When the measurement started, temperature of the copper block T_0 was set to temperature of interest. When the copper block temperature became stable (deviation of T_0 less than 10 mK), temperature difference ΔT between T1 and T2 was measured with no heat from the heater attached on the sample. Next, constant heat was applied by the heater. The heater power P was obtained by the current and the voltage measured by the four electrodes method. When temperature of T1 and T2 became sufficiently stable, ΔT was recorded. Similarly, ΔT 's of several different amounts of heat were measured. After confirming that the relationship between P and ΔT is linear, the thermal conductivity κ was calculated from the fitting using

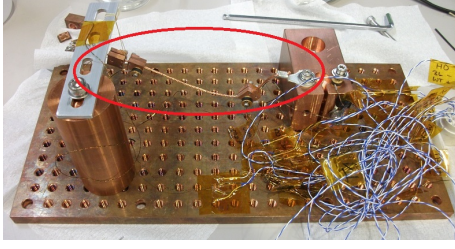


Figure A.2: Photo of the experimental setup. Schematic diagram of the red circled part is shown in Figure A.1. The whole copper plate is cooled down by the cryocooler.

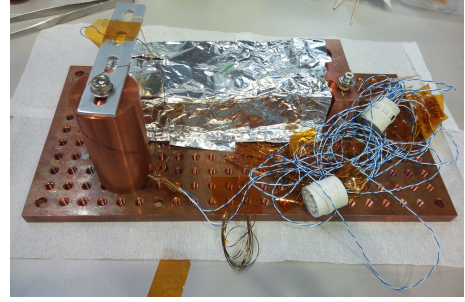


Figure A.3: Photo of the experimental setup. To block out thermal radiation, the sample was covered by a radiation shield made by an aluminum foil.

relation:

$$\kappa = \frac{P\ell}{S\Delta T}. \quad (\text{A.1})$$

Here, S is cross sectional area of the sample, and ℓ is length of the sample between T1 and T2. This measurement was repeated for different T_0 's. Typical temperature difference ΔT was 1 K.

For the measurement of each sample, it takes one day to make vacuum (pressure less than 10^{-3} Pa). Cooling down a cryostat takes a half day. Measuring the sample from ~ 4 K to ~ 100 K takes several days. Heating up the cryostat takes a half day. Thus, one series of the measurement takes 4 or 5 days.

The measured thermal conductivity value has an error of 20 %.

It is important to note that thermal conductivity depends on the second power of the diameter of the sample via cross sectional area S . When the sample has 0.10 mm in diameter, only 0.01 mm difference gives 20 % error. On the other hand, a contact length of the copper jigs is 3 mm, which is 3 % of the typical length $\ell = 100$ mm.

Another contribution is precision of the thermometers 100 mK. Since typical temperature difference ΔT is 1 K, this error corresponds to 10 %.

An error in the heater power P is less than 10 %. Estimated heat transferred by (a)thermal radiation or thermal conduction via (b)the electric cables and (c)the Kevlar wire was less than the order of 1 mW. During the measurement, heat larger than 10 mW was applied. Moreover, it is confirmed that the fitting error is less than 10 %.

A.4 Result

Figures A.5, A.6 show the result.

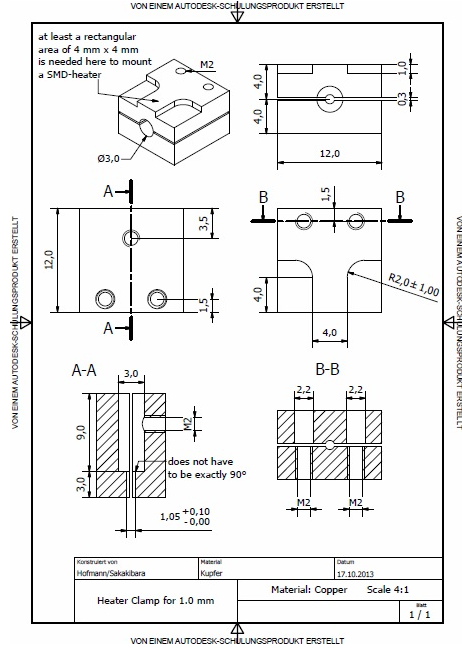


Figure A.4: Drawing of a copper jig to attach the thermometer or the heater to the sample designed by G.Hofmann. In cross section of A-A, a hole with 1.05 mm in diameter contacts the sample and a M2 hole is used to attach the thermometer.

Generally, thermal conductivity of metal is given as:

$$\kappa = \frac{1}{3} C_v v \ell, \quad (\text{A.2})$$

where C_v is the specific heat at constant volume, v is the averaged velocity of electrons, and, ℓ is the mean free path of electrons. Temperature dependence of v is negligible. The specific heat of electron is proportional to temperature, $C_v \propto T$. Below several ten Kelvin, the mean free path is limited by impurity or defect inside the metal. If the wire diameter is smaller than this length determined by the defect, the mean free path is limited by the sample size. This is called size effect. Because this limit is independent of temperature, temperature dependence of thermal conductivity comes from the specific heat of electrons. Namely, thermal conductivity is proportional to T [55, 69].

Figure A.5 shows that the annealing can improve thermal conductivity of the 7N twisted wires. Annealing can increase the size of the grain boundaries, which limit the mean free path of the samples not annealed. Since thermal conductivity of the 7N twisted wires annealed at 500 °C and 700 °C is the same, the effect of annealing has already saturated at 500 °C.

Thermal conductivity of the 7N twisted wires is lower than the thicker wires. The size effect

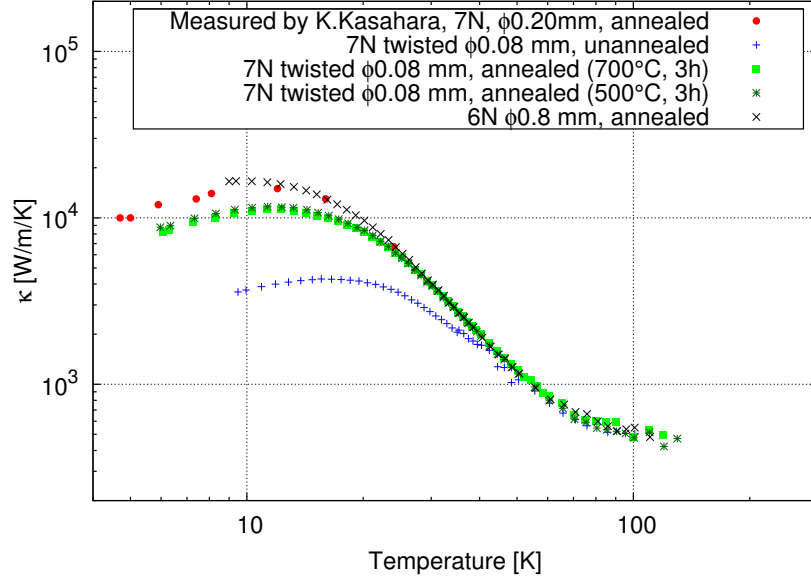


Figure A.5: Result of the thermal conductivity measurement of the copper wires. Values “Measured by K. Kasahara” are taken from Ref.[68].

can be one of the causes.

Figure A.6 shows that the annealing can improve thermal conductivity of the aluminum wires. Thermal conductivity of the annealed wires is comparable to K. Kasahara’s result. Since a soft material (material with a smaller Young’s modulus, aluminum) is suitable for the heat links of KAGRA, the measured thermal conductivity was used for the calculation of KAGRA cooling time in Section 4.3.

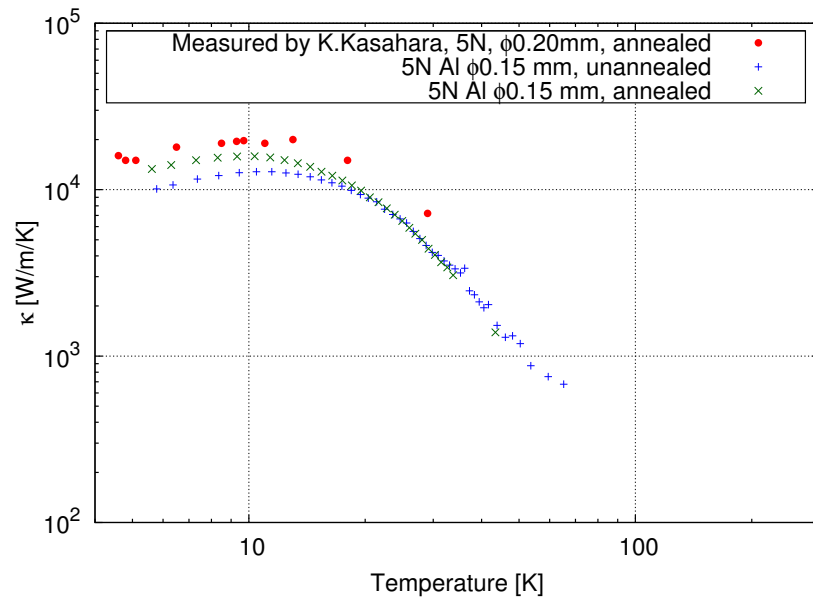


Figure A.6: Result of the thermal conductivity measurement of the aluminum wires. Values “Measured by K. Kasahara” are taken from Ref.[68]. Values of “5N Al $\phi 0.15$ mm, unannealed” were used in calculation in Section 4.3.

B

Sample code

The calculation of the cooling time of KAGRA was conducted using a Mathematica code. This chapter gives the sample code used to obtain Figure 4.10.

```
filename = "cooling13"; (*Output file name*)

(*Material Property*)
edlc[T_] = 0.3 * (T/300.0); (*Emissivity of coating*)
esap[T_] = 0.5; (*Emissivity of sapphire*)
 $\sigma$  = 5.67 * 10^(-8); (*Stefan – Boltzmannconstant*)
csapt = Import["cp3.txt", "Table"]; (*Specificheatofsapphire,
importedastable*)
csap = Interpolation[csapt, InterpolationOrder → 1]; (*Interpolating*)
ccut = Import["cucp.txt", "Table"]; (*Specific heat of copper*)
ccu = Interpolation[ccut, InterpolationOrder → 1];
lpt = ListLogLogPlot[{csapt, ccut},
PlotStyle → {RGBColor[1, 0, 0], RGBColor[0, 0, 1]},
GridLines → Automatic, AxesOrigin → {20, 0.1},
```

```

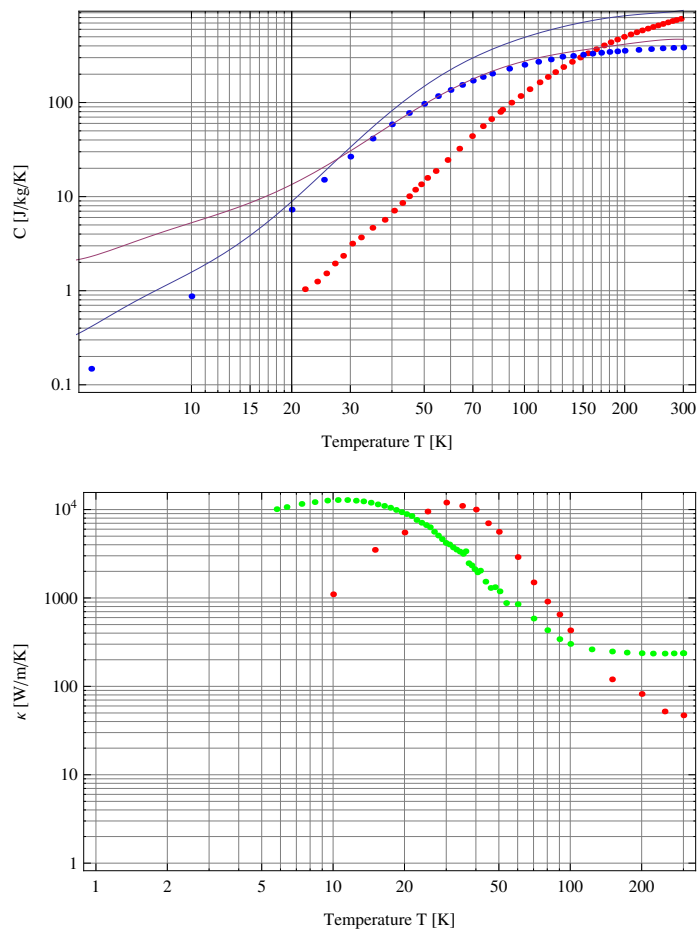
FrameLabel → {"Temperature T [K]", "C [J/kg/K]"},
Frame → True];
cal[T_] =
10^(46.6467 + (-314.292 * Log[10, T]) + (866.662 * Log[10, T]^2)+
(-1298.3 * Log[10, T]^3) + (1162.27 * Log[10, T]^4)+
(-637.795 * Log[10, T]^5) + (210.351 * Log[10, T]^6)+
(-38.3094 * Log[10, T]^7) + (2.96344 * Log[10, T]^8));
(*Specific heat of aluminum*)
csus[T_] =
10^(22.0061 + (-127.5528 * Log[10, T]) + (303.647 * Log[10, T]^2)+
(-381.0098 * Log[10, T]^3) + (274.0328 * Log[10, T]^4)+
(-112.9212 * Log[10, T]^5) + (24.7593 * Log[10, T]^6)+
(-2.239153 * Log[10, T]^7)); (*Specific heat of stainless steel*)
pt = LogLogPlot[{cal[T], csus[T]}, {T, 4, 300},
GridLines → Automatic, AxesOrigin → {20, 0.1},
FrameLabel → {"Temperature T [K]", "C [J/kg/K]"},
Frame → True];
Show[{lpt, pt}]
κalt = Import["altc-140106.txt", "Table"];
(*Thermal conductivity of aluminum*)
κal = Interpolation[κalt, InterpolationOrder → 1];
κsapt = Import["sapphirefiberk-sascha.txt", "Table"];
(*Thermal conductivity of sapphire*)
κsap = Interpolation[κsapt, InterpolationOrder → 1];

```

```

ListLogLogPlot[{ $\kappa_{\text{sapt}}$ ,  $\kappa_{\text{alt}}$ },
PlotStyle  $\rightarrow$  {RGBColor[1, 0, 0], RGBColor[0, 1, 0]},
GridLines  $\rightarrow$  Automatic, AxesOrigin  $\rightarrow$  {0, 0},
FrameLabel  $\rightarrow$  {"Temperature T [K]", " $\kappa$  [W/m/K]"},
Frame  $\rightarrow$  True]

```



(*Payload parameters*)

$N_{\text{mass}} = 5;$

$N_{\text{fix}} = 2;$

```

Mname = {"PF", "IR", "IM", "RM", "TM", "Cooling Bar", "Inner Shield"};
For[i = 1, i ≤ 4, i++, ε[i] = εdlc[T[i][t]])(*Emissivity of each mass*)
ε[5] = εsap[T[5][t]];
For[i = 1, i ≤ 4, i++, c[i] = csus[T[i][t]])(*Specific heat of each mass*)
c[5] = csap[T[5][t]];
M = {61.5, 44.9, 44.9, 33.7, 22.7}; (*Mass*)
A = {0.251, 0.451, 0.293, 0.182, 0.076}; (*Surface area*)
rad1 = {{1, 7}, {2, 7}, {4, 7}, {5, 7}}; (*Radiation from which to which*)
rad2 = {{2, 3}};
condal = {{2, 6, 45 8, 0.1510−3, 0.942},
{1, 2, 10, 310−3, 0.628},
{1, 3, 10, 310−3, 0.628},
{2, 4, 8, 1.610−3, 0.471}}; (*Parameters of heat links*)
condsap = {{3, 5, 4, 1.610−3, 0.3}}; (*Parameters of sapphire fibers*)
{Table[i, {i, 1, Nmass + Nfix}], Mname, Join[M, Table["-", {i, 1, Nfix}]],
Join[A, Table["-", {i, 1, Nfix}]]} // MatrixForm
shield = 7;
Tshfin = 8;
mirror = 5;

```

$$\begin{pmatrix}
1 & 2 & 3 & 4 & 5 & 6 & 7 \\
\text{PF} & \text{IR} & \text{IM} & \text{RM} & \text{TM} & \text{Cooling Bar} & \text{Inner Shield} \\
61.5 & 44.9 & 44.9 & 33.7 & 22.7 & - & - \\
0.251 & 0.451 & 0.293 & 0.182 & 0.076 & - & -
\end{pmatrix}$$

```

(*Calculate Q*)
Q = Table[Table[0, {i, 1, Nmass + Nfix}], {j, 1, Nmass + Nfix}];
For[i = 1, i ≤ Length[rad1], i++,
in = rad1[[i, 1]];
out = rad1[[i, 2]];
Q[[in, out]] = Q[[in, out]] +  $\epsilon[in] A[[in]] \sigma(T[in][t]^4 - T[out][t]^4)$ ;];
For[i = 1, i ≤ Length[rad2], i++,
in = rad2[[i, 1]];
out = rad2[[i, 2]];
Q[[in, out]] =
Q[[in, out]] +
 $A[[in]] \sigma(T[in][t]^4 - T[out][t]^4) / (1/\epsilon[in] + 1/\epsilon[out] - 1)$ ;];
For[i = 1, i ≤ Length[condal], i++,
in = condal[[i, 1]];
out = condal[[i, 2]];
Nal = condal[[i, 3]];
dal = condal[[i, 4]];
lal = condal[[i, 5]];
Q[[in, out]] =
Q[[in, out]] +  $Nal(\pi * (dal/2)^2) / lal$ 
Integrate[ $\kappa_{al}[T0]$ , {T0, T[out][t], T[in][t]}];
Print[{Mname[[in]], Mname[[out]], Nal, N[dal] * 1000, lal}]
];

```

```

For[i = 1, i ≤ Length[condsap], i++,
in = condsap[[i, 1]];
out = condsap[[i, 2]];
Nsap = condsap[[i, 3]];
dsap = condsap[[i, 4]];
lsap = condsap[[i, 5]];

Q[[in, out]] =
Q[[in, out]] + Nsap(π * (dsap/2)^2)/lsap
Integrate[κsap[T0], {T0, T[out][t], T[in][t]}];
Print[{Mname[[in]], Mname[[out]], Nsap, N[dsap] * 1000, lsap}]
];

Q = Q - Transpose[Q];

{IR, Cooling Bar, 360, 0.15, 0.942}
{PF, IR, 10, 3., 0.628}
{PF, IM, 10, 3., 0.628}
{IR, RM, 8, 1.6, 0.471}
{IM, TM, 4, 1.6, 0.3}

Q//MatrixForm

```

$$\begin{pmatrix}
0 & & & & \\
-0.000112557 \int_{T[2][t]}^{T[1][t]} \text{InterpolatingFunction}[\{\{5.776, 300.\}\}, <>][T0] dT0 & & & \\
-0.000112557 \int_{T[3][t]}^{T[1][t]} \text{InterpolatingFunction}[\{\{5.776, 300.\}\}, <>][T0] dT0 & & & \\
0 & & \dots & & \\
0 & & & & \\
0 & & & & \\
-1.42317^{*-11} T[1][t] (T[1][t]^4 - T[7][t]^4) & & & &
\end{pmatrix}$$

(*Fix temperature of mass*)

```
Tsht = Import["no4-8KTOP-calc.txt", "Table"];
```

```
Tsh = Interpolation[Tsht, InterpolationOrder → 1];
```

```
T[6][t_] = 8;
```

```
T[7][t_] = Tsh[t];
```

(*Solve differential equations*)

```
init = Table[T[i][0] == 300, {i, 1, Nmass}];
```

```
eqs = Table[D[T[i][t], t] == -(Total[Q[[i]])]/(M[[i]]c[i]), {i, 1, Nmass}];
```

```
sol = NDSolve[Join[eqs, init], Table[T[i], {i, 1, Nmass}], {t, 0, 10000000},
```

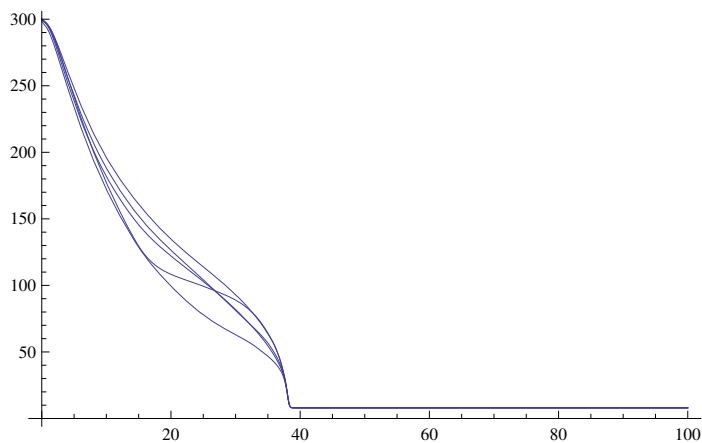
```
MaxSteps->100000];
```

```
For[i = 1, i ≤ Nmass, i++,
```

```
solT[i][t_] = Evaluate[T[i][t]/.sol][[1]];
```

```
]
```

```
Plot[Table[solT[i][t * 24 * 3600], {i, 1, Nmass}], {t, 0, 100}]
```



(*Export as text file*)

```
tmax = 100; dt = tmax * 3600 * 24/1000;
```

```
title = Join[{“#Time[s]”}, Mname];  
data2 = Table[Join[{dtj}, Table[solT[i][dtj], {i, 1, Nmass}],  
Table[T[Nmass + i][dtj], {i, 1, Nfix}]], {j, 0, 1000}];  
Export[filename <> “.txt”, Join[{title}, data2], “Table”]  
  
cooling13.txt
```


Acknowledgement

This research was conducted mainly in Gravitational Wave Project Office (GWPO), Institute for Cosmic Ray Research (ICRR), the University of Tokyo (Kashiwa, Chiba prefecture). Some experiments needed the large-sized KAGRA cryostats or the duct shields and I often conducted experiment in manufacturing companies of them (Toshiba Corporation and Jecc Torisha Co. Ltd.). I also visited Europe for two months (UK for one month, Germany for one month). I conducted a collaborative research with researchers there.

First of all, I would like to thank my supervisor and a chief of GWPO, K. Kuroda. He supported me not only about my thesis or my career but also about travel budget for the collaborative research in Europe and domestic/international conferences.

I would like to express my gratitude to people in KAGRA cryogenic subsystem, which I worked for to conduct this research. Some of them belong to High Energy Accelerator Research Organization (KEK). I often discussed whether my experiment plan is consistent with KAGRA construction schedule with chiefs of the cryogenic subsystem, T. Suzuki, N. Kimura, and, K. Yamamoto. Especially, N. Kimura went with me and helped me when I went to my first international conference, as well as, supported my experiment and thesis technically and financially. T. Suzuki told me interesting physics theory or idea underlying the research. K. Yamamoto read my paper submission or abstract of the conferences carefully and gave me useful comments. C. Tokoku, a technical staff in ICRR, not only took charge of the lab or ordered its equipment but also gave me comments about my experiments. T. Uchiyama also supported a part of the experiment financially. S. Koike designed or gave me useful comment about the experimental apparatus. D. Chen, who started ph.D in the same year in ICRR, helped me with the experiment when I was absent. T. Tomaru, who is also from K. Kuroda's lab and came back to the field of the gravitational waves when I was the second year of ph.D, especially cared about my ph.D thesis.

I'd like to thank S. Ioka, K. Nakamoto, H. Nezuka, T. Orikasa, H. Fukuda in Toshiba Corporation. They helped us with setting up the experiment when we visited there. When the experiment delayed, they kindly adjusted their manufacturing schedule. In Jecc Torisha Co. Ltd., I appreciate M. Tanaka, S. Goto, M. Sugino, Y. Kobayashi, and Y. Higuchi, manufacturing my experimental apparatus and helping with the experiment. Especially, M. Tanaka welcomed me when I visited there for the experiment, and kindly helped the experiment even when I

asked him to do so by e-mails.

T. Kajita, chief of ICRR and project leader of KAGRA, cared about status of the experiment when I met him in a corridor in ICRR. S. Miyoki not only helped me with things about ICRR network but also cared my research. S. Kawamura often supported me with my travel budget. R. Takahashi, chief of vibration isolation subsystem, and T. Sekiguchi, the same year ph.D student as me in the vibration isolation subsystem, E. Hirose in mirror subsystem, Y. Saito in vacuum subsystem, T. Akutsu in axillary optics subsystem, helped me especially when sharing information or adjustment between their subsystem and the cryogenic subsystem is necessary. K. Agatsuma asked me an useful question, which enriched discussion in Chapter 6

During the collaborative research, I visited S. Rowan's lab, Institute for Gravitational Research (IGR), Glasgow University. I'm thankful that M. Peter and D. Rebecca looked after me. K. Rahul, who was in Glasgow during my visit, came to ICRR next year and worked in the same office. Next, I visited R. Nawrodt's lab, institute of solid state physics, Friedrich-Schiller-Universität Jena. D. Heinert looked after me and G. Hofmann, J. Komma helped me. They visited ICRR next year and also helped me about the thermal conductivity measurement of the heat links.

I thank R. Kikuchi, R. Sato, C. Mashima, A. Chida, secretaries in ICRR for paper works about travel or order of apparatus.

Advanced Leading Graduate Course for Photon Science (ALPS) in Graduate School of Science, the University of Tokyo, provided me with both economic and academic support. I discussed the status of the experiment with S. Yamamoto, sub-supervisor in ALPS.

I'd like to mention that this work was supported by (1)the Leading-edge Research Infrastructure Program from the Ministry of Education, Culture, Sports, Science and Technology (MEXT), (2)JSPS KAKENHI Grant Numbers 25420857, and (3)JSPS Core-to-Core Program, A. Advanced Research Networks.

Finally, I wish KAGRA project would make a great success.

References

- [1] M. Maggiore: “Gravitational Waves I. theory and experiments,” Oxford Univ. Press (2007)
- [2] T. Nakamura et al.: “Detecting gravitational waves,” Kyoto University Press (1998) [in Japanese]
- [3] P R. Saulson: “Fundamentals of interferometric gravitational wave detectors,” Singapore; River Edge, NJ : World Scientific (1994)
- [4] “LCGT design document Version 3.0” (2009) [in Japanese]
- [5] J M. Weisberg and J H. Taylor: “Relativistic binary pulsar B1913+16: thirty years of observations and analysis,” ASP Conference Series **328** (2005) 25-31
- [6] N. Nakagawa et al.: “Thermal noise in half-infinite mirrors with nonuniform loss: A slab of excess loss in a half-infinite mirror,” Phys. Rev. D **65** (2002) 102001
- [7] V. B. Braginsky et al.: “Thermodynamical fluctuations and photo-thermal shot noise in gravitational wave antennae,” Phys. Lett. A **264** (1999) 1-9
- [8] M. Cerdonio et al.: “Thermoelastic effects at low temperatures and quantum limits in displacement measurements,” Phys. Rev. D **63** (2001) 082003
- [9] T. Uchiyama et al.: “Cryogenic cooling of a sapphire mirror-suspension for interferometric gravitational wave detectors,” Phys. Lett. A **242** (1998) 211-214
- [10] G. Harry et al.: “Optical coatings and thermal noise in precision measurement,” Cambridge University Press, (2012)
- [11] K. Yamamoto: “Cryogenic Mirrors - The State-of-the-art in Interferometric Gravitational Wave Detectors,” TEION KOGAKU **46**(7) (2011) 426-433 [in Japanese]
- [12] T. Uchiyama et al.: “Mechanical quality factor of a cryogenic sapphire test mass for gravitational wave detectors,” Phys. Lett. A **261** (1999) 5-11

- [13] K. Yamamoto et al.: “Measurement of the mechanical loss of a cooled reflective coating for gravitational wave detection,” *Phys. Rev. D* **74** (2006) 022002
- [14] E. Hirose et al.: “Mechanical loss of a multilayer tantala/silica coating on a sapphire disk at cryogenic temperatures: Toward the KAGRA gravitational wave detector,” *Phys. Rev. D* **90** (2014) 102004
- [15] AIST, Network Database System for Thermophysical Property Data
http://riodb.ibase.aist.go.jp/TPDB/DBGVsupport/index_en.html
- [16] Y.S.Touloukian: “Thermophysical Properties of Matter Volume 5 Specific Heat Nonmetallic Solids,” IFI/Plenum (1970)
- [17] T. Tomaru et al.: “Thermal lensing in an cryogenic sapphire substrates,” *Class. Quantum Grav.* **19** (2002) 2045-2049
- [18] K. Yamamoto et al.: “Parametric instabilities in the LCGT arm cavity,” *J. Phys.: Conf. Ser.* **122** (2008) 012015
- [19] G. M. Harry: “Advanced LIGO: the next generation of gravitational wave detectors,” *Class. Quantum Grav.* **27** (2010) 084006
- [20] T. Accadia et al.: “Virgo: a laser interferometer to detect gravitational waves,” *JINST* **7** (2012) P03012
- [21] H. Grote: “The GEO 600 status,” *Class. Quantum Grav.* **27** (2010) 084003
- [22] K. Arai: “Recent progress of TAMA300,” *J. Phys.: Conf. Ser.* **120** (2008) 032010
- [23] K. Somiya: “Detector configuration of KAGRA - the Japanese cryogenic gravitational-wave detector,” *Class. Quantum Grav.* **29** (2012) 124007
- [24] M. Punturo et al.: “Advanced Interferometers and the Search for Gravitational Waves,” *Astrophysics and Space Science Library* **404** (2014) 333-362
- [25] Y. Sakakibara et al.: “Progress on the Cryogenic System for the KAGRA Cryogenic Interferometric Gravitational Wave Telescope,” *Class. Quantum Grav.* **31** (2014) 224003
- [26] R. I. Epstein et al.: “Observation of laser-induced fluorescent cooling of a solid,” *Nature* **377** (1995) 500-503
- [27] R. I. Epstein et al.: “Solid-State Optical Cryocoolers,” *ICEC 25-ICMC 2014* (2014) Tue-Af-Orals Session 5
- [28] R. S. Ottens et al.: “Near-Field Radiative Heat Transfer between Macroscopic Planar Surfaces,” *Phys. Rev. Lett.* **107** (2011) 014301

- [29] R. Dolesi et al.: “Brownian force noise from molecular collisions and the sensitivity of advanced gravitational wave observatories,” *Phys. Rev. D* **84** (2011) 063007
- [30] K. Yamamoto et al.: “Current status of the CLIO project,” *J. Phys.: Conf. Ser.* **122** (2008) 012002
- [31] K. Agatsuma et al.: “Direct Measurement of Thermal Fluctuation of High-Q Pendulum,” *Phys. Rev. Lett.* **104** (2010) 040602
- [32] T. Uchiyama et al.: “Reduction of Thermal Fluctuations in a Cryogenic Laser Interferometric GravitationalWave Detector,” *Phys. Rev. Lett.* **108** (2012) 141101
- [33] T. Tomaru, et al.: “Conduction effect of thermal radiation in a metal shield pipe in a cryostat for a cryogenic interferometric gravitational wave detector,” *Jpn. J. Appl. Phys.* **47** (2008) 1771-1774
- [34] T. Tomaru, et al.: “Study of Heat Load Reduction for the LCGT Cryostat,” *J. Phys. Conf. Ser.* **122** (2008) 012009
- [35] E. Hirose, T. Sekiguchi: “Preliminary design of Type-A suspension system (cryogenic seismic attenuation system) for KAGRA sapphire mirrors,” JGW-T1402106-v1 (2014) <http://gwdoc.icrr.u-tokyo.ac.jp/cgi-bin/DocDB/ShowDocument?docid=2106>
- [36] E. Hirose, et al.: “Update on the development of cryogenic sapphire mirrors and their seismic attenuation system for KAGRA,” *Class. Quantum Grav.* **31** (2014) 224004
- [37] T. Kume, et al.: “Development of the very low vibration cryocooler unit for large-scale cryogenic gravitational wave telescope, KAGRA,” *Proceedings of ICEC 24-ICMC 2012* (2012) 399-402
- [38] C. Tokoku, et al.: “Cryogenic system for the interferometric cryogenic gravitationalwave telescope, KAGRA - design, fabrication, and performance test -,” *AIP Conf. Proc.* **1573** (2014) 1254-61
- [39] S. Miyoki et al.: “Cryogenic contamination speed for cryogenic laser interferometric gravitational wave detector,” *Cryogenics* **41** (2001) 415-420
- [40] E. Hirose et al.: “Sapphire mirror for the KAGRA gravitational wave detector,” *Phys. Rev. D* **89** (2014) 062003
- [41] Y. Sakakibara, et al.: “A Study of Cooling Time Reduction of Interferometric Cryogenic Gravitational Wave Detectors Using a High-Emissivity Coating,” *AIP Conf. Proc.* **1573** (2014) 1176-83

- [42] ET Science Team: “Einstein gravitational wave Telescope Conceptual Design Study,” (2011), p.156.
(available at: <http://www.et-gw.eu/etdsdocument>)
- [43] Y. Sakakibara: “A Study of Thermal Radiation Shields for Cryogenic Gravitational Wave Detectors,” master thesis, univ. of Tokyo (2012)
- [44] Y. Sakakibara, et al: “Calculation of thermal radiation input via funneling through a duct shield with baffles for KAGRA,” *Class. Quantum Grav.* **29** (2012) 205019
- [45] R. Takahashi, Y. Saito: “Vacuum-system design for the large-scale cryogenic gravitational wave telescope,” *Vacuum* **84** (2010) 709-712
- [46] H. Suzuki, M. Ikenaga: “Technology to deposit DLC,” *Nikkan Kogyo Shimbun* (2003) [in Japanese]
- [47] R. Takahashi, et al.: “Application of diamond-like Carbon (DLC) coatings for gravitational wave detectors,” *Vacuum* **73** (2004) 145-148
- [48] T. Tomaru, et al.: “Evaluation of Vacuum and Optical Properties of Nickel-Phosphorus Optical Absorber,” *JOURNAL OF THE VACUUM SOCIETY OF JAPAN* **48**(5) (2005) 301-303 [in Japanese]
- [49] Y. Saito: “slides for KAGRA f2f meeting (14th of Feb, 2013),” JGW-G1301527-v1 (2013) <http://gwdoc.icrr.u-tokyo.ac.jp/cgi-bin/DocDB/ShowDocument?docid=1527>
- [50] K. Ono: “Experiment to measure emissivity of Solblack in low temperature for KAGRA,” meeting of the Physical Society of Japan (2013) 22pSR-6 [in Japanese]
- [51] Asahi Precision. Co. Ltd.: “Low Reflection & High Optical Absorption Blackening electroless plating,” http://www.akg.jp/puresijyon/download/ke_solblack.pdf
- [52] D. Chen et al.: “Vibration measurement in the KAGRA cryostat,” *Class. Quantum Grav.* **31** (2014) 224001
- [53] T. Tomaru, et al.: “Maximum heat transfer along a sapphire suspension fiber for a cryogenic interferometric gravitational wave detector,” *Phys. Lett. A* **301** (2002) 215-219
- [54] A. Khalaidovski et al.: “Evaluation of heat extraction through sapphire fibers for the GW observatory KAGRA,” *Class. Quantum Grav.* **31** (2014) 105004

- [55] T. Tomaru, et al.: “Conduction Cooling Using Ultra-pure Fine Metal Wire I -Pure Aluminum-,” TEION KOGAKU **46** (2011) 415-420 [in Japanese]
- [56] NIST Cryogenics Technologies Group
<http://cryogenics.nist.gov/MPropsMAY/material%20properties.htm>
- [57] Y. Sakakibara et al.: “Reflectivity Measurements of Metals for LCGT Thermal Radiation Shields at Cryogenic Temperature and Wavelength of 10 μm ,” TEION KOGAKU **46** (2011) 434-440 [in Japanese]
- [58] J.P.Holman. “Heat transfer 10th ed” (McGraw-Hill Higher Education, Boston, 2010), Chap. 8, Radiation Heat Transfer, pp. 379-486.
- [59] G. Ventura et al.: “Low temperature thermal conductivity of Kevlar,” Cryogenics **40** (2000) 489-491
- [60] Y. Ikushima et al.: “The Road to Vibration-free Refrigeration - Development of a Low-vibration Refrigeration System for CLIO -,” TEION KOGAKU **46**(7) (2011) 400-407 [in Japanese]
- [61] Sumitomo Cryogenics of America, Inc: “CH-104 and CH-110 Cold Heads Operating Manual,” (2010)
- [62] R. Takahashi, “Direct measurement of the scattered light effect on the sensitivity in TAMA300,” Phys. Rev. D **70** (2004) 062003
- [63] D. J. Ottaway et al.: “Impact of upconverted scattered light on advanced interferometric gravitational wave detectors,” OPTICS EXPRESS **20** (8) (2012) 8329
- [64] H. Yamamoto, “LIGO I mirror scattering loss by microroughness,” LIGO-T070082-04-E (2007)
- [65] Genesia Corporation, “Detailed design of stray light control in KAGRA 3 km arms,” GE1422-14-104 (2014)
- [66] E. E. Flanagan, K. S. Thorne: “Noise due to light scattering in interferometric gravitational wave detectors. I: Handbook of Formulae, and their Derivations” (2011)
- [67] KAGRA HP
<http://gwcenter.icrr.u-tokyo.ac.jp/researcher/parameters>

- [68] K. Kasahara et al.: “Study of Heat Links for a Cryogenic Laser Interferometric Gravitational Wave Detector,” *TEION KOGAKU* **39** (2004) 25-32 [in Japanese]
- [69] T. Shintomi et al.: “Conduction Cooling Using Ultra-pure Fine Metal Wire II -Pure Copper-,” *TEION KOGAKU* **46** (2011) 421-425 [in Japanese]